SCIENCE CHINA Materials
REVIEW

mater.scichina.com link.springer.com

| doi: 10.1007/s40843-015-0084-8
Sci China Mater 2015, 58: 715–766

Beyond Li-ion: electrode materials for sodium- and magnesium-ion batteries

Robert C. Massé[1], Evan Uchaker[1] and Guozhong Cao[1,2,3*]

The need for economical and sustainable energy storage drives battery research today. While Li-ion batteries are the most mature technology, scalable electrochemical energy storage applications benefit from reductions in cost and improved safety. Sodium- and magnesium-ion batteries are two technologies that may prove to be viable alternatives. Both metals are cheaper and more abundant than Li, and have better safety characteristics, while divalent magnesium has the added bonus of passing twice as much charge per atom. On the other hand, both are still emerging fields of research with challenges to overcome. For example, electrodes incorporating Na^+ are often pulverized under the repeated strain of shuttling the relatively large ion, while insertion and transport of Mg^{2+} is often kinetically slow, which stems from larger electrostatic forces. This review provides an overview of cathode and anode materials for sodium-ion batteries, and a comprehensive summary of research on cathodes for magnesium-ion batteries. In addition, several common experimental discrepancies in the literature are addressed, noting the additional constraints placed on magnesium electrochemistry. Lastly, promising strategies for future study are highlighted.

INTRODUCTION

The role of energy production and consumption plays an ever increasing role in modern society as our devices become more portable and nations like China and India become more industrialized. Trends towards reduced fossil fuel dependence are prompted by environmental and financial incentives based on global concern (or opportunity) regarding pollution, climate change, and resource scarcity. It will not be possible for many of the current policies to continue moving forward – one such being the global subsidies for fossil fuels, the bulk of which went to oil, that totaled $548 billion in 2013 alone [1]. Renewable energies are not subsidized at anywhere near that value, but will need to grow rapidly to keep pace with world energy consumption, which is projected to grow by 56% between 2010 and 2040 [2]. Accordingly, substantial effort has been made to develop and install renewable energy harvesting technologies [3]. However, their successful implementation will be dependent on reliable and robust storage devices since harvesting solar and wind energy is inherently intermittent and the majority of consumption targets cannot be readily tethered to the grid.

As energy storage devices, batteries possess high portability, high energy density, high Coulombic efficiency, and long cycle life. They are ideal power sources for portable devices, automobiles, and backup power supplies; accordingly, batteries power nearly all of our mobile electronics and are used to improve the efficiency of hybrid electric vehicles [4,5]. Unfortunately, considerable improvements in performance are still required in order to meet the demands of advanced portable devices and achieve energy sustainability (e.g., through smart grid and electric vehicle technologies) [6]. These enduring needs have driven intensive research investments. While efforts have been successful, there is still significant room for improvement regarding the development and understanding of electrode materials [7]. The overall capacity and potential cycling window of many electrode materials are limited to prevent degradation over long term cycling. In addition to exploring new electrode materials, there have been strong efforts to improve those that are already utilized. Expense reduction is a priority as approximately 23% and 8% of the overall battery pack costs stem from the respective cathode and anode active materials alone [8].

An alkali-ion battery consists of several electrochemical cells connected in parallel and/or in series to provide a designated current or voltage. Each electrochemical cell has two electrodes separated by an electrolyte that is electrically insulating but ionically conductive. During discharge, when the alkali-ion battery operates as a galvanic cell, alkali ions exit the negative electrode (typically carbon) and insert themselves into the positive electrode while electrons

---

[1] Department of Materials Science and Engineering, University of Washington, Seattle, WA 98195, USA
[2] Beijing Institute of Nanoenergy and Nanosystems, Chinese Academy of Sciences, Beijing 100083, China
[3] School of Materials Science and Engineering, Dalian University of Technology, Dalian 116023, China
[*] Corresponding author (email: gzcao@uw.edu)

move externally from the negative electrode to the positive electrode. During charge, it operates as an electrolytic cell, and the process is reversed by means of an externally applied electromotive force. The total energy stored in and released by a cell during charge and discharge is controlled by the thermodynamics and kinetic processes of the active electrode material.

For a given electrode material, the physical, structural, and electronic properties can be manipulated to alter the overall electrochemical performance. There are several ways in which alkali ions can be repeatedly incorporated and removed from the electrode electro-active material. The three main mechanisms through which alkali-ion de/insertion occurs are based on intercalation, alloying, and conversion reactions [9]. Pseudocapacitive adsorption on the surface is another storage mechanism [10], albeit traditionally more pertinent to capacitors. It is most often the case where there is only a single mechanism operating, but it is possible for there to be a combination of the processes taking place if certain criteria are met.

Alloying reactions are primarily observed in the Group IV (silicon and tin) and V (phosphorus and antimony) elements that serve as anodic materials with high specific capacity [11–13]. The main challenge for the implementation of alloy anodes is their large volume change 400% during lithium insertion and extraction, which often leads to pulverization of the active alloy particles and poor cycle stability. In addition, the first-cycle irreversible capacity loss of alloy anodes is too high for practical applications (solid electrolyte interphase (SEI) and loss of active material).

A more recently investigated system is the conversion mechanism that involves the formation and decomposition of at least two separate phases through conversion reactions [14]. Reversible conversion reactions can transpire between binary MX compounds, where M is often a transition metal and X a chalcogen or halogen, and metallic lithium, and are based on the reduction and oxidation of metal nanoparticles. Thus it is a reaction that involves heterogeneous lithium storage. It has been determined that the reversibility of the conversion reaction depends on complete reduction of the metal species.

Of the three methods, intercalation is by far the most thoroughly investigated and well understood, and was the system on which initial developments in Li-ion batteries (LIB) were based [15–17]. Intercalation is the reversible insertion of a guest species (ion or molecule) into the lattice of a lamellar host structure. The overall process of electrochemical intercalation can be broken down into three simultaneous and sequential processes: (*i*) redox reactions at the electrode-electrolyte interface, (*ii*) nucleation and growth of the new interfacial phase, and (*iii*) charge and mass transfer. The structure of the host remains unchanged or is only slightly altered in the guest-host complex with the inclusion of the intercalation compound (intercalate), however there can be phase changes depending on the extent of intercalation. The rate of intercalation can be controlled by imposing an external potential across the cell, and the reaction will stop when this potential equals the free energy of the system. Deintercalation will occur when the voltage exceeds this free energy.

The progress of energy storage materials and devices appreciably lags the rapid progression of other electronic components. In spite of steady advancements in these technologies, battery development has increasingly become the bottleneck impeding device development [18–20]. Among the commercially available energy storage media, alkali-ion (particularly lithium-ion) batteries are a mature and robust technology that has been extensively used in consumer devices because of their high energy density and portability [21,22]. Despite great commercial success, lithium-based batteries have several drawbacks associated with their potential safety issues, high cost, and resource scarcity. Conversely, sodium-ion (Na-ion or NIB) and magnesium-ion (Mg-ion or MIB) batteries have been gaining considerable attraction as realistic candidates for energy storage applications over the past several years [9,23–27]. Some of the pertinent properties are summarized in Table 1.

In sharp contrast to lithium-ion batteries, work on alternative chemistries such as sodium- and magnesium-ion batteries has been less intense, and both fields are still in their infancy. The number of publications is rising rapidly (for example, see Fig. 1 in Ref. [26]), indicative of the interest in and potential impact of these technologies. Although there are some excellent reviews published recently (including but not limited to Ref. [24–27,30–33]), the accelerated pace of developments in both fields justifies a summary of the most salient recent results.

As alkali metals, sodium and lithium have similar electrochemical behavior. Thus, analogous positive hosts such as layered oxides, and polyanion compounds, and Chevrel phases have seen notable developments, and at the negative electrode, graphene, TiO_2 and various alloying materials are reviewed. Conversely, magnesium electrochemistry is more complicated, and a comprehensive survey of cathode materials has been conducted to better understand the distinctive characteristics. This survey represents a compilation of magnesium cathode research to date, starting with the highly successful Chevrel phases, and including traditional transition metal oxides, silicates, chalcogenides, and other eclectic energy storage configurations. Throughout,

Table 1 Comparative qualities of lithium, sodium, and magnesium for alkaline (earth)-ion battery applications [28–30]

Parameter	Lithium	Sodium	Magnesium
Cationic radius (Å)	0.76	1.02	0.72
Atomic weight (g mol^{-1})	6.9	23.0	24.3
E (V *vs.* SHE)	−3.04	−2.71	−2.37
Carbonate cost ($/ton)	~6000	~150	~1000
Metallic capacity (mA h g^{-1})	3862 (Li^+)	1166 (Na^+)	2205 (Mg^{2+})
Metallic capacity (mA h cm^{-3})	2046	1129	3833
Coordination preference	Octahedral and tetrahedral	Octahedral and prismatic	Octahedral

an effort has been made to highlight conceptual and practical tools that will enable further progress, such as mechanistic information and the importance of the electrolyte in magnesium-containing systems.

SODIUM-ION BATTERIES

Advances in energy harvesting technologies have spurred the need for an array of energy storage for both portable and stationary applications. Fig. 1 shows the abundance (atomic fraction) of the chemical elements in Earth's upper continental crust as a function of atomic number [34]; clearly, it is more cost-effective to use less expensive and more abundant materials when available. As the use of large format batteries becomes widespread, increasing demand for lithium commodity chemicals combined with geographically-constrained lithium mineral reserves will drive up prices. Currently, approximately 35% of the world's production of lithium-containing precursor materials is now consumed by battery manufacturing while lithium recycling has been historically insignificant [35]. Identified lithium resources total 5.5 million tons in the US and approximately 34 million tons in other countries, with approximately 50% coming from Bolivia and Chile alone. Current Li-ion batteries are priced at approximately $600 USD per kWh, but several global government agencies have set goals of seeing these costs decrease to $150 USD per kWh with accompanying increases in energy density into the 400–500 Wh kg^{-1} range [36].

Compared to the comprehensive body of work on lithium-ion batteries, research on NIBs is still in its nascent stages [37]. An NIB functions under the same principles as Li-ion technology, but with different characteristics as dictated by the properties of the transporting ionic species and the consequent effects it has on the electrode materials (Table 1) [30]. As mentioned above, sodium and lithium share similar chemical properties including ionicity, electronegativity, and electrochemical reactivity as they are both alkali metals. They accordingly have comparable synthetic protocols and electrochemical performances, which indicates that the development of NIBs can be (ideally) based on previously applied approaches or methods utilized for LIBs. However, the larger size and different bonding char-

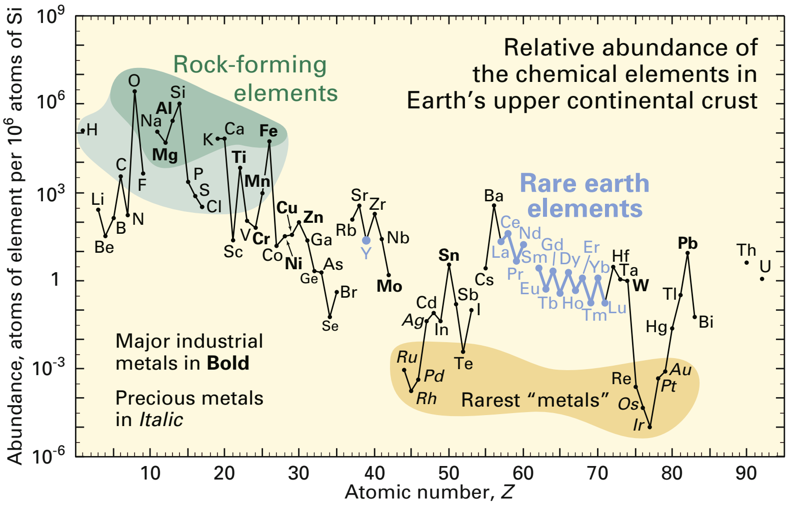

Figure 1 Abundance (atom fraction) of the chemical elements in Earth's upper continental crust as a function of atomic number [34].

acteristics of sodium ions influence the thermodynamic and kinetic properties of NIBs, and can lead to unexpected behavior in terms of electrochemical performance or reaction mechanism.

NIBs are attractive because sodium resources are seemingly inexhaustible as well as ubiquitous, and therefore cost considerably less (by a factor of roughly 30–40 times) than lithium; additionally, sodium does not undergo an alloying reaction with aluminum at low voltage, as is the case with lithium, meaning that aluminum can replace copper as the anodic current collector which equates to an overall cell cost savings of ~2% [30,38,39]. The lower operating voltage of Na-ion cells results in enhanced stability of the non-aqueous electrolyte [30], but also manifests itself in lower energy density. The majority of the proposed electrode materials for NIB show similar or slightly lower specific capacity and redox potential than when used in Li-ion cells [40,41]. Moreover, the accommodation of sodium in traditional host materials is difficult because the ionic radius and reduction potential of sodium are strikingly larger than that of lithium. Therefore, the (de)sodiation process induces large distortions in the host lattice that ultimately lead to pulverization of the electrode and the impending failure of the cell [42].

One of the most expensive material components of an alkali-ion battery, regardless of the configuration, is the cathode, as shown in Fig. 2. Reduction of cost has been one of the primary driving forces for the investigation of new cathode materials to replace expensive $LiCoO_2$, particularly for vehicular and grid storage applications. Thus, it is clear that the development of either other battery systems or the refinement of current assemblies using new materials is necessary. The majority of investigations, to date, examining NIB cathodes have focused on intercalation based materials, particularly layered transition metal oxides.

Positive electrode materials

Layered transition metal oxides

The effects of crystallinity on vanadium pentoxide as pertaining to NIB performance were recently investigated [44]. Amorphous and nanocrystalline V_2O_5 were prepared through a combination of sol-gel processing paired with electrochemical deposition and investigated as cathode for NIB. The amorphous V_2O_5 electrodes with short range order and a more open framework demonstrated a discharge capacity of 241 mA h g^{-1} when examined as positive electrode material for NIB application while its crystalline counterpart only had a capacity of 120 mA h g^{-1} (Figs 3c and d). The significant difference between the crystalline and amorphous phases arises from the fast Faradaic reactions which occur in amorphous V_2O_5 stemming from a percolated diffusion network. Moreover, because diffusion now occurs through isotropic percolation and is not confined along a preferential pathway, the overall charging/discharging rates are much faster. The discrepancy in performance is primarily accredited to the low entropic energy associated with the ordering of intercalated atoms and a more open framework. The less structured and more open channels reduce the diffusion barrier for sodium ions to transition between sites leading to high rate capability and energy density.

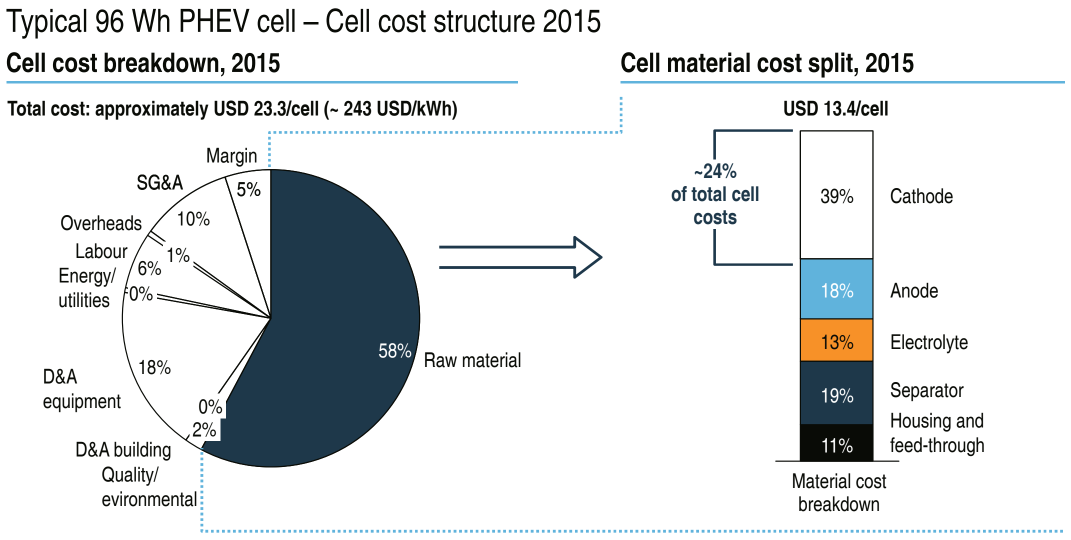

Figure 2 Material cost breakdown for a typical 96 Wh PHEV cell [43].

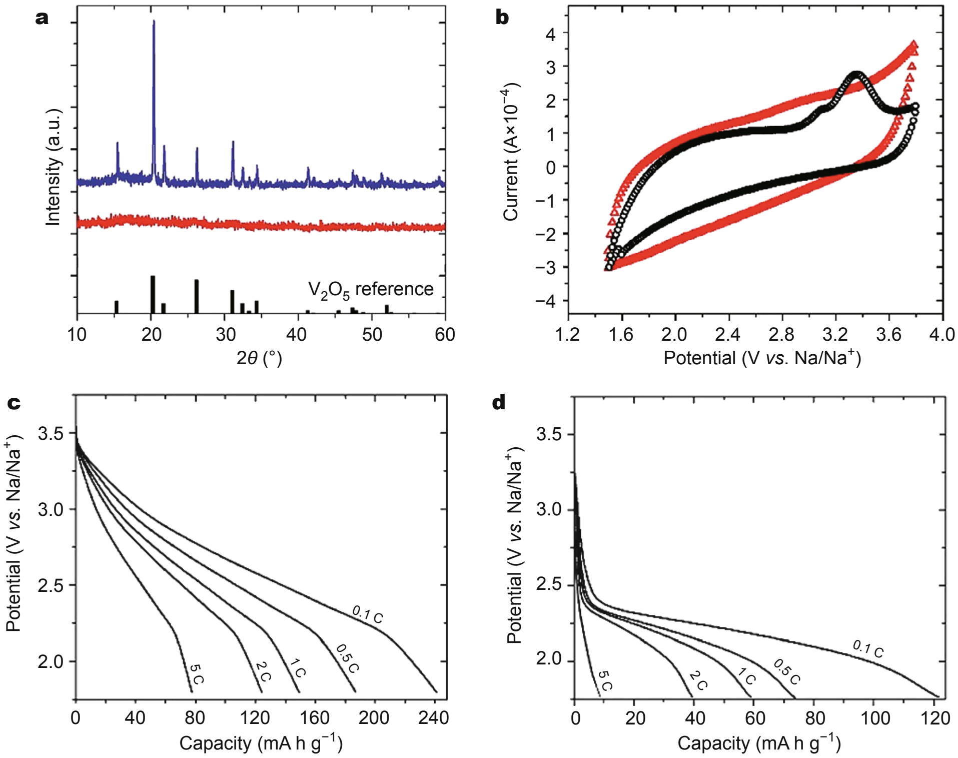

Figure 3 (a) XRD spectra (with V_2O_5 reference) and (b) CV plots (collected at 1.0 mV s^{-1}) for the amorphous (red) and crystalline (black) V_2O_5; the rate capability of the (c) amorphous and (d) crystalline V_2O_5 when discharged at current densities ranging from 23.6 (0.1 C) to 1170 mA g^{-1} (5 C). Reproduced from Ref. [44] with permission, Copyright 2014, Royal Society of Chemistry.

In a separate investigation, crystalline water was incorporated into the V_2O_5 lattice via the intercalation of water molecules. While well known as a technique for bolstering the performance in Li-ion setting, the new study was found to work for NIB application as well [45–47]. The hydrated $V_2O_5 \cdot nH_2O$ cathode, where $n = 0.55$ as derived from thermogravimetric analysisn (TGA), displays excellent sodium storage capability of 338 mA h g^{-1} at a current density of 50 mA g^{-1}, which is much higher than pristine, orthorhombic V_2O_5. More interestingly, cyclic voltammetry (CV) characterization showed that a capacitive charge storage mechanism accounts for a significant proportion of the total observed capacity, and actually becomes more prevalent as the scan rate incresaes. Moreover, it was determined that the crystalline water is not totally exchanged during cycling based on *ex situ* X-ray diffraction (XRD) and Fourier transform infrared (FTIR) spectroscopy analysis. Similar results have been recorded for sodiated MnO_2 where the incorporation of crystalline water enhanced Na ion diffusion both in the host and at the interface, suppressed fatal Mn^{2+} dissolution, and improved long-term structural stability [48]. These studies demonstrate that the optimized design of stable intercalation compounds could lead to substantial improvements for applications in energy storage appropriate by overcoming intrinsic limitations.

Layered $Na_xM_yO_2$ (M = Co, Ni, Mn, Fe, V, Cr, etc.) materials allow for high Na^+ ion diffusion between lamellar MO_6 slabs that are weakly attracted to one another; due to a direct overlap of the Co 3d orbitals, it is possible to achieve diffusion coefficients on the order of 10^{-11} cm^2 s^{-1} and metallic conduction approaching 300 S cm^{-1} at ambient temperature. The polymorphic phases of the compounds adopting this structure are often dictated by the preparation conditions such as Na^+ content, sintering temperature, and the atmospheric environment. The O3-$NaMO_2$ polymorph, with Na^+ ions occupying the octahedral holes between MO_6 slabs, is the preferred arrangement below sintering temperatures of 650°C. It is possible to form degenerate structures with decreasing Na content, where the O3-phase gradually transforms to O′3, P′3, and P3; however, all of these structures suffer from low electronic conductivity. In the P2-Na_xMO_2 polymorph, Na^+ ions are distributed in face- and edge-sharing trigonal prisms (as shown in Fig. 4), often under sintering temperatures exceeding 650°C. The migration of Na between the two sites is likely to be affected by the interactions between Na ions. Na-ion intercalation in P2-Na_xMO_2 is reversible because of the oxide interlayer gaps with no accompanying MO_6 slab slippage. Perhaps more simply, P (prismatic) and O (octahedral) signify the shape of the NaO_6 polyhedra while 2 and 3 denote the repetition unit perpendicular to the layers. However, these materials often suffer from rapid capacity-fading during cycling as dictated by the sodium content and interplay between cationic electrostatic interactions coupled with electroactive cation species charge ordering results in the formation of numerous Na^+/vacancy-ordered superstructures.

Through molecular dynamic simulations Mo *et al.* [50] showed that partially desodiated P2-Na_xCoO_2 is a fast Na ionic conductor while O3-Na_xCoO_2 also has good diffusivity, albeit an order of magnitude lower than P2-Na_xCoO_2. However, it was determined that Na-ion conductivity in P2 increases with Na content but decreases for the O3 phase. The activation barrier for single-vacancy migration was also determined to increase with sodium content as a result of the strong electrostatic repulsion between the nearest-neighbor Na ions. Furthermore, it was determined that divacancies are not a stable defects in P2 as is often the case in Li-containing analogues; rather, Na ions migrate via a honeycomb sublattice with relatively low energy barrier. There are strong electrostatic interactions among Na ions that are likely the dominant limiting factor for Na diffusion in P2. It was speculated that Na ordering is an additional factor that can limit Na migration at high Na concentrations. Our results show that P2-type layer oxide materials are promising cathode materials with good rate capabilities for NIBs. It was also proposed that it may be possible to perturb the ordering of the transition metal sublattice by incorporating distinct transition metal elements that weaken Na ordering.

Han *et al.* [51] were able to optimize the electrochemical cycling and rate performance of P2-Na_xCoO_2 by doping with Ca^{2+}. It was expected that Ca^{2+} would enhance the electrostatic interactions between CoO_6 slabs by fixing itself between them because of its comparatively larger ionic radius (1.00 Å) compared to $Co^{3+/4+}$ (0.61/0.53 Å). As expected, Rietveld refinement indicated that the Ca-doping induced a volume contraction while not noticeably varying Na^+ occupancy, implying that Ca^{2+} substitution for two Na^+ ions is an energetically favorable process. When cycled as cathode material for NIB, the Ca-doped materials showed none of the abrupt voltage changes that are known to accompany

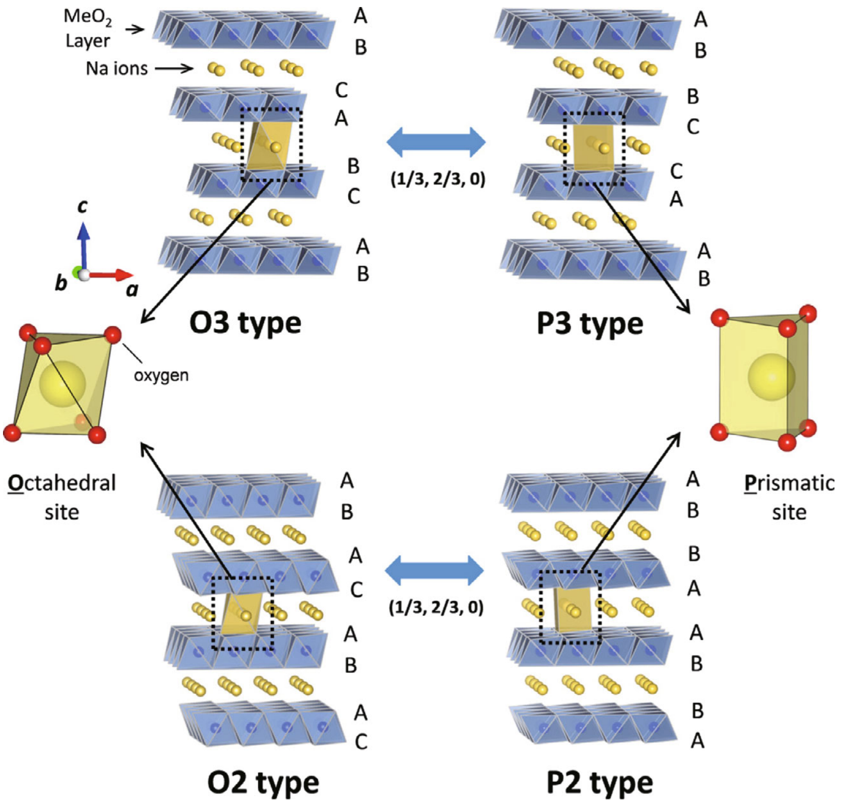

Figure 4 The classification of Na-Me-O layered materials with the sheets of edge-sharing MeO_6 octahedra and phase transition processes induced by sodium extraction. Reproduced with permission from Ref. [49], Copyright 2014, IOP Publishing.

Na-vacancy ordering [52,53]. While the Ca-doped samples did record a lower capacity value than the undoped counterpart, doping (up to $Na_{0.52}Ca_{0.10}CoO_2$) significantly improved both the cyclability and rate capability; $Na_{0.60}Ca_{0.07}CoO_2$ demonstrated negligible capacity fade over 60 cycles (~0.07 mA h g^{-1} $cycle^{-1}$) in contrast to the substantial decrease observed for $Na_{0.73}CoO_2$ (0.56 mA h g^{-1} $cycle^{-1}$), after which point it actually overtook the pristine material in terms of overall reversible capacity. It was reasoned that Ca-doping suppressed the formation of alternating biphasic and solid-solution domains by not permitting Na-vacancy ordering. The lack of Na-vacancy ordering also lent itself to more rapid diffusion over all Na concentrations, leading to the improved rate performance, as determined by potentiostatic intermittent titration technique.

Ceder's group [54] also went on to examine a multitude of Na_xCoO_2 polymorphic phases of varying stoichiometry synthesized under several conditions. Through *in situ* and *ex situ* XRD they were able to determine that the P2 can form with a relatively large variation in sodium content. Additionally, by pairing this data with electrochemical results, they revealed that the single-phase domains are considerably larger than previously expected and that precursor ratios are ill-suited for providing an accurate single-phase composition value. Shibata and colleagues determined the diffusion constant of Na ions in O3- and P2-type $NaCoO_2$ thin films through electrochemical impedance spectroscopy (EIS) [55]. It was noted that the diffusion constant values of Na^+ in $NaCoO_2$ (~0.5–1.5×10^{-10} cm^2 s^{-1}) are higher than those of Li^+ in $LiCoO_2$ (< 10^{-11} cm^2 s^{-1}). However, it was determined that the activation energy for Na-ion diffusion was prohibitively low in these layered cobalt oxides. The diffusion constant of O3-$NaCoO_2$ was higher than that of P2-$NaCoO_2$ because of the successive structural phase transitions from the O3, O′3, P′3, to P3. Such findings indicate that the (de)sodiation process can outperform expectations.

Hasa *et al.* [56] conducted a comparative study examining the role and impact of the Ni/Fe ratio, annealing temperature, and stoichiometric sodium content on the structural, morphological, and electrochemical properties of various Na_xMO_2 (M = Ni, Fe, Mn) compounds. The study was aimed at providing some insight as to why the intermixing of transition metals in MO_2-sheets can correspondingly improve the structural stability and electrochemical cycling performance. It was found that the final phase is more noticeably dictated by the annealing temperature employed and precursor material Na content, where higher levels of either often lead to P2 formation; it was reasoned that lower Na content reduces the repulsion between neighboring oxygen layers, but in turn leads to crystalline water intercalation in an attempt to reduce the overall energy. The Ni to Fe ratio was found to only moderately affect the P2 electrochemical performance in terms of capacity. The Ni-content alone was observed to strongly influence the working potential because of the Ni^{2+}/Ni^{4+} redox couple, with a double-electron process, invoking changes in the layer alignment and structural reorganization due to sodium vacancy ordering. It was further assumed that Ni doping stabilizes the structure via Mn^{3+} formation and hinders Mn dissolution, consequently improving the energy efficiency.

As has been shown for layered lithium compounds with nickel and one or multiple additional transition metal cations in LIB, the nickel redox reactions are the dominant species contributing to the overall capacity [57,58]. However, lower nickel content has been correlated with better capacity retention upon cycling. Additionally, it has been suggested that dense nanorod-structured assemblies could minimize contact area with electrolyte, in turn exposing less material to degradation in the acidic electrolyte (HF attack). With these considerations in mind Hwang *et al.* [59] designed radially aligned hierarchical columnar structure in spherical particles with varied chemical composition from the inner ($Na[Ni_{0.75}Co_{0.02}Mn_{0.23}]O_2$) to outer ($Na[Ni_{0.58}Co_{0.06}Mn_{0.36}]O_2$) regions of the structure. The transition metal concentrations varied over a radial nanorod distance of approximately 3 μm, and were detected and corroborated using atomic absorption spectroscopy and X-ray photoelectron spectroscopy (XPS). The radially aligned superstructure delivered a discharge capacity of 157 mA h g^{-1} at 15 mA g^{-1} and a capacity retention of 80% (125 mA h g^{-1}) over the course of 300 cycles. The comparatively high capacity and stability was possible because of gradient structure where the inner and outer regions support the $Ni^{3+/4+}$ and $Ni^{2+/3+}$ redox couples, respectively. Bulk material of the nominally averaged composition exhibited a slightly lower initial capacity but underwent substantial capacity fade with each cycle. Moreover, the redox peaks detected via dQ/dV after 100 cycles were preserved for the superstructure but were attenuated for the bulk sample. These findings demonstrate how structural and chemical control can be implemented to utilize the $Ni^{2+/3+/4+}$ redox reaction for Ni-rich O3-type layered compounds, and showcases the advantages of the radially aligned columnar structure.

Layered oxides have been the linchpin of the electrode materials for some time now and have been meticulously studied for the LIB system. However, when implemented in NIB, they often suffer from lower Na^+ ion diffusion coefficient and reduced dimensionality of ionic transport as dictated by cycling-induced ordering events [60,61]. The generally accepted types of ordering include: transition metal ordering, charge ordering, and Na^+/vacancy ordering, all of which affect one other. Na^+/vacancy ordering deriving from strong Na^+-Na^+ interaction in the alkali metal layer and charge ordering in the transition metal layer leads to the formation of localized superstructures that effectively limit the Na^+ ion transport kinetics and cycle performance. Wang *et al.* [62] avoided this issue by implementing a cation-disordered structure composed of transition metal ions with similar ionic radii but different redox potentials. The use of a disordered Cr^{3+} and Ti^{4+} arrangement in the transition metal layer prevents their eventual charge ordering that in turn inhibits Na^+/vacancy ordering. The novel composition of the $Na_{0.6}[Cr_{0.6}Ti_{0.4}]O_2$ electrode meant that it could be used as either cathode or anode. Capacities of 74 and 112 mA h g^{-1} were measured when cycled between 2.5–3.85 and 0.5–2.5 V (*vs.* Na/Na^+) corresponding to per formula unit sodiation levels of 0.26 and 0.4, respectively. The cathodic and anodic capacity retention after 200 cycles at 1 C was 94% and 90.4%, respectively. Neutron powder diffraction (NPD) confirmed that P2-$Na_{0.6}[Cr_{0.6}Ti_{0.4}]O_2$ with sodium content varying between 0.33 and 1.0 is Na^+/vacancy-disordered, thereby lending to the high ionic conductivity and ability to withstand high current densities. Electron energy loss spectroscopy (EELS) and X-ray absorption spectroscopy (XAS) examination clarified that the $Cr^{3+/4+}$ redox couple is responsible for the charge compensation on desodiation whereas the $Ti^{4+/3+}$ redox couple is involved in the charge compensation during sodiation. This contribution highlights the importance of designing disordered transition metal arrangements that prevent Na^+/vacancy ordering by halting charge ordering in the transition metal layer. This strategy lends a simple way towards achieving electrode materials with high power density and long cycle life.

Polyanion compounds

Contrary to the LIB system, alkaliated olivine $FePO_4$ is not stable and cannot be synthesized by conventional synthetic routes for NIB application [63,64]; however, maricite $NaFePO_4$ is generally regarded as thermodynamically stable and does merit investigation [65]. Kim *et al.* [65] combined computational and experimental findings to identify the mechanism responsible for the electrochemical activity of maricite $NaFePO_4$. XRD and extended X-ray absorption fine structure (EXAFS) made clear that the first desodiation step effectively amorphizes the initially crystalline maricite $FePO_4$ structure because of the kinetic limitations of Fe atoms to migrate at room temperature. The random and disordered diffusion pathways of amorphous $FePO_4$ afforded, as determined through quantum mechanical computations, significantly lower activation energy than maricite or olivine $FePO_4$ where diffusion is limited to one-dimensional tunnels along the *b*-direction. Similarly, previous reports concerning amorphous $FePO_4$ have demonstrated that a solid-solution behavior is observed during the dis/charge process [66,67]. Ultimately, the amorphous transformation is the key mechanism by which reversible cycling can proceed because it allows for substantially smaller Na migration barriers, and provides insight on the governing mechanisms behind a potential candidate for low-cost Na ion battery cathodes.

Open framework polyanionic materials have been steadily gaining interest for the past several years. Such investigations have focused on utilizing transition metal species with multiple redox chemistries, the potential of which can be enhanced and roughly tuned, due to the inductive effect of polyanionic species, by incorporating highly electronegative fluorine in the structure. When compared to their transition metal oxide counterpart, polyanionic materials often have a more stable potential response concurrent with (de)sodiation, allocate for superior capacity retention because of their structural energetics and robust frameworks, and are insensitive to ambient atmosphere [68]. Kundu *et al.* [69] synthesized $Na_4NiP_2O_7F_2$ with a three-dimensional open framework that can be readily implemented as NIB cathode material. Interatomic potential-based atomistic simulation methods indicate rapid Na ionic diffusion is expected in all three dimensions with a low activation barrier, and is validated by temperature-dependent ionic conductivity measurements. Use of an ionic liquid electrolyte allowed electrochemical examination at relatively high potential, however the cell was still plagued by oxidation at the cathode surface and parasitic redox reactions at the conductive carbon current collector interface. While the electrochemical performance was far from ideal, further exploration of this compound in an all-solid-state NIB is alluring, and such studies are expected to provide the impetus for the investigation of new sodium metal fluoropyrophosphate compounds as high voltage cathode materials for NIB.

Iron based open framework polyanionic compounds have also attracted considerable interest for their environmental benignity and inexpensive cost, and many ~3 V Fe-based phosphate (PO_4^{3-}) insertion compounds have been reported. Phosphate materials have been pursued as replacement for oxygen containing species because the voltage of many layered oxides is intrinsically self-limited by the top energy of the O 2p bands. Similarly, materials with even higher electrode potential can be realized by replacing phosphate with sulfate (SO_4^{2-}), thus taking advantage of higher electronegativity. Barpanda *et al.* [70] reported on an alluaudite-type sulfate framework compound ($Na_2Fe_2(SO_4)_3$) that registered the highest-ever $Fe^{3+/2+}$ redox potential at 3.8 V *vs.* Na/Na$^+$ along with fast rate kinetics; this is the first documented report of this material with the given structure. Rietveld refinement and Mössbauer spectroscopy detected trace amounts of Fe(III) impurity phase while revealing that the compound forms a three-dimensional framework (unrelated to the NASICON structure) with large tunnels along the *c*-axis. An initial reversible capacity of 102 mA h g^{-1}, corresponding to 85% of theoretical 120 mA h g^{-1} (one-electron) capacity, was possible at 6 mA g^{-1} and the rate dependence was highly reversible over 30 cycles when cycled under various current rates. These findings testify $Na_2Fe_2(SO_4)_3$ as a possible candidate for economical production at scale, and paves the way for a new sub-group of polyanionic cathodes and the discovery of sustainable cathode materials.

Chevrel phases

The Chevrel phase is a promising insertion type host that is capable of inserting a univalent (Li$^+$, Na$^+$, Cu$^+$) or bivalent (Zn^{2+}, Cd^{2+}, Ni^{2+}, Mg^{2+}) cation within the Mo_6T_8 (T = S, Se) framework. The Chevrel phase is most aptly characterized by its open and rigid framework comprised of Mo_6-clusters within anion cubes that allocates for intrinsically high electronic conductivity. Saha *et al.* [71] investigated the Mo_6S_8 and Mo_6Se_8 phases as positive electrode material within the voltage range of 1.2–2.2 V *vs.* sodium. It was revealed that electrochemical sodiation into the Mo_6S_8 phase proceeds via a two stage reaction accompanied by phase transformation from the initial Mo_6S_8 phase to $Na_2Mo_6S_8$ and then $Na_{3.7}Mo_6S_8$. However, an irreversible process would take place and the original phase could only be returned to $Na_1Mo_6S_8$, although it remains stable afterwards. Sodiation of Mo_6Se_8 progressed similarly to its chalcogen counterpart albeit at slightly lower voltages and a final composition of $Na_{3.3}Mo_6Se_8$; an irreversible reaction upon desodiation to $Na_1Mo_6Se_8$ was also observed. There was a gradual capacity fade for both systems because of Na ion trapping within two terminal compositions, but for the most part Mo_6S_8 was stable after the first cycle while Mo_6Se_8 would take an additional cycle to reach stability. Mo_6S_8 and Mo_6Se_8 delivered initial capacities of 108 and 69 mA h g^{-1} with Coulombic efficiencies of 68.3% and 71%, respectively. Mo_6S_8 could reach a stable capacity of 60 mA h g^{-1} up to the 50th cycle with low capacity loss per cycle (0.7%), while Mo_6Se_8 achieved a low but stable capacity of 35 mA h g^{-1} after the 20th cycle with high Coulombic efficiency of 99.33%. EIS conducted at 0.1 V intervals during (de)sodiation verified the partial charge trapping issue that coincided with an increase in charge transfer resistance. Despite the scientific issues yet to be explained and technical issues still to be addressed, the Mo_6T_8 (T = S, Se) Chevrel phases are promising as Na-ion positive electrodes given their ease of fabrication, stable capacity, and high Coulombic efficiency.

Negative electrode materials

There have been relatively few reports regarding anode materials for NIB. Hard carbon is not a realistic candidate for NIB application. Its voltage with respect to metallic sodium is too low thus resulting in sodium metal deposition which carries major safety concerns. Therefore, it is obligatory to develop new anode materials with high capacity that can operate at satisfactory potentials.

Graphite is the most commonly used anode material for LIB, but its application in NIB is severely limited. This is corroborated by recent theoretical calculations supporting that the minimum interlayer distance necessary for Na$^+$ ion insertion is 0.37 nm (the interlayer distance of graphite ~0.34 nm) [72]. Recently, many carbon nanostructures and derivatives have been receptive towards Na$^+$ insertion, but they rely on the presence of graphite nanocrystallites and nanovoids, which is less than ideal seeing as the later only takes place over a narrowly low potential range [73].

First-principles calculations regarding Na adsorption on graphene with various percentages of divacancies (the most common type of vacancy defect observed) and Stone-Wales defects show that adsorption is not possible for pristine graphene [74]. However, the presence of defects enhances the adsorption, and the potential is larger when the adatoms are on and/or around the defective zone. With the increase in defect density, the maximum capacity obtained is much higher than that of graphite and increases with the density of the defects. For the Stone-Wales and maximum possible highest density divacancy defects, capacities of 1070 and 1450 mA h g^{-1}, respectively, can be achieved. The divergence in performance from pristine graphene is due to changes in the bonding charge distribution leading to enhanced charge transfer. Similar findings were observed for Li and Ca adsorption (Fig. 5) [74–76], and such findings have been experimentally verified in half-cells by other groups [77].

Expanded graphite was produced by initially forming graphite oxide that was then partially reduced to limit the large amount of oxygen containing groups that sterically hindered the sodiation process. When tested, the expanded

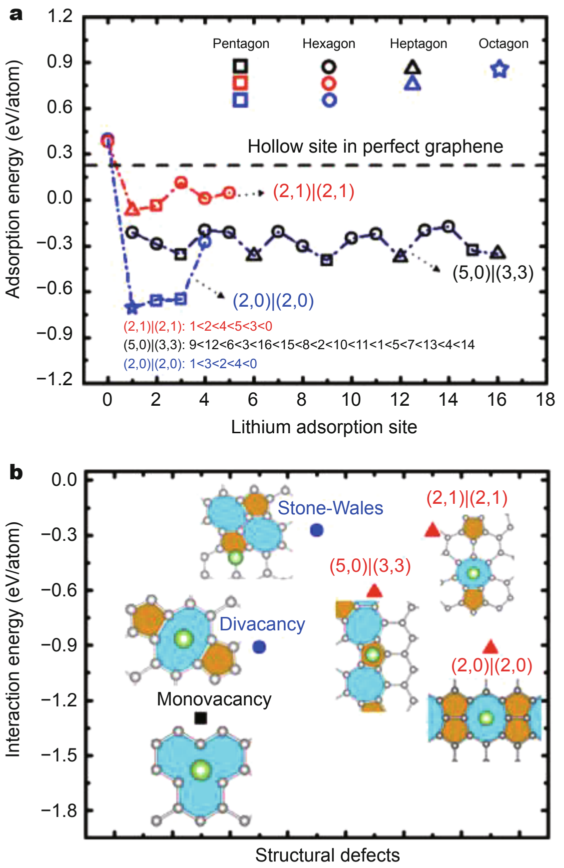

Figure 5 (a) The adsorption energy of a Li adatom on different sites in the boundaries. (b) Interaction energy of a Li adatom with different structural defects such as a monovacancy, divacancy, Stone–Wales defect, and grain boundaries of several orientation. Insets are the local atomic structures for the most stable adsorption sites of a Li adatom on these five structural defects. Reprinted with permission from Ref. [75], Copyright 2014, American Chemical Society.

graphite delivered a high reversible capacity of 284 mA h g^{-1} at a current density of 20 mA g^{-1}, with superior capacity retention (73.9% after 2000 cycles at 100 mA g^{-1}) [78]. The defects enhance sodiation because of the strong ionic binding energy between the Na^+ ions and the defects, which effectively overcomes the van der Waals (vdW) interaction between graphene sheets. Moreover, larger interlayer distances and defects may account for both the sloped and flat regions observed in the potential profiles of disordered carbons [79].

Adsorption/binding energies of isolated Na atoms on graphene-like materials are often reported, but fail to take into consideration competition between adsorption and plating that provides a more complete understanding of graphene-based materials in the context of NIBs. Additionally, many studies do not include vdW force corrections that often yield lower binding energies and migration barriers. Malyi *et al.* [80] showed through computational analysis that 1) graphene is not an attractive anode for NIBs, 2) Na-Na interaction plays an important role in Na diffusion, and 3) defects can improve Na storage significantly. Density functional theory (DFT) analysis of pristine graphene showed that: Na atoms have a tendency to adsorb on H adsorption sites, the electron density around the Na atoms is effectively reduced, and increasing Na concentration during sodiation results in strong Na-Na interactions that directly impact the electrochemical performance. The increase of Na concentration results in spontaneous formation of Na complexes and a reduction of Na-graphene strength. Moreover, the Na-Na interaction is found to affect Na diffusion significantly and to produce a significant reduction of Na migration barriers. The culmination of these findings reveals that pristine graphene is not suited for application as NIB electrode material. Contrary to this, defected graphene systems show improved Na adsorption that preferentially takes place near the defects. Diffusion is also improved in defected systems; for instance, the migration barriers for Na diffusion at vacancy and divacancy graphene systems are significantly larger than those for ideal graphene. These findings all indicate that Na-Na interaction needs to be taken into account during electrode material design and development.

Graphene foam doped with 6.8 at.% nitrogen was prepared by annealing freeze-dried graphene oxide foams in ammonia [81], which has potential for low cost and large-scale production. XRD peak analysis established that the *d*-spacing for the doped foam was slightly larger than conventional graphite. The N-doped graphene foam showed considerably improved charge capacities and capacity retention compared to reduced graphene foam and nanostructured graphene. The charge capacities for these three materials (at the indicated C-rates) were 1057.1 (0.2 C)/ 137.7 (10 C), 707.4 (0.2 C) / 10.3 (10 C), and 809.4 / 10.5 (10 C) mA h g^{-1}, respectively. The charge capacity retention after 45 cycles at 10 C for the doped material (13%) was also higher than those for the nanostructured graphene (1.5%) and reduced graphene foam (1.3%). The observed boost in performance of the N-doped graphene foam was attributed to synergistic effects associated with the well-defined mesoporous structure, large surface area, and enlarged lattice spacing between graphene layers coupled with the N-doping-induced defects. These findings indicated that heteroatom-doping induced defects can tremendously affect material structure and performance, the optimization of which should always be taken into consideration.

Recently, there has been discord regarding the method through which sodium ions are incorporated into anatase TiO_2. Several studies have proposed contrasting mechanisms based on pseudocapacitive, amorphization, and intercalation as the primary method of Na-ion incorporation [82–84]; however, all studies agree that Na-ion incorporation in anatase TiO_2 is reversible. Wu and colleagues [85] utilized a slew of methods towards elucidating this (de)sodiation mechanism for which there seems to be no consensus using a commercial sample of nanoparticulate anatase TiO_2. *In situ* XRD analysis was conducted to examine the structural changes of the active material upon sodium metal ion uptake and release within the voltage range of 0.1−2.0 V. Fig. 6a indicates the three distinct sections in the discharge curve, representative of three successive Na-ion incorporation mechanisms: pseudocapacitive (15 mA h g^{-1}), intercalation (100 mA h g^{-1}), and amorphization paired with structural rearrangement (250 mA h g^{-1}). Nearly all the anatase-related reflections were depleted after initial discharge and failed to reappear upon subsequent charge. *Ex situ* scanning electron microscopy (SEM) analysis revealed that there was a decomposition product formed during the initial discharge cycle which disappears upon charging. Energy dispersive X-ray spectroscopy (EDS) analysis confirmed that the product was not formed due to electrolyte decomposition and was most likely amorphous NaO_2 (sodium superoxide). *Ex situ* XPS of discharged material detected both Ti^{3+} and metallic Ti^0 (~19 at.%) peaks, with the metallic phase predominately limited to the particulate surface. This suggests that only a portion of the sodium ions can be inserted into the anatase host structure while the remainder reduce anatase TiO_2 to the metallic state. *In situ* gas chromatography and mass spectrometry (GC-MS) analysis demonstrated that oxygen evolution steadily increased during discharge while CO_2 evolution (electrolyte decomposition) was steady (Fig. 6b). Thus, combining these results, it appears that sodium is able to partially reduce anatase TiO_2 to the metallic state while sodium oxide and an amorphous sodium titanate phases are simultaneously formed. When electrochemically cycled, the newly formed amorphous sodium titanate phase was able to reversibly (de)insert approximately

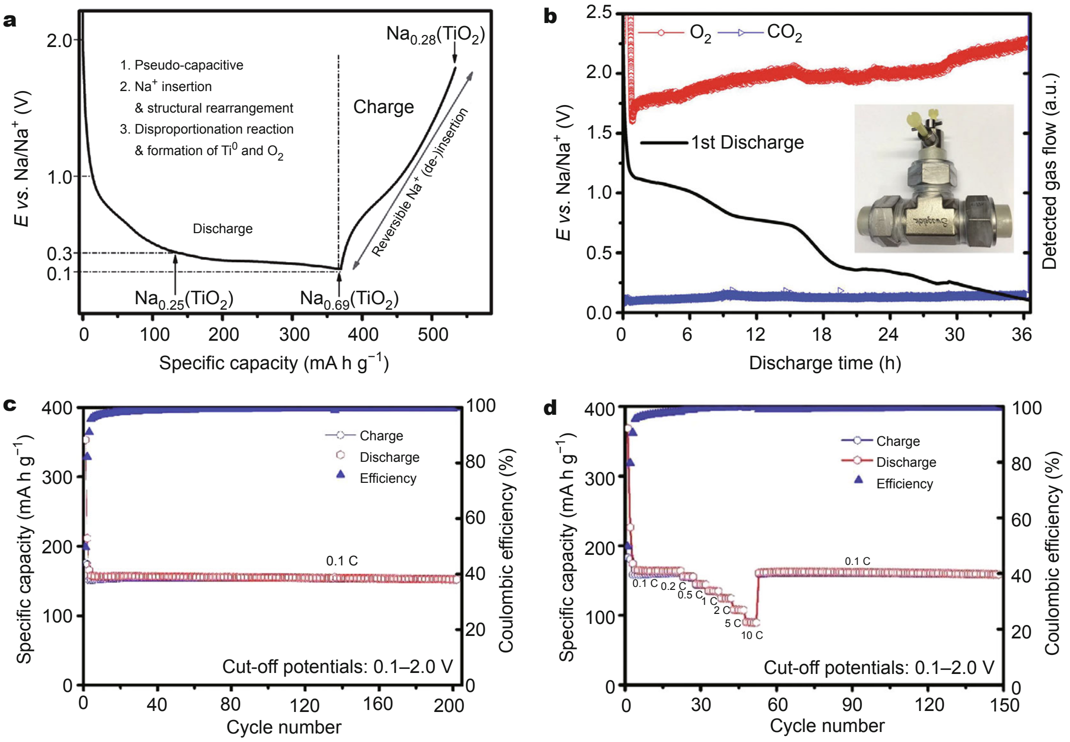

Figure 6 (a) Potential profile for the first full cycle of anatase TiO_2 at 0.01 C including the proposed reaction mechanism and composition of newly formed titanate phase at 0.3, 0.1, and 2.0 V. (b) *In situ* GC-MS analysis of evolving gaseous products formed upon the initial discharge of anatase TiO_2 electrode (C/30; lower cut-off potential: 0.1 V); inset: photograph of the GC-MS *in situ* cell. Galvanostatic cycling of TiO_2 electrodes: (c) two formation cycles at 0.01 C, followed by constant current cycling at 0.1 C within the potential range of 0.1 to 2.0 V; d) at increasing C-rates. Reprinted with permission from Ref. [85], Copyright 2015, John Wiley & Sons.

0.41 sodium per TiO_2 formula unit, providing a reversible specific capacity of roughly 140 mA h g^{-1} that is quite stable and capable of handling high current density (Figs 6c and d). Clearly the newly formed amorphous sodium titanate phase is the major source of the observed sodium ion storage capability, and exhibits stable long-term cycling performance, excellent high rate capability, and superior Coulombic efficiency, thereby showcasing its potential as an NIB anode material.

Legrain *et al.* [86] conducted a computational study comparing the alkali-ion insertion energetics of anatase, rutile, TiO_2(B), and amorphous TiO_2. Their results showed that TiO_2(B) provides the most favorable Na-ion insertion sites among the TiO_2 crystalline phases with a defect formation energy of −1.96 eV *vs*. metallic Na reference. Furthermore, the results revealed that the amorphous structure exhibits a distribution of insertion site energies, with the lowest being more favorable than crystalline TiO_2(B) by 1 eV. Experimentally, the use of amoprhous TiO_2 has also proven beneficial for NIB application over its crystalline counterpart both in terms of capacity and rate capability by Xiong *et al*. [42]. The capacity of amorphous titanium dioxide nanotube electrodes improves with cycling, eventually reaching a maximum of 150 mA h g^{-1}. CV and power law relationships were utilized to determine the storage processes at play. It was found that the discharge process starts as a mainly capacitive-limited mechanism that converts to a mixed contribution (diffusion and surface capacitance) as the potential drops below a certain threshold. Observation of the pre-edge X-ray absorption near edge structure (XANES) feature suggested an increase in the structural disorder upon Na^+ intercalation, but this eventually reached a saturation point that coincides with the maximum capacity attainable. It was further speculated that the capacity becomes limited as some of the intercalation sites remain inaccessible and some of the Na ions are irreversibly stuck in the structure. Nb-doping was also proposed as a potential means towards improving sodiation capability by suppressing the coarsening of TiO_2 grains through grain boundary segregation, thereby yielding nanoparticles [87]. These results highlight some of the potential, and oftentimes unexpected, differences that can arise from the use of amorphous electrode materials.

Nanosized $FeSb_2$ was synthesized through ball milling and compared with Sb [88]. The iron containing material successfully sustained a reversible capacity exceeding 540 and 440 mA h g^{-1} for more than 130 cycles at current densities of 36 and 300 mA g^{-1}, respectively. While exhibiting a lower capacity at low current rate, the alloy actually overtakes Sb in terms of cyclability at high rate as demonstrated by the measured polarization. A rise in polarization represents an increase in impedance and (reversibly) increases with the cycling regime for intermetallic electrodes. This is because of reaction kinetic limitations caused by the restructuring and the decrease of the particle size (electrochemical grinding). $FeSb_2$ and Sb showed analogous polarization at low current density, but the $FeSb_2$ demonstrated a lower polarization at higher rates relative to Sb. Moreover, there was an overall irreversible increase in the overall degree of polarization for Sb that was not observed for $FeSb_2$. Preliminary *in situ* XRD analyses suggest that, after the formation of an amorphous intermediate, a conversion reaction takes place during the first discharge, presumably leading to the formation of nanoparticles of metallic iron embedded in the Na_3Sb matrix. The formation of nanosized Fe-particles was confirmed by Mössbauer spectroscopy where superparamagnetic behavior was observed in the discharged state; superparamagnetism is typical of nanosized magnetic domains usually observed when the particle size is smaller than 3 nm. The spectrum collected at the end of the charge process is identical to that obtained for the fully discharged electrode, clearly showing that iron particles formed during discharge and are not involved in the charge process. Ultimately, it was reasoned that the presence of Fe in the electrode is beneficial because of its homogenous distribution which can effectively increase the electronic percolation within the electrode and thereby enhance the kinetics.

Micro-sized particles of O3-type $NaTiO_2$ were synthesized via solid-state reaction using metallic sodium to reduce anatase TiO_2 [89]. Within the 0.6–1.6 V potential range $NaTiO_2$ delivers a specific capacity of 152 mA h g^{-1} and retains 98% of its initial capacity after 60 cycles at a rate of 0.1 C. *In situ* XRD confirmed that the (de)sodiation process propagated through a reversible O3 to O3′ phase transition. These measurements also revealed that the interslab *d*-spacing and Ti-Ti separation distances actually decreased during the sodiation process. Paired with the obtained differential capacity curves, it was concluded that most regions are single phase with a smooth voltage profile while the two-phase reaction is limited to a short plateau where the O3 transforms into O3′ via monoclinic distortion; it was further suggested that the O3′ region is actually composed of three domains with different superstructure modulations and that Na^+/vacancy ordering and second-order phase transitions were responsible for the unusual variations in lattice parameter (which typically remain constant in the biphasic domain). These findings should not be limited to titanium-containing systems, and provides a new manner of insight towards the design of layered intercalation materials.

Chen *et al.* [90] prepared a graphene-coupled TiO_2 sandwich-like hybrid by rapid microwave-assisted *in situ* reduction-hydrolysis route. Ambient calcination removed the residual organics and improved crystallinity. At the same time, the titanium species was transformed to a composite of TiO_2(B) and anatase TiO_2 as confirmed by XRD and Transmission electron microscopy (TEM). Electron paramagnetic resonance and XPS results suggested that the TiO_2 nanoparticles, rather than adhering simply via physisorption, are chemically bonded with the graphene matrix. The potential profiles are sloping curves with a final discharge capacity of 149 mA h g^{-1} when cycled at 500 mA g^{-1} with negligible polarization. The rate performance was quite commendable where reversible capacities of 265, 187, 149, 125, 114, and 102 mA h g^{-1} were delivered at 50, 200, 500, 1500, 3000, and 6000 mA g^{-1}, respectively. Additionally, reversible capacity of 120 mA h g^{-1} can be maintained for more than 4300 cycles at a current rate of 500 mA g^{-1}, clearly attesting to the superior long-term cyclability of the hybrid material. The power law relationship between the peak current and the scan rate was used to determine the diffusion-controlled and capacitive process contributions to the overall capacity. The findings gathered from sweeping at a range of scan rates indicated that the capacitive contributions are independent of the scan rate, but the sodiation process does eventually become diffusion limited at higher rates. Thus, the comparatively excellent rate capability and long-term stability can be ascribed to an intercalation pseudocapacitance mechanism that dominates the charge storage process. The sodiation dynamics were analyzed utilizing first-principle calculations and revealed that the hybridization of graphene with TiO_2 provides a more feasible sodium transport channel along the hybrid interface. This gives rise to a much lower activation energy and thus diffusion energy barrier, and ultimately enhances the Na^+ intercalation pseudocapacitive process. The design of such structures exploiting pseudocapacitance represents a promising strategy for developing electrode materials with high power density and long cycle life which merits further investigation.

Spinel-type electrodes for NIBs have rarely been investigated. $Na_2Ti_3O_7$ suffers from sodium plating, which poses a safety hazard, in addition to hysteresis and the poor cycling performance, and there exists a general consensus that Na ions are too large to fit in spinel host tetrahedral sites [30,40]. However, Sun *et al.* [91] demonstrated that sodiation can reversibly proceed via occupation of the spinel host octahedral sites through a three-phase separation mechanism. Initially, an array of high tensile-strength binders were used to optimize the electrode and abate any capacity fading that could result from volume expansion during sodiation. A carboxymethyl-cellulose sodium-based binder system yielded a stable capacity of 155 mA h g^{-1}, a Coulombic efficiency exceeding 99%, and an excellent cyclic stability after several cycles. Galvanostatic intermittent titration further confirmed that $Li_4Ti_5O_{12}$ has an average potential of 0.91 V for sodium storage. *In situ* synchrotron XRD, first-principles calculations, and scanning tunnelling electron microssopy (STEM) imaging elucidated the sodiation mechanism which was rationalized to take place through a three-phase separation process. Three Na ions can be inserted into one formula unit of $Li_4Ti_5O_{12}$ where it will occupy the 16*c* vacancy site which drives the Li ion at the 8*a* site into the 16*c* site due to the Coulombic repulsion. However, the material will at this point separate into two rock salt phases because of the two differently sized alkali ions, with a single alkali species at the 16*c* site. The phase boundary will correspondingly propagate during sodiation and push forward, and is reversible; no lithium release was detected after cycling. This finding brings new insight and perspective on the design of electrode materials by understanding the electrochemical process and Na-ion storage mechanism in $Li_4Ti_5O_{12}$.

As a negative electrode material, the zero-strain characteristics of layered P2-type $Na_{0.66}[Li_{0.22}Ti_{0.78}]O_2$ ensure a potentially long cycle life with only 0.77% volume change during (de)sodiation [92]. Furthermore, P2-$Na_{0.66}[Li_{0.22} Ti_{0.78}]O_2$ exhibits an average potential of 0.75 V and an apparent Na^+ diffusion coefficient of 10^{-10} cm^2 s^{-1}. The monotonically decreasing voltage profile, indicating that sodium insertion occurs through a solid-solution reaction, contradicts other P2-type electrodes where multiple plateaus are often observed; this behavior can be ascribed to the random distribution of Li in the transition metal layer. At current densities of 10.6, 21.2, 58, 106, and 212 mA g^{-1} the reversible capacities were 116, 106, 90, 77, and 62 mA h g^{-1}, respectively. When utilized in a full cell, a capacity of 100 mA h g^{-1} is realized. It was concluded on the basis of *in situ* XRD analysis that the final sodiated product consists of several P2 phases with slightly varying Na content and occupation. There can be no contributions to the overall capacity from lithium as their diffusivity coefficient is negligible because the connecting path through the TiO_6 octahedra is prohibitively small. Capacity retention of 75% over 1200 cycles demonstrated the long cycle life of this electrode material, which could show promise upon further optimization.

Wang *et al.* [93] demonstrated that Ti doping of tunnel-structured $Na_{0.44}MnO_2$ yields a negative electrode material for aqueous NIBs. There are five distinct manganese crystallographic sites in the $Na_{0.44}MnO_2$ structure as induced by charge and order preservation: Mn(1), Mn(3), and Mn(4) sites are occupied by Mn^{4+} whereas Mn(2) and Mn(5) sites are occupied by Mn^{3+}. On the framework level, the structure is composed of double and triple rutile-type chains of edge-sharing MnO_6 octahedra and single chains of corner-sharing MnO_5; there are three different sodium sites and corresponding paths that must be traversed because of these polyhedral units. The $Na_{0.44}[Mn_{1-x}Ti_x]O_2$ unit cell volume was found to expand as a result of Ti substitution, and the maximum achievable stoichiometry was $x = 0.44$ where Ti would occupy mostly Mn(1), Mn(3), and Mn(4) sites; as revealed through DFT calculations, XRD, and STEM. When cycled in nonaqueous (0.1 C) and aqueous (2 C) half-cell configurations, the discharge capacity for the pristine and Ti-substituted samples was 100/32 and 110/37 mA h g^{-1}, respectively, where 1 C = 126 mA g^{-1}. Multiple plateaus were observed during (de)sodiation for the unsubstituted $Na_{0.44}MnO_2$ for both electrolyte systems due to a series of phase transitions and vacancy ordering; however, these plateaus gradually dissipated and adopted a sloped profile with increasing Ti content. Finally, XAS was conducted to determine the electrochemically active species, which could shed light on the active diffusion paths the Na ion must undertake. The Mn spectrum of the as-prepared $Na_{0.44}MnO_2$ powder recorded 42% Mn^{3+} and 58% Mn^{4+}, while Ti substitution to $Na_{0.44}[Mn_{0.44}Ti_{0.56}]O_2$ reduces the manganese oxidation states to 67% Mn^{3+} and 31% Mn^{4+}. Further XAS analysis concluded that Mn^{4+} ions at Mn(3) sites are first reduced to Mn^{3+}, and then Mn^{3+} ions at Mn(2) sites are further reduced to Mn^{2+}. Thus, Ti substitution alters the charge compensation mechanism sodiated manganese oxide. These findings provide new insight on the grand effects that small material substitutions can have, and validates $Na_{0.44}[Mn_{1-x}Ti_x]O_2$ as a negative electrode material for aqueous NIB.

Elemental phosphorus (P) is a particularly attractive anode material provided its natural abundance, environmental benignity, and ability to react with three Na atoms to form Na_3P giving a theoretical specific capacity of 2035 mA h g^{-1}. Qian *et al.* [94] prepared an amorphous phosphorus-carbon nanocomposite that delivered a high sodium ion storage capacity of 1764 mA h g^{-1} and considerable retention over 100 cycles. Kim *et al.* [41] did the same with amorphous red phosphorus and recorded a capacity of 1890 mA h g^{-1} with negligible capacity fading over 30 cycles and extremely low redox potential. However, black phosphorus is the most stable of the three phosphorus allotropes (red, white, and black) and has a layered structure similar to graphite, but a greater interlayer distance (5.4 Å *vs.* 3.4 Å), consisting of phosphorene layers with AB stacking bound by vdW interactions. Black phosphorus also exhibits the highest bulk conductivity of these polymorphs and has a reversible capacity of 637 mA h g^{-1}. Hembram *et al.* [95] proposed an atomistic mechanism for the sodiation of black phosphorus based on first-principle calculations. It was determined that the sodiation of the layered spaces of black phosphorus induces changes in the layer stacking because of sliding of the phosphorene layers. Furthermore, P–P bond cleavage initiates above a critical sodium level. Sodiation beyond this point is eventually accommodated by the formation of an amorphous phase. Concurrently, the sodiation mechanism of black phosphorus shifts from predominately intercalation into the phosphorene layers to alloying with P atoms. The insights gathered from this study concluded that the improved performance of black phosphorus in NIBs relies on the conservation of the layered structure. One method towards maintaining this structure may be the use of phosphorus-carbon composites. The formation of stable phosphorus-carbon bonds would enhance the stability of the layered structure of black phosphorus. The complete understanding of the sodiation mechanism in black phosphorus will provide useful guidelines in designing new NIB anode materials.

Differing from the inorganic compounds typically used as secondary battery electrodes, organic electrodes are inexpensive and pliable, making them ideally suited candidates for future large-scale and flexible applications. Moreover, the implementation of π-conjugated systems is predicted to be conducive to fast charge transport/collection that would greatly benefit the (de)sodiation process. The extension of π-conjugated systems can also strengthen intermolecular interactions, potentially leading to layer-by-layer molecular arrangement that could expedite the diffusion between layers. Wang *et al.* [96] investigated the benefits of π-conjugated systems by comparing sodium benzene-dicarboxylate (SBDC) as starting molecule that was extended via a carbon-carbon double bond giving sodium 4,4′-stilbene-dicarboxylate (SSDC). When examined as an anode material for NIB at a current density of 50 mA g^{-1}, the SSDC and SBDC electrodes recorded second cycle capacities of 180 and 112 mA h g^{-1}, respectively; this is an even larger discrepancy considering the theoretical capacities for the two materials are 172 and 255 mA h g^{-1}, respectively, provided the differences in molecular weight. Additionally, the SSDC electrode showed enhanced high rate performance with reversible capacities of 105 mA h g^{-1} and 72 mA h g^{-1} at current densities of 2 A g^{-1} and 10 A g^{-1}, respectively, and was fully recoverable upon returning to low current density (Fig. 7). It was ultimately reasoned that

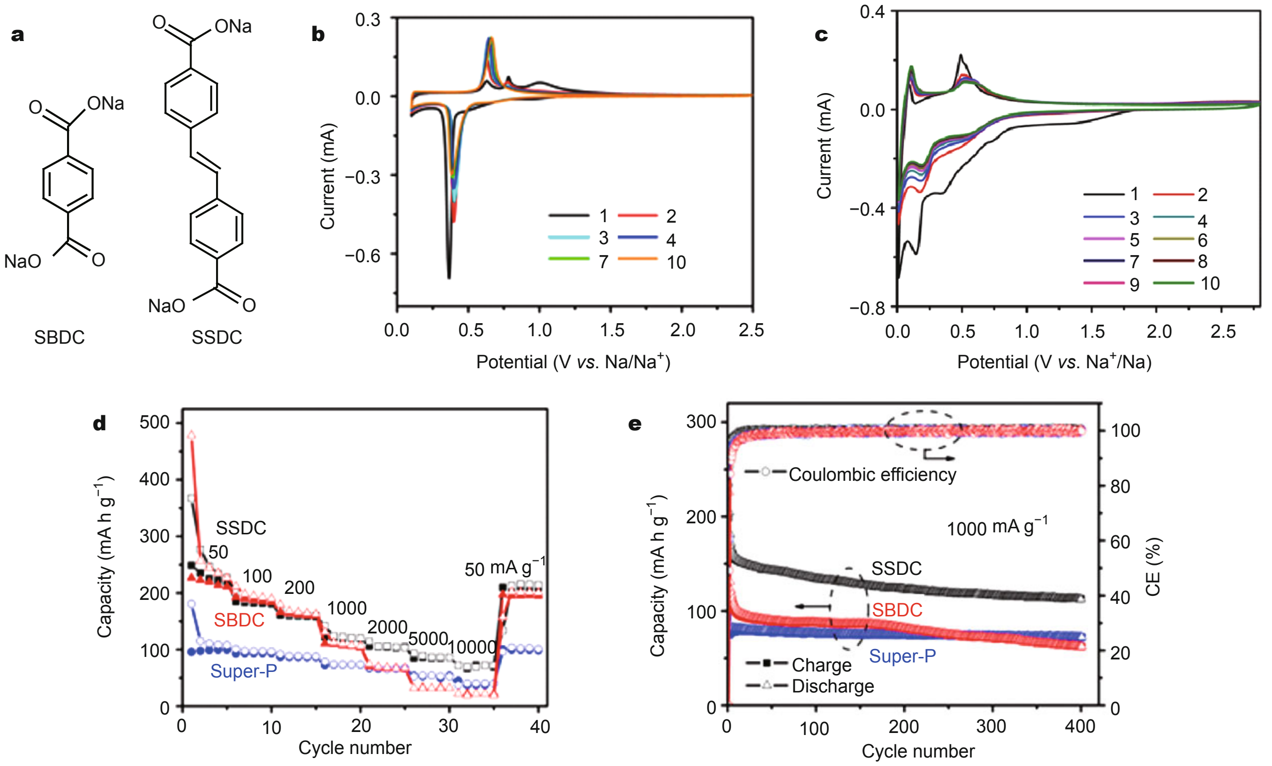

Figure 7 (a) Schematic chemical structure of the starting molecule SBDC and chosen double bond linkage to extend the π-conjugation forming SSDC. Typical CV curves of (b) SBDC and (c) SSDC films in the first 10 cycles. Electrochemical performances of super P, SBDC, and SSDC at: (d) various current rate and (e) cycle performance at 1 A g^{-1} (solid: charge, open: discharge). Reprinted with permission from Ref. [96], Copyright 2015, American Chemical Society.

π-conjugated systems can efficiently improve the high rate performance because of improved charge transport, more stabilized discharged/charged states, and enhanced intermolecular interactions that facilitate (de)sodiation. Thus, there are clearly functionalization steps that can and should be taken toward the design of high performance organic electrode materials.

Summary

Overall, NIBs are, at present, an up-and-coming technology brimming with much promise and intrigue. In theory, NIBs present a complementary alternative to Li-ion based systems with primary advantages rooted in cost and safety. However, the reignition of interest in this field has revealed, if not anything else, that analogous materials can behave substantially different than expected relative to their prior LIB performance. One of the main issues NIB electrodes face is the ability to successfully (de)intercalate Na$^+$ reversibly and with stability upon prolonged cycling. This poses a problem as sodium ions are substantially larger than their lithium counterparts, and thereby are much more intrusive and disruptive on the host material. Towards this end there is a host of potential materials well suited for such application, however their inherent qualities are oftentimes not enough and manipulative techniques must be employed in order to make the structure more receptive to the sodiation process. Ultimately, there is still much work to be done in the development of electrode materials better suited for sodium intercalation before NIBs can be implemented on a large scale.

MAGNESIUM-ION BATTERIES

As with NIBs, research into rechargeable magnesium-ion batteries (MIBs) is very much in its infancy. In spite of pioneering work by Gregory *et al.* [97] in the late 1980’s, progress in MIB research was scarce in the wake of the commercialization of LIBs by Sony in 1991. Then in 2000, Aurbach *et al.* [98] contributed key breakthroughs to the electrolyte and cathode materials that have since enabled more widespread interest in the subject. Nevertheless, the burgeoning MIB research activity (as evidenced by, for example, the rapid proliferation of review articles [26,27,31,32,99–108]) is more likely attributable to stagnating LIB progress than to any other factor.

There are several technical problems that have hampered the commercialization of MIBs. While most of the concepts are identical, Mg-ion electrochemistry does not have much direct carry-over from Li-ion research. In particular, the set of electrolytes that are conducive to Mg electrochemistry is much more limited than Li. On one hand, the common Mg analogs to Li-ion electrolytes (for example, salts like $Mg(ClO_4)_2$ and solvents like acetonitrile and propylene carbonate) will form passivating layers on Mg metal anodes [97,99,109]. This passivation layer is ionically insulating – in contrast to Li, where the solid-electrolyte interface layer is a Li-ion conductor – and reduces cycling performance. On the other hand, those electrolytes that are compatible with Mg have relatively narrow voltage windows. The family of organohaloaluminate/ether electrolytes (e.g., $Mg(AlCl_2BuEt)_2$ in tetrahydrofuran (THF), where the dichloro complex/ether electrolyte is herein denoted as DCC) reported by Aurbach *et al.* [98] support highly reversible stripping and plating of magnesium, but is only stable up to ~2.2 V (voltages are reported with respect to the reversible Mg/Mg^{2+} couple, unless otherwise indicated). The volatile solvent also has safety limitations associated with its low boiling point (66°C for THF), while chloride-containing electrolytes are corrosive towards common battery components [105,110,111].

Nevertheless, new advances may soon circumvent this problem. While commercially practical electrolytes may not be a reality yet, researchers have made tremendous progress in the electrolyte in the last fifteen years [104,107]. Notably, a recent trend to reduce chlorine content in electrolytes has enabled the discovery of noncorrosive electrolytes with good conductivity (>1 mS cm^{-1}), efficient Mg dissolution/deposition (>98% Coulombic efficiency) and anodic stability well beyond 3 V [110,112–114]. These developments are encouraging and should soon facilitate better exploration of high-voltage cathode materials.

The second major problem pertains to the cathode materials, which suffer from either slow solid-state diffusion kinetics or low total energy density. Slow transport kinetics are manifest in the form of large overpotentials and low intercalation levels [103,115,116]. Enhanced electrostatic effects from the divalent ion are usually cited as the culprit, but may be mitigated by the host's ability to delocalize electrons and change valence states [100,117]. While Chevrel phases are prototypical of the very small set of kinetically fast, long-term stable cathode materials demonstrated thus far (>2500 cycles, Fig. 8), their low voltage and theoretical capacity (~1.1 V, ~128.8 mA h g^{-1} for Mo_6S_8) make them uncompetitive compared to today's Li-ion cells [118].

Lastly, lower voltages are expected for magnesium batteries compared to Li batteries. The cell voltage may be expressed in terms of the Gibbs free energy as follows:

$$V = -\Delta G/nF, \tag{1}$$

where ΔG can be approximated as the difference in the Gibbs free energy between the pertinent cathode and anode reactions, n is the number of electrons transferred and F is the Faraday constant. At the negative electrode, the reduction potential of Mg is ~0.67 V more positive than Li (−2.37 and −3.04 V *vs.* standard hydrogen electrode (SHE), respectively [28]). In the case of ionic hosts as the positive electrode, insertion of Mg^{2+} (that is, formation of a Mg-rich phase) occurs at lower energies than the analogous processes for lithium. This is because the lattice energy becomes more negative upon insertion of the similarly sized, but divalent Mg^{2+} atom (cf. the Kapustinskii equation [103,119]). The combined effect is that magnesium cathode materials have been observed or expected to operate ~1 V lower than the same material in LIBs [120–123], although this does not take into consideration discrepancies in electrolyte solvation or co-intercalation effects.

Despite these challenges, Mg is attractive for a variety of reasons, as mentioned previously (Table 1). First, its raw materials are significantly cheaper and more abundant than Li. It is also much less reactive than either Li or Na, which eases constraints on safety and manufacturing. If transport limitations can be overcome, the voltage loss compared to Li is compensated by the fact that Mg delivers twice as much charge per atom.

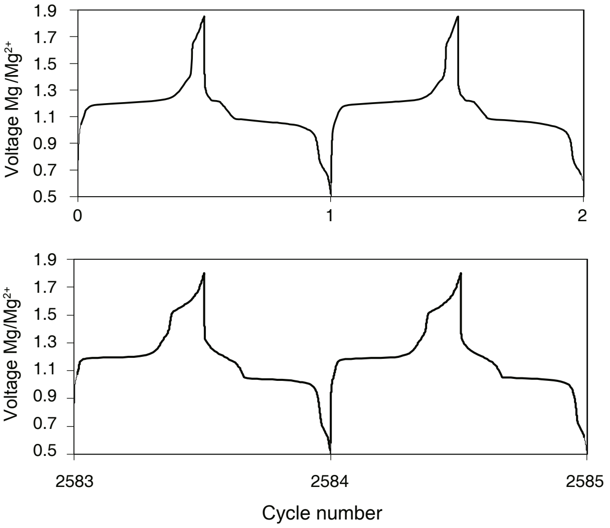

Figure 8 Voltage profiles for rechargeable Mg/Mo_6S_8 coin cells demonstrate excellent longevity. Reprinted with permission from Ref. [100], Copyright 2003, Japan Chemical Journal Forum and Wiley Periodicals, Inc.

Furthermore, the extremely high volumetric capacity (3832 mA h cm^{-3}) makes it an ideal prospective anode material for mobile devices and electric vehicle batteries, where space is at a premium. On the other hand, its energy density by weight (2205 mA h g^{-1}) is ~57% of Li. However, this is hardly a disadvantage in the absence of non-dendritic Li metal anodes, and is still far superior to today's graphite anodes. (Lithiated graphite, LiC_6, has a specific capacity of ~372 mA h g^{-1}, which corresponds to a volumetric capacity of ~800 mA h cm^{-3} depending on packing density.) A critical characteristic of magnesium, unlike lithium, is that stripping and deposition occurs without the formation of dendrites [124–126]. As such, anode materials may be superfluous if commercially practical Mg electrolytes are identified. (Aside: since we can use Mg metal as the anode, we can then refer to such devices as magnesium batteries rather than magnesium-ion batteries, often with "rechargeable" added to distinguish from primary Mg cells. Variations of these terms are used interchangeably in the literature to describe the same device.)

The remainder of this review contains a survey of the progress made in various rechargeable MIB cathode materials, with emphasis placed on the newest results in this rapidly accelerating field. We will identify avenues for further research, and highlight the importance of the other electrochemical cell components, which has been frequently overlooked.

Cathode materials

Transition metal chalcogenides (TMCs)

(i) Chevrel phases. The family of Chevrel phase materials (CP = $M_xMo_6T_8$ where M is a metal and T is a chalcogen) is the best characterized Mg-ion cathode material, having been the subject of many structural, kinetic, and thermodynamic studies [117,118,120,127–155] since Aurbach and coworkers showcased Mo_6S_8 [98]. Thousands of cycles with minimal capacity fading are possible with this material as a consequence of its structural features and the lack of side reactions between the electrolyte and either electrode. As such, it has been used as a good model system for characterization of MIB electrolytes [156–159]. However, as mentioned previously, its low energy density (projected to be ~60 Wh g^{-1} [98]) has hindered its implementation in a commercial MIB cell. Nevertheless, its long lifetime coupled with a wide operating temperature window (−20 to 80°C [98]) may enable its use in stationary energy storage applications, where high energy density is preferred, but not as critical as longevity [27].

The CP unit cell is composed of Mo_6 octahedra inside a cubic cage with S or Se atoms at each corner. Magnesium atoms can occupy twelve available sites formed in the channels between these building blocks. In Mo_6S_8, the twelve sites are themselves divided between two rings with six inner sites and six outer sites. Levi *et al.* [120] demonstrated that Mg inserts first into the inner sites, which is initially slow. In the case of Mo_6S_8, this insertion (discharge) reaction is given by Equation (2):

$$Mo_6S_8 + Mg^{2+} + 2e^- \rightarrow Mg_1Mo_6S_8. \tag{2}$$

Subsequent insertion into the outer sites occurs much faster and corresponds to the following reaction:

$$Mg_1Mo_6S_8 + Mg^{2+} + 2e^- \rightarrow Mg_2Mo_6S_8. \tag{3}$$

However ~23% loss in the charging capacity is observed at room temperature, and the final deinsertion step proceeds as slowly as the initial intercalation. This charge trapping is attributed to circular motion of Mg^{2+} in the inner ring, since Mo-Mg interactions create a large energy barrier to escape the low-potential inner ring sites [117]. Levi *et al.* [138] found that the improved mobility of Mg during the second reaction is a consequence of increased repulsion between Mg^{2+} ions. Apart from the charge trapping, the high mobility is related to the nature of CPs, where the 3D channels of closely spaced vacant sites prevent Mg^{2+} ions from occupying adjacent sites. Instead, the ions must diffuse into the bulk. Further, the ability of Mo_6 to easily accommodate four electrons per cluster helps maintain local electroneutrality, which in turn enables rapid intercalation kinetics [100,102]. Using alternative cluster compounds has been reported in the case of Mo_9Se_{11} [151], and clusters such as Fe_6, Co_6, and Cr_6 have been suggested as an interesting potential research direction for kinetically fast MIB cathode materials with higher energy densities [103], although they have not been demonstrated to date.

There have been several main strategies used to improve the performance of CP materials. These are: 1) substitution of S with Se, 2) reducing the particle size, and 3) incorporating Cu into the host CP. Additional work has been made to improve the synthesis for scale-up, since the original preparation methods suffer from drawbacks including high temperatures and vacuum conditions [160].

First, reducing the particle size has been shown to be effective [132]. Since no surface films are known to form on CP in the DCC electrolyte, this approach increases the active surface area without increasing parasitic side reactions depleting the electrolyte or Coulombic efficiency. This is in stark contrast with LIB materials, where side reactions associated with SEI formation are undesirable but necessary to protect the electrode materials. Milling decreases the particle size and improves capacity. However, this effect only held for milling under inert atmospheres and for short durations, as oxidation in air and amorphization hurt the electrochemical performance. Another route to nanoscale CP particles simply involved changing the synthetic procedure. A reduced temperature route (from 1250 to 900°C) yielded particles approximately five times smaller than the original method, and increased the capacity by ~5% (Figs 9c and d) [143]. CP nanofibers with diameters in the 100–300 nm range have also been synthesized from a sol-gel technique, although their electrochemical performance has not be reported [146]. Ryu *et al.* [148] also found that controlling the ratio of KCl salt to precursor material in a molten salt synthetic reaction can be used to control the size and electrochemical properties of the product CP. Median diameters of 0.24, 0.57 and 0.75 μm were obtained for 4:1, 6:1 and 2:1 salt-to-precursor ratios (whether this is a weight or molar ratio was not specified). The best capacities and rate performance was obtained in the case of the 6:1 synthesis. The optimum average size was apparently 0.57 μm, with the smaller particles allegedly leading to side reactions that hurt performance. This contrasts with previous reports where no such side reactions are observed [105,132]. However, a different albeit closely related electrolyte was used in this study: $(PhMgCl)_2$-$AlCl_3$/THF. Recently, Woo *et al.* [153] found that chemical intercalation of copper via a low temperature (80°C) solid-state reaction serves as an effective means of controlling the copper content and size of the CP powder (Fig. 10). The chemically intercalated material showed a narrower voltage hysteresis and better capacity, presumably related to the high active surface area of the material.

Replacing S with Se is an effective way to avoid charge trapping [134]. This was attributed to the greater polarizability of selenium compared to sulfur, although this kinetic improvement comes at the price of lower insertion voltages

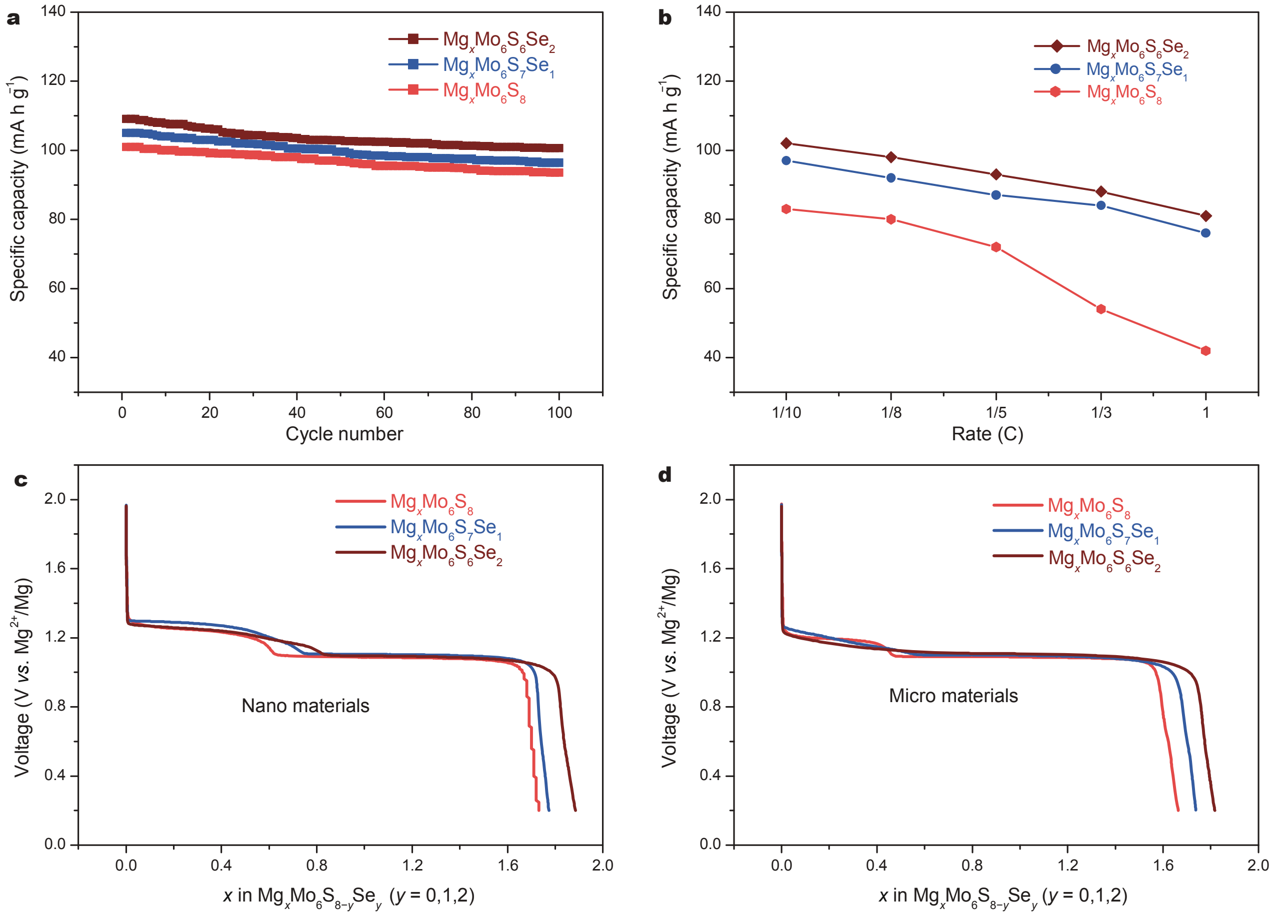

Figure 9 (a) Cyclic stability, (b) capacity retention when operated at 15°C, and voltage profiles of (c) nano- and (d) microscale $Mg_xMo_6S_{8-y}Se_y$ for $y = \{0,1,2\}$ cycled using the DCC electrolyte at various rates. Reprinted with permission from Ref. [143], Copyright 2007, WILEY-VCH Verlag GmbH & Co. KGaA, Weinheim.

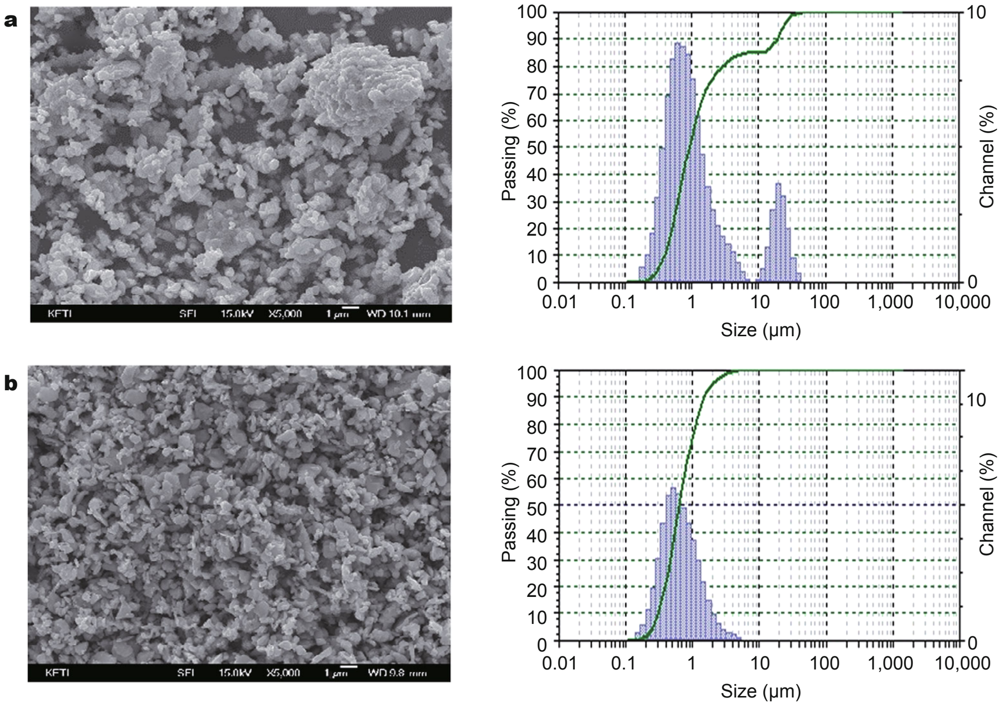

Figure 10 Field emission SEM (FESEM) and particle size analysis results indicate a larger and bimodal size distribution for the case of (a) the leached CuCP *vs*. (b) the chemically intercalated CuCP. Reprinted with permission from Ref. [153], Copyright 2014, Royal Society of Chemistry.

and (theoretical) capacities. Further X-ray and neutron diffraction work also indicated that the geometry of the unit cell is increased, and the relative positions of the inner and outer sites are more favorable (Fig. 11) [137,138]. The combined effect of these two changes greatly enhanced transport kinetics, with the second being particularly crucial for reducing charge trapping. Saha *et al.* [106] have extended this concept to Mo_6Te_8 via first-principles calculations. The electronic structure suggests strong hybridization between the Mo 4d and {S,Se,Te} 3p orbitals and high electronic conductivity over the pertinent range of Mg content ($0 < x < 2$), although the material becomes semiconducting as x tends to 2. As expected, the voltage decreased as the anion was changed from S to Se to Te, reflecting the longer, weaker bonds obtained going down the group.

Partial substitution of Se boosts the kinetics without hurting the capacity or voltage, as evidenced in Figs 9a and b [143,144]. The superior kinetics raises the utilization of the electrode and increases the observed capacity (even though the heavier Se atoms decrease the theoretical value), while simultaneously improving the rate capability at 15°C.

A third approach involves incorporating Cu into the structure of the CP material. As mentioned above, Mo_6S_8 and related compounds are metastable, so they have to be obtained from a parent structure (usually $Cu_xMo_6S_8$) by chemical leaching [131]. Fortuitously, it was discovered that maintaining some level of copper in the material leads to better capacities (~100 mA h g^{-1} *vs.* ~90 mA h g^{-1} for previous CP cathodes) and kinetics by avoiding charge trapping [127,141]. Structural and electrochemical analysis indicated reversible extrusion of Cu^0 upon Mg^{2+} intercalation. Both types of cations occupy the same inner and outer ring sites, with preferential substitution of Mg in the inner sites and Mg/Cu segregation taking place. Upon charging, the reinsertion of Cu forces Mg out of the inner sites, bypassing charge trapping phenomena [142]. In addition to decreasing particle size, Woo *et al.* [153] also found that high capacities could be obtained with over 1 mole of Cu per CP formula unit. Discharge capacities of 112, 105, and 94 mA h g^{-1} were obtained as the copper content in Cu_xCP was increased from $x = 1.3$ to 1.5 to 1.7, respectively. Optimized Mg-Cu repulsion effects were cited as the reason for the high performance of $Cu_{1.3}Mo_6S_8$, whereas higher copper concentrations block diffusion. The same group recently contributed to understanding the mechanism of Cu insertion and extraction [155]. They used a Cu nanoparticle/graphene composite as an additive to study the formation of Cu_xCP and its interaction with Mg^{2+}. First, they noted the spontaneous intercalation of Cu

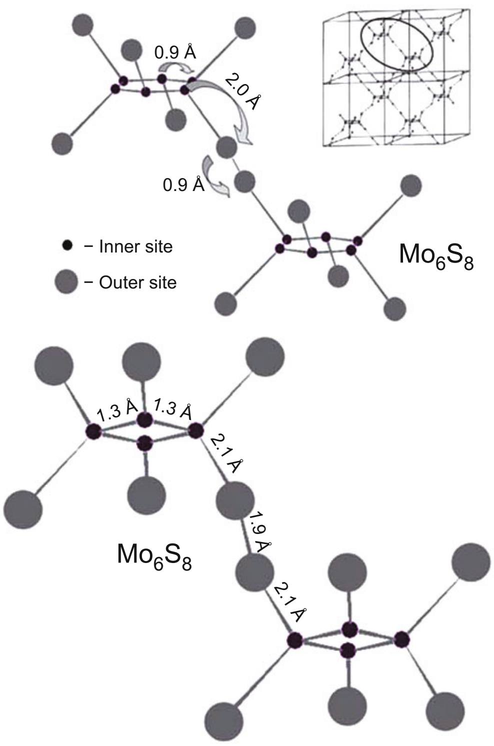

Figure 11 The relative positions of inner and outer Mg insertion sites in the pure sulfide and selenide CP compounds. Reproduced with permission from Ref. [105]. Copyright 2013, Royal Society of Chemistry.

into the host material. Structural analysis with XRD, XPS, and TEM further suggested that Mg^{2+} insertion ejects Cu^+ from the CP, at which point the copper is reduced to Cu^0 at the surface. Upon charging, the process reverses as metallic copper is oxidized and inserted while Mg^{2+} is removed (Fig. 12).

Another novel approach to increasing the energy density of MIBs has recently been proposed by Ichitsubo *et al.* [149]. They note the discrepancy between the potentials for Cu extraction from Cu_xCP (~1.2 V) and Cu metal dissolution (~1.7 V) in Mg-compatible electrolytes. That is, the chemical potential of copper in the CP is apparently greater than that for the metal, in disagreement with thermodynamics. They resolve the apparent contradiction by invoking effects pertaining to the electrolyte. When small solvents such as ethylene carbonate (EC) and dimethyl carbonate (DMC) infiltrate the host and occupy the most stable Mg sites, Cu^+ and Mg^{2+} are forced into less stable sites that artificially lower the (de)intercalation potential. Conversely, larger solvents such as glymes and ionic liquids are too bulky to enter into the host, and a relaxation effect allows cations to find the most stable sites, if given time to reach equilibrium. They propose that this feature can conceivably be used to raise the operating voltage of CP cathodes into the 2–3 V range.

In addition to those methods described above, several

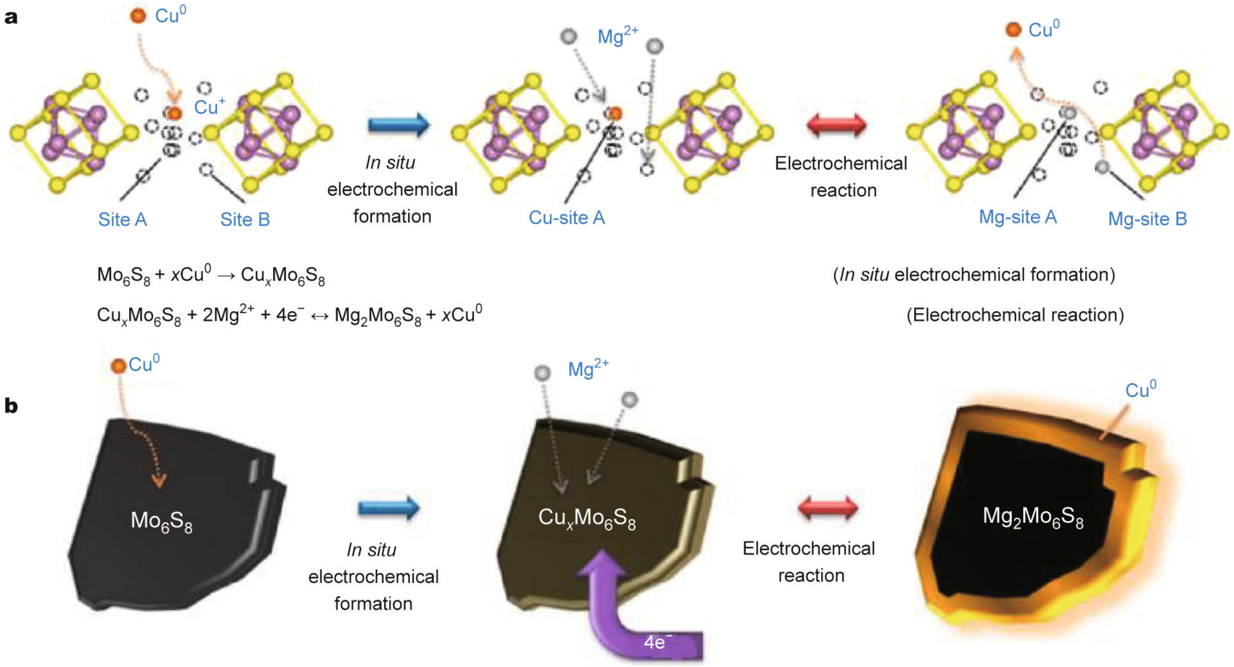

Figure 12 Schematics for incorporation of Cu and subsequent displacement by Mg at (a) the level of the unit cell and (b) the level of the microstructure of Mo_6S_8. Reprinted with permission from Ref. [155], Copyright 2015, American Chemical Society.

studies have focused specifically on the synthesis of CP materials. Emphasis has been placed on reducing the temperature and duration of the traditional high-temperature solid state procedure, as well as reducing the need for high vacuum or potentially explosive mixtures [136]. A direct synthesis of Mg_xCP would be advantageous, but does not appear to be feasible because of the formation of passivating MgO surface films that inhibit performance [135]. The first reported molten salt method to $Cu_2Mo_6S_8$ lowered the required temperature from 1100–1200°C to 850°C and reduced the reaction time from 200 to 60 h because of faster kinetics in the liquid medium [136]. Later, a high-yield (96%) thermal explosion synthesis was reported to run to completion in as little as 10 min [147]. In both cases, the new product and the solid-state products showed approximately identical electrochemical performance. A wet chemistry route to $Cu_2Mo_6S_8$ was proposed by Saha *et al.* [150]. The precipitate obtained from the reaction between $(NH_4)_2MoS_4$ with $CuCl_2$ in DMF was later annealed at 1000°C, and the resulting material was composed of micron-sized particles. The reaction itself takes only 5 h, although annealing and leaching steps add at least 12 h to the process. The CP material obtained from this route had relatively low capacity at a C/6 rate (~76 mA h g^{-1}), but showed only 13% capacity loss when the rate was increased by almost a factor of 10 (~66 mA h g^{-1} at 1.5 C), with correspondingly high Coulombic efficiency (~99.3%).

(ii) Molybdenum disulfide. MoS_2 is a two-dimensional solid with layers held together by vdW forces. This makes it quite similar to graphene, and it shares many of the same electronic and structural properties. As an MIB cathode material, its theoretical capacity is ~223.2 mA h g^{-1} (for magnesiation up to $Mg_4Mo_6S_{12}$) [161].

Initial studies on MoS_2 by Novák *et al.* [99] showed irreversible electrochemical insertion of Mg^{2+} using an ionic liquid electrolyte at 80°C. The first use of MoS_2 as a reversible Mg-ion host was presented by Li and Li [162]. Nanostructured MoS_2 with a range of morphologies were prepared via a relatively low temperature (~180°C) hydrothermal route. The molybdenum source was $NaMoO_4$ and a variety of sulfurization reagents were used, including Na_2S, $MeCSNH_2$, CSN_2H_4, KSCN and CS_2. Solution processing was followed by calcination under Ar at 700°C. Electrochemical cycling was performed in a variant of the DCC electrolyte, and while many reversible cycles were reported, the capacity and Coulombic efficiency were very low (<25 mA h g^{-1}, <40% CE).

More recently, Liang *et al.* [161] prepared graphene-like MoS_2 (G-MoS_2) from a solvothermal reaction between MoO_3 and thioacetamide (CH_3CSNH_2) in pyridine. XRD, TEM, and Raman spectra results indicated the exfoliated material was composed of four layers of MoS_2 on average, and slightly larger interplanar spacing compared to the bulk material (B-MoS_2). Nanoscale Mg (N-Mg) particles under 5 nm in diameter were prepared by reducing $MgCl_2$ in an ionic liquid to investigate the effect of the anode material on cell performance compared to bulk Mg (B-Mg). Electrochemical tests demonstrated the synergetic effect of the nanoscale anode and the exfoliated MoS_2 cathode, as compared to the bulk materials (Fig. 13). The cell operated at ~1.8 V and achieved 170 mA h g^{-1} in a Mg-compatible electrolyte ($Mg(AlCl_3Bu)_2$/THF), with 95% capacity retention after 50 cycles. The improvements over the bulk were attributed to less charge trapping and thinner surface films at the cathode and anode, respectively.

Liu *et al.* [163,164] published similar studies on MoS_2/carbon composites. Both used a combination of hydrother-

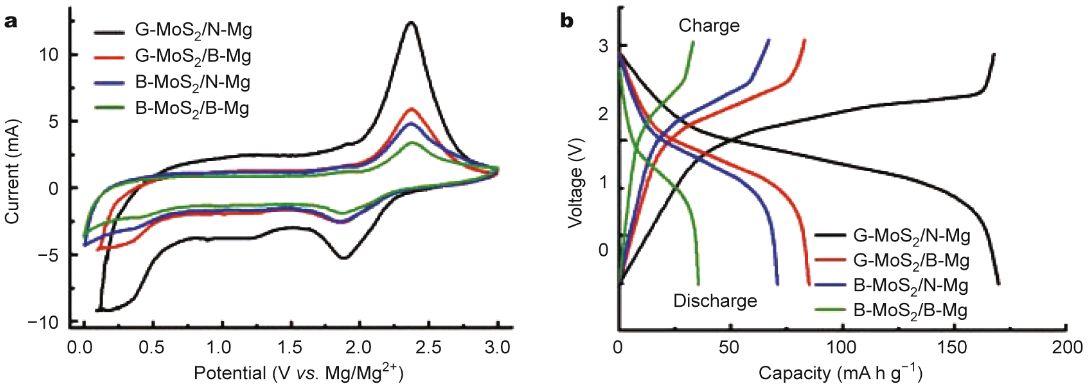

Figure 13 (a) Cyclic voltammograms for all four permutations of bulk (B) and graphene-like (G) MoS_2 at the cathode and bulk and nanosized (N) magnesium at the anode. The anode served as both the counter and reference electrode and the scan rate was 1 mV s^{-1}. (b) Voltage profiles for coin cells measured at a current density of 20 mA g^{-1}. Reprinted from Ref. [161], Copyright 2011, WILEY-VCH Verlag GmbH & Co. KGaA, Weinheim.

mal and heat treatments to optimize the composition of the composite cathodes. The optimized composite had a carbon content of ~46 wt.% microspheres and its morphology was identified as microspheres of carbon interspersed between MoS_2 layers [163]. The initial capacity approached the theoretical limit (213 *vs.* 223.2 mA h g^{-1}), and stayed above ~80 m Ah g^{-1} for 50 cycles. Rapid capacity deterioration during the first eight cycles was attributed to passivation of the AZ31 Mg alloy (3% Al, 1% Zn, 96% Mg by weight) anode. Similar results were obtained when glucose was replaced with reduced graphene oxide as the carbon source [164]. The carbon served both to enhance conductivity and exfoliate the MoS_2 layers, allowing more access to insertion sites.

Several computational studies have focused on MoS_2 in various morphologies to help guide future experiments. Yang *et al.* [165] performed DFT calculations to study the properties of zigzag MoS_2 as a cathode material. This particular conformation was selected on the basis of its high conductivity. They found preferential adsorption above the Mo atoms (denoted as T sites) at the edge of ribbon, and that Mg interacts primarily by forming ionic bonds with MoS_2. The diffusion path along the nanoribbon takes the atom from one T site to the next nearest one by first passing through the central site (H) above a Mo_3S_3 hexagon (Fig. 14). The energy barrier for this process is only 0.48 eV, which is a big improvement over 2.61 eV in the bulk, and corresponds to a million-fold increase in the diffusion coefficient (assuming Arrhenius type diffusion).

Liang *et al.* [166] formally introduced the tuning of interlayer distance as an effective way to decrease the diffusion barrier, using MoS_2 as a model system. Downsizing materials and screening the divalent Mg^{2+} charge with water have been used often in many reports, but come with problems associated with low material density and Mg anode compatibility, respectively. Tuning the interlayer spacing has proven effective in the context of, for example, $Li_xV_2O_5$ xerogels [47] and MoS_2 anodes for NIBs [167], and may serve as a tool for rational design in MIB materials. DFT shows how the diffusion barrier experiences a significant decrease from 1.12 to 0.22 eV by increasing the interlayer spacing from 0.65 to 0.9 nm (Fig. 15). The latter value is even smaller than predicted for single-layer MoS_2 by Yang *et al.* [165], which might be caused by differences in methodology and conformation.

In this range, the material goes from bulk diffusion behavior to a closer approximation of the single-layer behavior. To test their model experimentally, they delaminated and restacked MoS_2 layers with varying amounts of polyethylene oxide (PEO), which varied the spacing from 0.615 nm in pristine MoS_2 to 1.45 nm for an equimolar amount of PEO and MoS_2. While the experimental results were not as positive as the DFT model predicted, increasing the spacing did improve the conductivity and rate capablity. The cyclic stability of the largest spacing was also good, with 94% of 75 mA h g^{-1} retained after 30 cycles. The relatively low capacity was in part due to the multilayer strucuture, since the theoretical capacity of 223.2 mA h g^{-1} only pertains to single layers that can adsorb two layers of Mg atoms per layer of MoS_2. Nevertheless, the result demonstrates how tuning interplanar spacing may be an effective strategy to improve Mg^{2+} intercalation in host materials.

Pereira and Miranda investigated Mg adsorption and diffusion into MoS_2 and WS_2 using an approximation of nanotubes compatible with DFT [168]. Their results indicate that insertion at the outside surface is more favorable than the inside of the nanotubes, and the voltage and binding energy increase as the size of the nanotubes is reduced (although high concentrations of Mg^{2+} will become increasingly unstable). The preferred diffusion path is identical to the path described by Yang. The activation energy for diffusion apparently decreases from 0.778 eV for bulk MoS_2, and as low as 0.051 eV for 10 Å nanotubes,

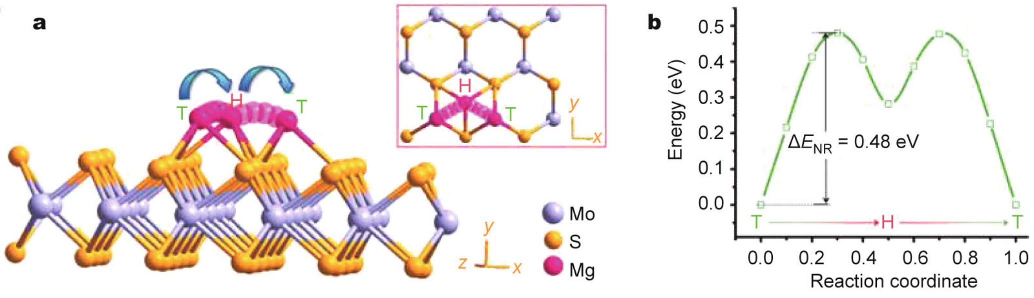

Figure 14 (a) Mg diffusion path on the surface of a MoS_2 nanoribbon view from the side and from above (inset). (b) Energy barrier to diffusion along the T-H-T pathway, with activation barrier ΔE_{NR} indicated. Reprinted from Ref. [165]. Copyright 2012, American Chemical Society.

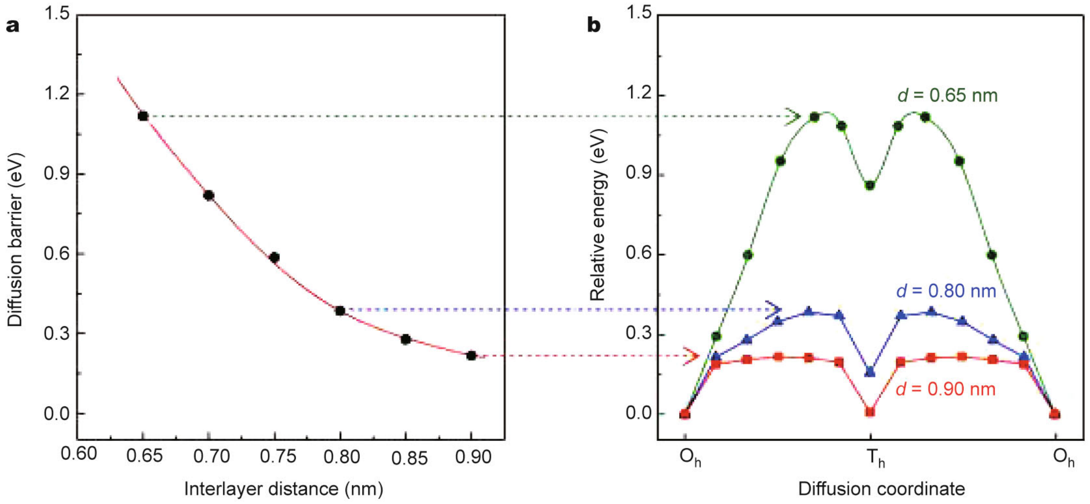

Figure 15 (a) The predicted diffusion barrier for Mg in MoS_2 is inversely related to the interlayer distance. (b) The potential energy diagram for migration from one octahedral site to the next shows great reductions in the range 0.65 nm < d < 0.90 nm. Reprinted from Ref. [166], Copyright 2015, American Chemical Society.

while larger nanotubes approach the behavior of single-layer MoS_2 (~0.080 eV barrier). While the particular values between different studies are not quantitatively comparable, these results suggest the pathways to increasing ionic mobility, and may lead to MoS_2 or other nanostructured materials with high rate capabilities.

(iii) Titanium dichalcogenides. Titanium disulfide has been used as a LIB host material with good results, but its performance as an MIB cathode has been less impressive so far. Bruce and Gregory *et al.* [97,169,170] both screened TiS_2 as a Mg host, with inconsistent results. Electrochemical results were also lackluster in the case of layered and cubic TiS_2 in $Mg(ClO_4)_2$/THF [116] and DCC electrolytes [160], respectively.

The most positive experimental results regarding TiS_2 were reported by Tao *et al.* [121]. They prepared TiS_2 nanotubes through a low temperature gas-phase reaction. This material inserted ~0.49 Mg per TiS_2 molecule, for an initial capacity of 236 mA h g^{-1}. Further, it maintained a capacity of 180 m Ah g^{-1} after 80 cycles and operated at an average voltage of ~1.25 V. The high surface area of the nanotubes was credited for the good performance, but the exact reaction mechanism was not identified. Exfoliating bulk TiS_2 has been suggested as a possible method to superior performance, analogous to MoS_2 [27,161].

This intuition is supported by a theoretical study by Emly and Van der Ven [171], who looked at layered and spinel TiS_2 as a model system and compared some of the properties of Li_xTiS_2 and Mg_xTiS_2. In the case of the layered polymorph, the diffusion barrier is reduced from 1.16 to 0.55 eV as the c-axis is augmented by 10% (Fig. 16), and qualitatively similar results for the spinel. As with Li, the diffusion path for Mg in TiS_2 starts at one octahedral site, passes through a local energy minimum in a tetrahedral site, and arrives at an adjacent octahedral site. Additionally, Mg^{2+}/vacancy ordering is shown to correspond with voltage drops in the predicted voltage profile of layered Mg_xTiS_2, while the spinel voltage slopes with no apparent plateaus, suggesting solid solution behavior. The ordering effects are a consequence of the strong interactions between the host and Mg^{2+}. In agreement with Liang *et al.* [166], they point to tuning the interlayer spacing as a useful tool. However, they also note that the ease with which transition metals change valence states plays an important role in determining the diffusion barrier for Mg, which may preclude TiS_2

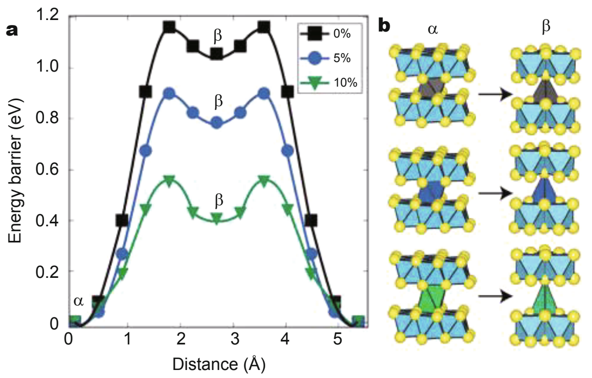

Figure 16 Effect of expanding the c-axis on the diffusion barrier for a dilute concentration of Mg in layered TiS_2. The energy barrier is shown in (a) and a schematic of the change in the c parameter is shown in (b). Reprinted from Ref. [171], Copyright 2015, American Chemical Society.

as a viable MIB cathode material.

Gu *et al.* [172] recently reported on $TiSe_2$ for the first time as an MIB cathode material. Noting the beneficial effects of electron delocalization in CP [100], the study focused on hybridization of the energetically similar Ti 3d and Se 4p atomic orbitals (Fig. 17). Density of states calculations provided further evidence for d-p hybridization, which is proposed as a driving force for the material's good electrochemical performance. When tested in a coin cell configuration with DCC electrolyte and a Mg metal anode at a rate of 5 mA g^{-1}, an average capacity of 108 mA h g^{-1} was observed over the course 50 cycles, which is ~83% of the maximum capacity. Further, ~50% of the capacity was retained after a tenfold increase in the current density, from 5 to 50 mA g^{-1}. While the energy density is modest (the discharge voltage is <1 V), this significance here is that the electronic structure of various hosts has been ignored relative to the crystal structure, but may be invoked to explain the good performance of materials with strongly hybridized metal-anion molecular orbitals. Such materials include TiS_2 [121], WSe_2 [173], and MoS_2 [161] in the case of MIBs, and CoO_2 [16] and MnO_2 [174] in the case of LIBs.

Layered titanium chalcogenides may not prove to be as successful as magnesium hosts, but they have served as useful model systems. These recent studies add valuable insight into the rational design of MIB cathode materials.

(iv) Other TMCs. Besides those chalcogenides already mentioned, a wide swath of other TMCs have been screened, with modest-to-poor results. Chemical intercalation of VS_2 [97] demonstrated moderate capacity and voltage (1.71 V, 154 mA h g^{-1}). ZrS_2 [97] showed a higher energy density (2.60 V, 228 mA h g^{-1}), but displayed poor electrochemical behavior in $Mg(ClO_4)_2$/acetonitrile (AN) [116]. In addition to TiS_2 referenced above, Amir *et al.* [160] screened CuS, $CuFeS_2$, $CuFe_2S_3$, Cu_9S_8, Cu_2S, NiS, TiSSe, and NiS_xSe_y using the DCC electrolyte. All these compounds demonstrated some electrochemical activity, but rapid capacity fading supports the conclusion that these materials are unlikely to be robust MIB cathode materials.

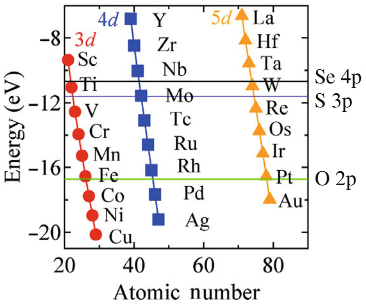

Figure 17 Energy levels for the partially filled *nd* orbitals of the transition metals ($n = 3, 4, 5$) plotted with horizontal lines to show the energy of the O 2p (green), S 3p (purple), and Se 4p (black) orbitals. Reprinted from Ref. [172], Copyright 2015, Nature Publishing Group.

Novák *et al.* [99] screened NbS_2, which lead to minimal Mg insertion at 80°C in an ionic liquid electrolyte. Yuan and Günter [175] prepared NbS_3 from the respective elemental powders in a high-pressure synthesis. The open circuit voltage (V_{oc}) of Mg/solid electrolyte/NbS_3 cells was ~1.82 V, and two plateaus at 1.5 and 1.2 V were observed during the first discharge. The highest degree of intercalation was 0.74 Mg per host molecule, equivalent to ~210 mA h g^{-1}, but the capacity quickly deteriorated in just a few cycles.

Several more recent developments have focused on cobalt, tungsten and vanadium dichalcogenides, with more promising results. He *et al.* [176] studied CoS for the first time as an MIB battery material. CoS was prepared from a solvothermal process at 180°C. The flower-like morphology was the result of thin nanoplates assembling into micron-sized spheres (Fig. 18). They propose

$$CoS + Mg^{2+} + 2e^{-} \rightarrow Co + MgS \tag{4}$$

as the pertinent reaction scheme, which they support with evidence from XRD and inductively coupled plasma mass spectrometry (ICP-MS) analysis. An initial discharge capacity of 123.5 m Ah g^{-1} was observed at a current density

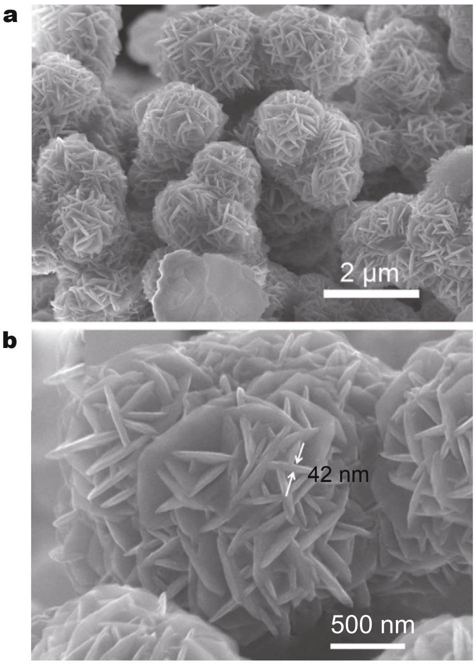

Figure 18 SEM images of the flower-like morphology of the pristine CoS material. Reprinted from Ref. [176], Copyright 2015, Elsevier.

of 50 mA g^{-1}, and retained a capacity of over 100 mA h g^{-1} after 65 cycles. Formation of an SEI layer reduced the energy efficiency for the first several cycles, but was nearly 100% afterward. The material also demonstrated good rate capability. After 30 cycles, no apparent fading was found at a current density of 150 mA g^{-1}. The material performance is also sensitive to the morphology, as doubling the Co precursor concentration led the formation of solid microspheres that showed a lower capacity and faster fading.

Novák and coworkers [99] electrochemically intercalated $Mg_x WS_2$ up to $x = 0.28$, but no further progress on tungsten compounds was reported until recently. Liu *et al.* [173] grew WSe_2 nanowires directly on W foil by chemical vapor deposition (CVD) technique. The material showed a high capacity of ~200 mA h g^{-1} with negligible fading over 160 cycles at 50 mA h g^{-1}. This high capacity and efficiency is even retained at high rates (Figs 19a-c). The reported performance is attributed to several features of the nanowire array, including very high active surface area and good mechanical and electrical properties. They also present DFT results that support the electrochemical stability and high conductivity of magnesiated WSe_2.

Lastly, Gu *et al.* [172] obtained similar results for VSe_2 as compared to $TiSe_2$. With a major discharge plateau slightly below 1 V and a capacity of ~110 mA h g^{-1}, over 60 cycles were demonstrated with no apparent capacity fading. Again, this was attributed in part to hybridization between the V 3d and Se 4p atomic orbitals, which allows for electron delocalization that in turn boosts kinetic performance.

Pereira and Miranda [168] also examined the properties of WS_2 nanotubes, and concluded that, similarly to MoS_2, Mg insertion is not stable above certain Mg concentrations. As such, the maximum practical capacity may be limited. However, they found that WS_2 nanorods exhibit very high Mg mobility, even compared to Li. The Mg diffusion barrier for a 10 Å WS_2 nanorod was 23 meV, compared to ~35 meV for single layer WS_2 and 864 meV for Mg diffusion in bulk WS_2. For Li, the barrier was 198 meV on 10 Å nanorods.

In general, the various sulfides and selenides have demonstrated or are projected to demonstrate good ionic mobility thanks to anion polarizability. However, increased diffusivity generally comes at the cost of low voltages and theoretical capacities relative to the analogous oxides. Chevrel phases offer the best performance to date, but have relatively low energy densities and involved syntheses,

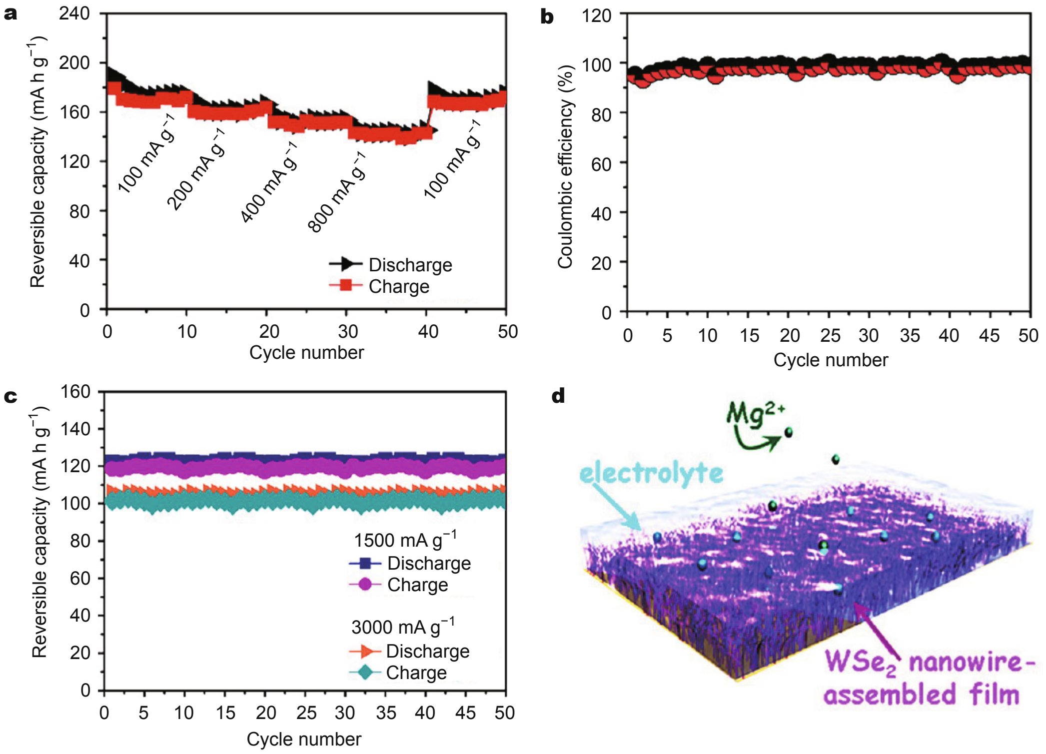

Figure 19 (a) Rate performance and (b) corresponding efficiency of the WSe_2 nanowire cathode. (c) Cyclic stability at very high rates of 1.5 and 3.0 A g^{-1}. (d) Schematic of Mg^{2+} intercalation into the nanowire array. Reprinted from Ref. [173], Copyright 2013, American Chemical Society.

while most other TMCs have had problems with extended cyclability. Further work is required to identify the reaction mechanisms at the atomic level and produce materials that simultaneously have good energy density, long cycle life, and scalable syntheses.

Transition metal oxides

(i) Vanadium oxides. After the family of CP compounds, the various vanadium oxides have been the second most popular subject of MIB cathode investigations in terms of publications [97,99,115,116,169,177–207]. As a cathode material, it has advantages of reasonably low cost and high capacity stemming from its available valence states. The theoretical reduction from V^{5+} to V^{3+} corresponds to the formation of $Mg_2V_2O_5$, whose capacity is 589 mA h g^{-1} with respect to V_2O_5. However, slow Mg^{2+} transport and poor capacity retention are key problems that have not yet been solved.

Vanadium pentoxide is a layered compound composed of square pyramidal VO_5 clusters, with weak vdW interactions between V and a 6th oxygen atom on adjacent layers. Initial screening by Gregory *et al.* [97] found V_2O_5 had a fairly high V_{oc} of 2.66 V and a capacity of 196 mA h g^{-1} via chemical intercalation. As with most oxide materials, insertion of Mg^{2+} into V_2O_5 or related variants has proven difficult, owing to slow diffusion and de-solvation arising from the electrostatic effects of the divalent ion [182,208]. Several early papers indicate modest results with respect to either electrochemical or chemical intercalation [169,177–179]. V_2O_5 has also been used as a cathode in cells with polymer gel electrolytes, but longevity has proven to be a big issue, with no more than ~10 cycles reported [184,187,190,197].

Methods to improve reversible electrochemical intercalation have focused on screening the divalent charge or controlling the structure on the nanoscale. These approaches are used in tandem in the case of vanadium gels. Further, doping has been used to improve the electrochemical properties of V_2O_5 for Li insertion, and should be a useful technique for improving MIB materials as well.

Increasing the active surface area is a familiar method used to improve battery material performance. Amatucci *et al.* [115] prepared a nanocrystalline V_2O_5 powder with particle sizes in the range of 20–50 nm using a chemical vapor condensation technique. The powder had a large surface area (~90 m^2 g^{-1}) and a high reversible capacity of 180 mA h g^{-1}, but showed a large voltage hysteresis indicative of slow kinetics (Fig. 20). Jiao *et al.* [193] prepared VO_x nanotubes via a sol-gel/hydrothermal route. The nanotubes were a few microns in length and less than 100 nm wide. The capacity and stability were not high as the initial capacity was ~80 mA h g^{-1} with rapid fading, but a follow-up study improved the capacity and conductivity of the nanotubes by doping with Cu [194]. The capacity increased to 120 mA h g^{-1} and still faded fast, but the result indicates that transition metal dopants can be expected to bolster electrochemical performance.

Another nanotube synthesis used a microwave-assisted hydrothermal process [202]. By controlling the amount of the reducing agent, the average valence state of vanadium metal centers could be manipulated, as observed from XPS measurements. While the average valence state did not strongly affect the initial capacity (in fact, the cathode prepared with lower amine content, denoted as LT-VO_x, showed slightly higher capacity and Coulombic efficiency compared to the one with a high amine concentration, denoted as HT-VO_x), the presence of V^{3+} reduced the impedance of the nanotubes, which in turn improved the cyclic stability (Fig. 21). The LT-VO_x faded to about one third of its initial capacity after 20 cycles, while the HT-VO_x cathode showed ~71% capacity retention. This improvement is attributed to mitigated repulsion between Mg^{2+} and V^{3+} ions, relative to vanadium in higher oxidation states, which enhances transport and structural stability of the nanotubes.

Gershinsky *et al.* [201] used thin film electrodes to study the mechanism of Mg insertion into V_2O_5. The film was vacuum deposited on Pt foil ~200 nm thick. A differential capacity plot revealed four distinct steps in both the insertion and extraction steps (Fig. 22), which suggests that the processes involved are rather complicated. Stable cycling above 150 mA h g^{-1} was observed for 35 cycles,

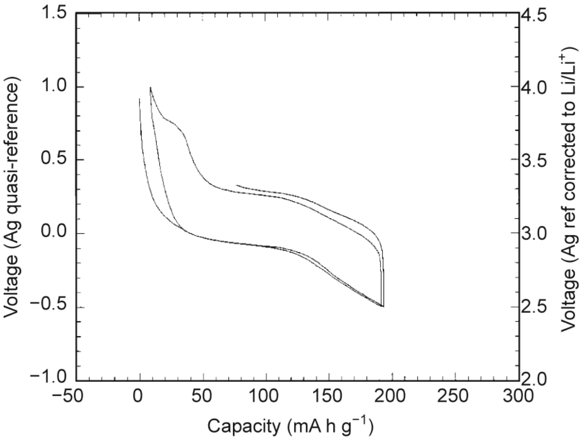

Figure 20 Reversible electrochemical insertion of Mg^{2+} into nanocrystalline V_2O_5 proceeds with high voltage polarization. The electrolyte was 0.5 mol L^{-1} $Mg(ClO_4)_2$ in propylene carbonate (PC), the cell used an activated carbon counter electrode and a silver quasi-reference electrode, and the current density was 7.6 mA g^{-1}. Reproduced from Ref. [115], Copyright 2001, the Electrochemical Society.

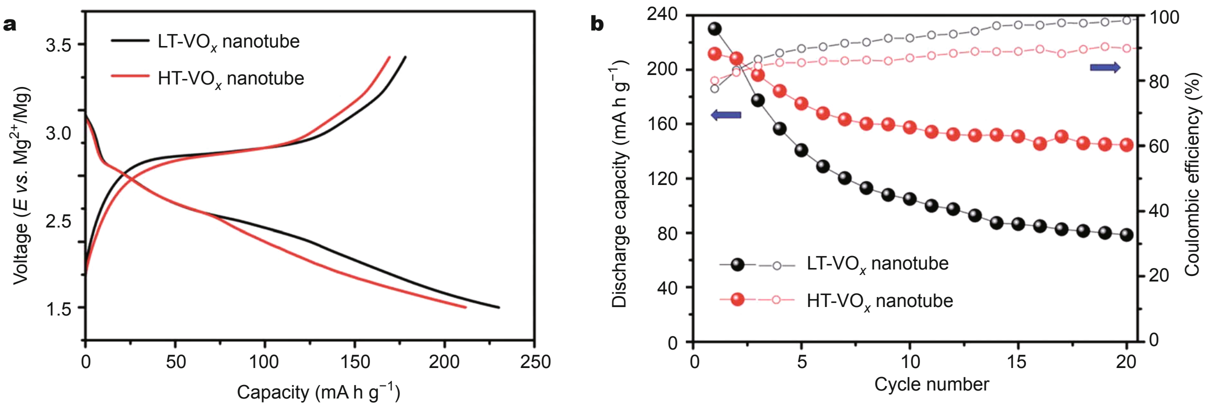

Figure 21 (a) Initial charge-discharge voltage profile (0.2 C rate) and (b) cyclic stability and Coulombic efficiency for the HT-VO_x and LT-VO_x nanotubes. Reprinted from Ref. [202]. Copyright 2014, Royal Society of Chemistry.

with very high Coulombic efficiency. The low capacity may be a consequence of the relatively narrow cycling window (2.2–3.0 V), and corresponds to ~0.5 Mg inserted per host molecule. The rigorous electrochemical analysis of thin films is a useful platform for further characterization of Mg insertion mechanisms, which are by and large not well resolved so far.

The effect of wet electrolytes on electrochemical performance was first observed by Novák and Desilvestro [116]. While single crystal V_2O_5 did not function at all, a maximum initial capacity of ~170 m Ah g^{-1} was obtained when 1 mol L^{-1} H_2O was added to the 1 mol L^{-1} $Mg(ClO_4)_2$/AN electrolyte, although rapid fading still occurred within 20 cycles. This effect was repeated in a similar study [188] that used PC as the solvent instead of AN, where a maximum capacity of ~158 mA h g^{-1} was obtained when the water concentration was 1.8 mol L^{-1} in the electrolyte, but faded even faster.

Since wet electrolytes are reactive toward Mg metal, Novák *et al.* [180,181] attempted to use hydrated vanadium oxides of the form $MV_3O_8{\cdot}nH_2O$, where M was an alkali or alkali earth metal, to gain the advantages of charge screening without passivating the Mg anode. Heating the vanadium bronze at 100°C removed some of the water, leaving ~3 H_2O molecules per formula unit. The $MgV_3O_8{\cdot}3H_2O$ showed ~150 mA h g^{-1} at first, and stayed above 80 mA h g^{-1} for 60 cycles in an ionic liquid electrolyte. However, while they found that the presence of some water was crucial to cycling, FTIR spectroscopy indicated that some of the lattice water is removed during the process.

Vanadium oxide aerogels are prepared by supercritically drying a V_2O_5 hydrogel using liquid CO_2. The high surface area and structural water are considered to be advantageous to its performance as an MIB cathode. They have been investigated by Tang *et al.* [189] and Le *et al.* [183] as Mg^{2+} hosts. While chemical intercalation with $MgBu_2$ produced $Mg_2V_2O_5$ [208], only ~0.6 mol could be reversibly

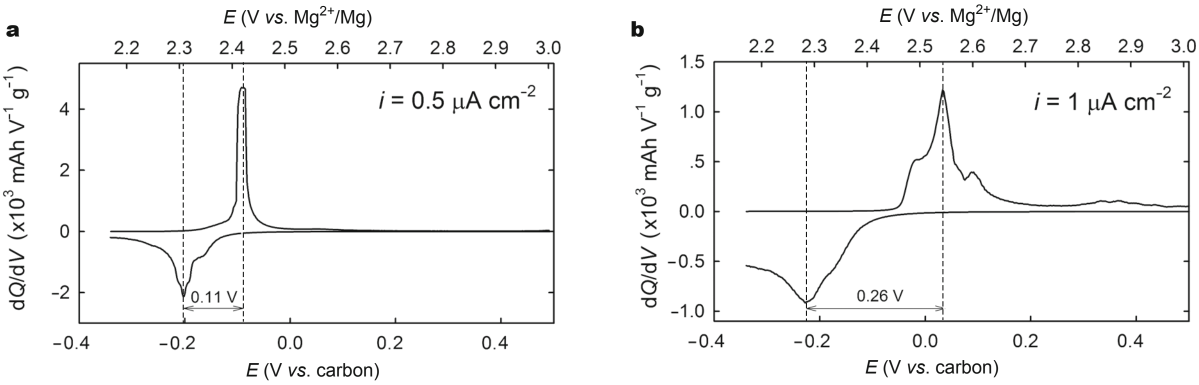

Figure 22 Differential capacity plots obtained for V_2O_5 thin film electrodes with 0.1 mol L^{-1} $Mg(TFSI)_2$/AN as the electrolyte and activated carbon cloth as the counter and reference electrodes at current densities of (a) 0.5 and (b) 1 μA cm^{-2}. Reprinted from Ref. [201], Copyright 2013, American Chemical Society. TFSI stands for bis(trifluoromethane) sulfonimide.

inserted in either material. It has been suggested [189] (but not definitively demonstrated [103]) that a pseudocapacitive surface mechanism is responsible for charge storage in these high surface area materials.

Vanadium oxide xerogels have been more thoroughly studied [185,191,196,204]. As with aerogels, xerogels benefit from high surface areas and charge screening by lattice water. Further, these materials are synthesized through sol-gel processing techniques, which are relatively easy to scale up.

Stojković *et al.* [196] studied a xerogel/carbon composite in an aqueous solution saturated with $Mg(NO_3)_2$. A capacity of ~107 mA h g^{-1} was obtained for the composite, compared to less than 50 mA h g^{-1} available in the case of just the xerogel or microcrystalline V_2O_5 by itself.

Imamura *et al.* [185,186] prepared a xerogel/carbon composite that intercalated 1.84 mol Mg^{2+} per unit of V_2O_5, for a capacity of ~540 mA h g^{-1}. CV showed two charge/discharge peaks for both Li^+ and Mg^{2+} insertion, indicating the presence of two distinct and presumably identical insertion sites for both processes. The cell cycled at capacities in excess of 270 mA h g^{-1} after 35 cycles. However, the current densities may have been reported as a factor of 1000 too large (i.e. 1–20 A g^{-1} compared to 1–20 mA g^{-1} [103]).

Lee *et al.* [204] prepared a xerogel with the formula $Mg_{0.1}V_2O_5{\cdot}1.8\ H_2O$ using an ion exchange resin to control the magnesium content. They found better kinetics using AN than carbonate solvents (Fig. 23), which agrees with a computational study on the desolvation of Mg^{2+} in different electrolytes [209]. Cycling at a C/10 rate with 0.5 mol L^{-1} $Mg(ClO_4)_2$/AN as the electrolyte resulted in a high capacity of ~300 mA h g^{-1}, but stability beyond seven cycles was not reported.

Inamoto *et al.* [200] coated the surface of V_2O_5 with sulfur and another metal oxide to inhibit dissolution of sulfur into the electrolyte. The highest capacity was 420 mA h g^{-1} when MnO_2 was used as the additive in the microwave-generated plasma synthesis. ICP-MS analysis on this $V_2O_5/S/MnO_2$ composite material suggested a 100:6.8:14.4 molar ratio of V to S to Mn, and indicated utilization of over 90% of the theoretical capacity. As mentioned above, the increased polarizability of S over O allows for easier insertion kinetics, although the long-term cyclability was not discussed. However, the results show that anion doping in metal oxides can be used to increase the host capacity and should be investigated further.

Several recent computational studies have used V_2O_5 as a model system and are worth reviewing here. Wang *et al.* [199] were the first to use DFT calculations to investigate MIBs using V_2O_5 as the host structure. They compared the transport properties of Li and Mg in both bulk and single-layered V_2O_5. They found that binding energy of Mg to V_2O_5 was much larger (more favorable) for the single layered V_2O_5 compared to bulk (4.06 *vs.* 2.20 eV, respectively). Interestingly, Li was found to have a much lower diffusion barrier in single-layered V_2O_5 compared to bulk (0.20 *vs.* 0.39 eV) while the calculated diffusion barrier for Mg was ~1.4 eV in both cases (Fig. 24). The reduction of the energy barrier for Li was attributed to the formation of half as many ionic bonds between Li and nearby O atoms in the single-layered oxide as in the bulk (2 *vs.* 4 bonds). In the case of Mg, the nanostructured material only reduces the number of bonds from four to three, which is apparently not sufficient to significantly affect the activation energy for diffusion.

In another computational study, Carrasco [203] considered the effect of vdW forces on the thermodynamic and kinetic properties of alkali and alkaline-earth metal inser-

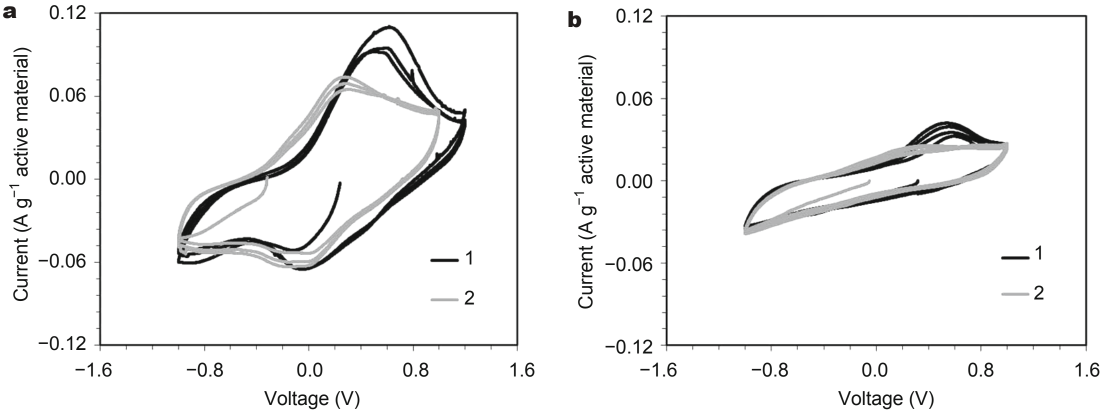

Figure 23 Slow scan CV taken for the $Mg_{0.1}V_2O_5$ electrode at a sweep rate of 0.1 mV s^{-1}. The reference electrode was Ag/Ag^+ and the counter electrode was Pt foil. (a) and (b) refer to AN and EC:DMC solvent, while (1) and (2) refer to $Mg(ClO_4)_2$ and $Mg(TFSI)_2$ salts. Reproduced from Ref. [204], Copyright 2014, The Electrochemical Society.

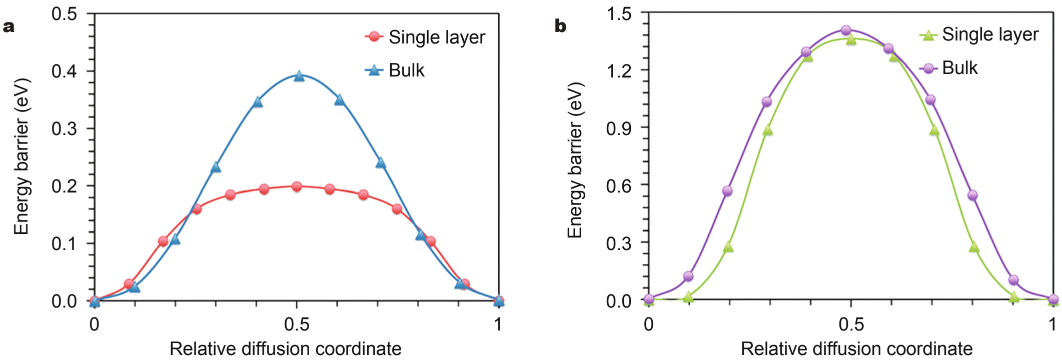

Figure 24 Energy barrier for diffusion for (a) Li and (b) Mg in bulk and single-layer V_2O_5. Reprinted from Ref. [199], Copyright 2013, the PCCP Owner Societies.

tion into bulk V_2O_5. The insertion energy for Mg into V_2O_5 is strongly affected by the position of the V^{4+} centers. The most stable configurations involve placing the two reduced vanadium centers near the inserted Mg ion, and on different bilayers (Fig. 25). This is intuitively reasonable since both the lattice strain caused by the larger V^{4+} centers and electrostatic repulsion between Mg^{2+} and V centers will be minimized in this way. Additionally, diffusion along the *b*-axis is the most favorable, and a 0.97 eV barrier to diffusion was calculated for Mg. Further, quantum mechanical (QM) factors play a more significant role in stabilizing the inserted Mg ion than they do for Na or Li. The model that incorporated vdW forces improved the accuracy of the computed lattice parameters and takes into account QM effects, which had a bigger effect on the insertion voltage for divalent elements than the alkali metals. The vdW model predicted an insertion voltage of 2.70 V, which agrees reasonably well with the V_{oc} of 2.66 V observed by Gregory *et al.* [97].

Zhou *et al.* [205] calculated the V_{oc}, band structure,

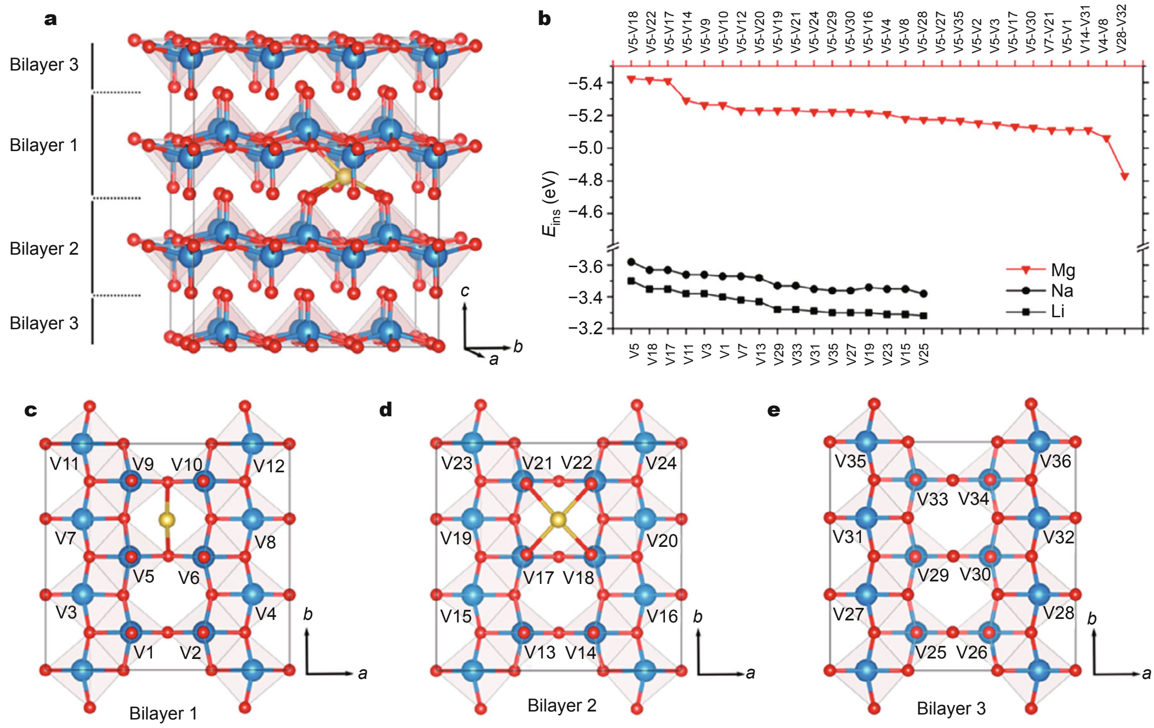

Figure 25 (a) Supercell containing three V_2O_5 bilayers with one ion inserted into the most favorable site. (b) Intercalation energy for Li, Na and Mg as a function of the position of the V^{4+} ions formed upon insertion. (c–e) Bilayers 1–3 with vanadium positions identified. Yellow: alkali (earth) metal; Blue: V; Red: O. Reprinted from Ref. [203], Copyright 2014, American Chemical Society.

diffusivity, and α→δ phase transition energy. Their model calculated an V_{oc} of 3.06 V for magnesium insertion, with an even higher voltage obtained when vdW forces were considered (3.60 V), which is higher than Carrasco's value, but still follows the trend that incorporating vdW forces account for phenomena that act to increase the voltage relative to the Perdew-Burke-Ernzerhof (PBE) functional. This voltage is even higher than that for Li, but has precedent in the literature [183,185]. In these cases, co-intercalation of the solvent has been implicated in raising the voltage [103,32]. While V_2O_5 is known to have conductivity issues, they predict that MgV_2O_5 is highly conductive, with a very small 0.02 eV band gap. In α-V_2O_5, the diffusion barrier is 1.26 eV, whereas for δ-V_2O_5, the barrier becomes 1.38 eV and has a double peak configuration. The two phases are indicated in Fig. 26. They find that there is no barrier to this transformation, and it takes place as magnesium content increases. Since this transformation appears to further inhibit diffusion, more attention should be paid to trying to repress it.

Lastly, Gautam *et al.* [207] derived the full $Mg_xV_2O_5$ phase diagram for $0 < x < 1$. $Mg_xV_2O_5$ exists as a two-phase equilibrium between α-V_2O_5 and δ-V_2O_5. However, they note that a metastable phase, denoted as ε-V_2O_5, undergoes Mg ordering when V_2O_5 is half magnesiated ($Mg_{0.5}V_2O_5$), and may dominate since δ-V_2O_5 requires structural rearrangement of the crystal lattice. Such metastable transitions have been documented in, for example, $LiFePO_4$ and may be present here as well [210]. Contrary to Zhou, they find that the energy barrier for diffusion is higher in α-V_2O_5 than δ-V_2O_5 (0.975–1.120 eV compared to 0.600–0.760 eV, respectively), and suggest that cycling V_2O_5 exclusively in the delta phase may improve performance.

There are some discrepancies to be addressed between these studies, which future experimental work should try to elucidate. Computational materials science is rapidly becoming a more powerful tool, but still needs to be verified in light of the fact that these studies cannot simultaneously capture the myriad phenomena going on within the cathode materials. Nevertheless, they offer useful insight into different possible methods to test proposed mechanisms and improve V_2O_5 performance in MIBs.

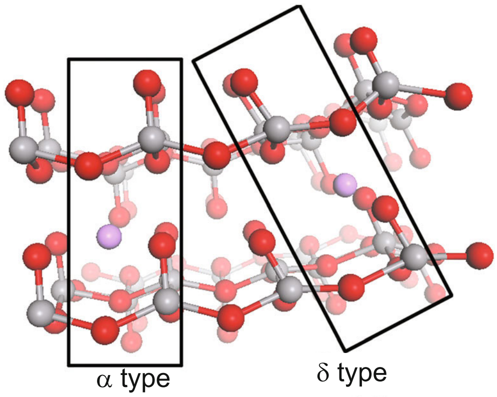

Figure 26 Structure of α- and δ-phase V_2O_5, which corresponds to demagnesiated and magnesiated V_2O_5, respectively. Reprinted from Ref. [205], Copyright 2014, the PCCP Owner Societies.

Many studies on V_2O_5 have shown that it has potential as an MIB cathode material, but limits to stability and kinetics remain challenges that have yet to be solved. Downsizing the active material and a variety of charge screening approaches have improved its performance to a limited extent, and both anion and cation doping appear to have beneficial, albeit not fully understood effects. The growing body of computational work has provided inconsistent results, but also offers avenues to test these results. Another issue for V_2O_5 is that it has been exclusively studied in electrolytes that are not compatible with Mg metal, and it is clear that the electrochemical performance is affected by the choice of electrolyte [204,208]. New high voltage electrolytes have been proposed, and compatibility studies will be needed to show if any of this class of electrolytes can simultaneously support electrochemical reactions at both the cathode and the anode.

(ii) Manganese oxides. Manganese is relatively abundant and environmentally benign metal, making it attractive for MIB applications from an environmental perspective. As a cathode material, MnO_2 has a high capacity (308 mA h g^{-1} for the reduction of Mn^{4+} to Mn^{3+} in $Mg_{0.5}MnO_2$) and voltage (~2.9 V for spinel MnO_2 [123,211]), which has pegged it as one of the most promising positive electrodes for MIBs. The many phases of manganese oxides make it an interesting research subject and potential host for Mg ions. Further, it has recently become the most popular MIB cathode studied, with over half of the reports incorporating MnO_x as a Mg-ion host coming in the past five years [97,106,123,169,211–232].

Initial electrochemical magnesiation of manganese oxides by Gregory *et al.* [97] gave promising results. A V_{oc} of 2.40 V and a capacity as high as 224 mA h g^{-1} were obtained in the case of Mn_2O_3. Electrochemical cycling was later reported in the case of a mixed Mn-Co oxide ($Mn_{2.17}Co_{0.37}O_4$) [212]. However, the capacity fell below 30 mA h g^{-1} within 30 cycles. MnO_2 has also been used to study polymer electrolytes [213,215,216,218,219]. Despite initial capacities as high as 270 mA h g^{-1} [219], long term stability has not been reported thus far, on account of Mg metal passivation on the anode side and kinetic limitations of electrolytic MnO_2

as a Mg-ion host.

Recent studies have generally focused on various MnO_2 polymorphs, which can generally be classified according to their diffusion channels. These include 1D tunnel structures, 2D layered materials, and 3D spinels. Tunnel-structured polymorphs can further be subcategorized by size. Pyrolusite (β-MnO_2), hollandite (α-MnO_2), and todorokite are composed of chains of edge-sharing octahedral that form 1×1, 2×2 and 3×3 square channels, respectively [214].

Pyrolusite was thought to have too narrow a structure to accommodate Mg^{2+}, and has rarely been studied since Bruce *et al.* [169] found minimal Mg storage after chemical intercalation. However, this phase has recently shown performance commensurate with other polymorphs [231], the implications of which are discussed later in this section. Kumagai *et al.* [214] similarly found negligible intercalation into hollandite MnO_2, but obtained 85 mA h g^{-1} for an initial capacity for hydrothermally prepared todorokite when $Mg(ClO_4)_2$/PC was used as the electrolyte.

Nevertheless, hollandite MnO_2 has been the subject of intensive study of late. Zhang *et al.* [221] studied commercial nanoscale α-MnO_2 powder (~20 nm particle size) using Mg-hexamethyldisilane (HMDS) as the electrolyte. An initial capacity of ~280 mA h g^{-1} was obtained, but rapidly faded. EXAFS spectra indicated partial collapse of the tunnel structure, which is brought about by dissolution of Mn into the electrolyte and Jahn-Teller distortion of octahedral containing Mn^{3+} [233].

Rasul *et al.* [220] prepared a composite of α-MnO_2/acetylene black hydrothermally, which showed higher capacity than pristine α-MnO_2 obtained from a sol-gel route (210 and 85 mA h g^{-1}, respectively) [222]. A very high initial capacity of 475 mA h g^{-1} was obtained when heated to 60°C, compared to 310 mA h g^{-1} at 20°C. Layered birnessite (δ-MnO_2) was also studied to examine the effects of the microstructure, and showed poorer performance relative to the hollandite phase. A maximum initial capacity of 109 mA h g^{-1} was obtained for a Mg-ion exchanged birnessite-acetylene black composite electrode. However, in all cases, the capacity deteriorated below ~60 mA h g^{-1} within 20 cycles. The rapid fading was attributed to leaching of soluble Mn species from the cathode into the electrolyte.

Octahedral molecular sieves (OMS-5) are another polymorph of MnO_2 that has been studied [224]. It possesses a 4×2 tunnel structure. Pure MnO_2 molecular sieves and composites containing acetylene black were prepared from birnessite-MnO_2 hydrothermally. The carbon additive improved the capacity *vs.* pristine OMS-5, and in the limit of slow discharge (10 mA g^{-1}), the initial capacity reached ~204 mA h g^{-1}. As with previous studies, however, dissolution of the unstable Mn^{3+} hurt the capacity, which fell to ~50 mA h g^{-1} within ten cycles. The authors noted that capacity retention was inversely related to the initial capacity, possibly because higher extents of reaction produce more Mn^{3+}, which in turn destabilizes the structure of the material.

The voltage profiles recorded from galvanostatic tests in these reports all show sloping curves as opposed to plateaus, which are indicative of a true intercalation process. The various reports have at times referred to this sloping behavior as suggestive of pseudocapacitance, solid-state solution formation, or conversion reactions. However, these are all distinct phenomenon, and it is difficult to distinguish one from another from the discharge profile alone.

An interesting study combined microscopy and spectroscopy to provide evidence for conversion as the primary charge transfer mechanism in K^+-stabilized α-MnO_2 [227]. TEM images showed the progressive formation of an amorphous layer on the originally crystalline nanorods (Fig. 27). The amorphous layer formed a shell around the particles that prevented further reaction, and XAS, EELS and EDS revealed that the layer was a mixture of MnO and MgO. As is often the case with conversion reactions, the process was not fully reversible in the voltage range of the electrolyte (~3.2 V for Mg-HMDS, [234]), and is likely susceptible to pulverization and/or inactivation over the long term, even in the absence of Mn dissolution.

This result is further supported by a thorough study

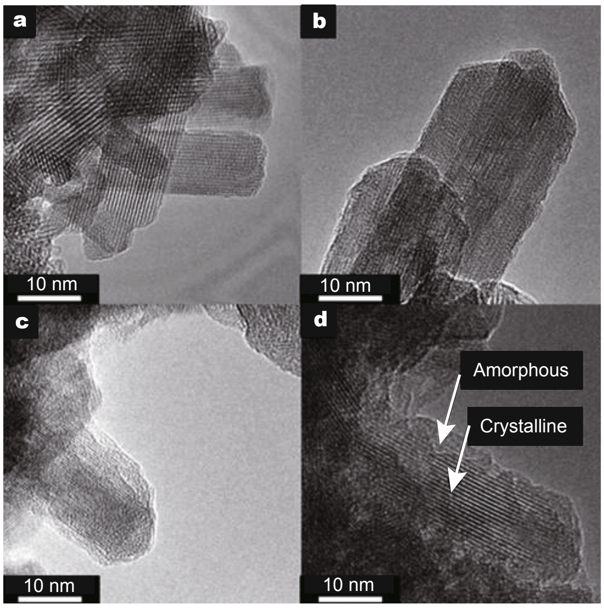

Figure 27 TEM images of MnO_2 at (a) 0% depth-of-discharge (DOD), (b) 33% DOD, (c) 66% DOD, and (d) fully discharged. Reprinted from Ref. [227], Copyright 2014, American Chemical Society.

that examined the effect of stabilizers (K^+, H_2O, Li_2O, and other ions inserted into the 1D MnO_2 channels) and polymorphs (e.g., α-, β-, γ-, δ-MnO_2). The type and amount of stabilizer had only minor effects on capacity, and even the 1×1 β-MnO_2 polymorph showed performance on par with the larger tunnel structures. Most critical was the surface area of the species. The initial capacity was linearly related to the surface area up to a capacity of ~250 mA h g^{-1} at 70 m^2 g^{-1}, above which point the capacity is kinetically controlled. Taken together, this information favors conversion rather than intercalation as the dominant mechanism, as the polymorphs with bigger and more stable tunnels would be expected to have superior intercalation performance. Capacity fading still remains a problem, however, as in each case the capacity fell below 50 mA h g^{-1} within ten cycles. Although EIS results show the amorphous layer causes an increase in charge transfer resistance with cycling [228], this layer is apparently thin enough (on the order of 1 nm [227]) that its contribution is negligible compared to the well-known issue of Mn dissolution and electrolyte decomposition catalyzed by the active material.

Along the lines of certain V_2O_5 studies and recent Na-ion results [48,180], Nam *et al.* [229] incorporated crystal water into layered MnO_2 and studied the solvation effect of water in the electrolyte. The layered oxide was prepared by galvanostatically cycling the original spinel (obtained via a hydrothermal route) in 1 mol L^{-1} $MgSO_4$. This activation process caused the capacity to gradually increase from 0 to 170 mA h g^{-1} over the course of 50 cycles, during which time the surface area increased from 3.4 to 49.5 m^2 g^{-1}. Contrast in STEM images confirmed the presence of water between layers (Fig. 28). Interplanar water appears to stabilize the host, as heating at 300°C removed the water and transformed the phase back into the spinel, which had inferior electrochemical performance. TGA measurements showed increased water content upon insertion, indicating that Mg^{2+} is co-inserted with as many as 3 water molecules. Further analysis with XRD and STEM revealed no MgO or MnO formed upon insertion, which suggests intercalation rather than conversion as reported in α-MnO_2. However, instead of Mg^{2+} residing between layers, Mg/Mn mixing takes place to accommodate insertion.

As the water content in the $Mg(ClO_4)_2$/AN electrolyte was varied from 0 to 10 mol L^{-1}, the capacity increased from 56.8 to 227.6 mA h g^{-1} at current density of 100 mA g^{-1}. Decreased overpotentials were observed in the discharge-charge voltage profiles and EIS results showed reduced cathode/electrolyte interfacial resistances as more water was added to the electrolyte. In the limit of $Mg(ClO_4)_2$ in pure water, a maximum capacity of 231.1 mA h g^{-1} and high voltage of 2.8 V were obtained. Further, excellent rate performance and long-term stability were observed. At a high rate of 2 A g^{-1} (20 times the initial rate), almost 50% of the initial capacity was retained. Even at this rate, 62.5% capacity retention (88.6 mA h g^{-1}) was observed after 10,000 cycles. This corresponds to 99.98% Coulombic efficiency over the entire testing period, and represents by far the best long-term MIB cathode performance reported to date. Of course, aqueous electrolytes cannot be used with Mg metal anodes, and would require some sort of protective membrane or water-compatible anode. Nevertheless, these results demonstrate how hydrating Mg^{2+} can lead to superior kinetic performance not often seen in oxides for MIB applications.

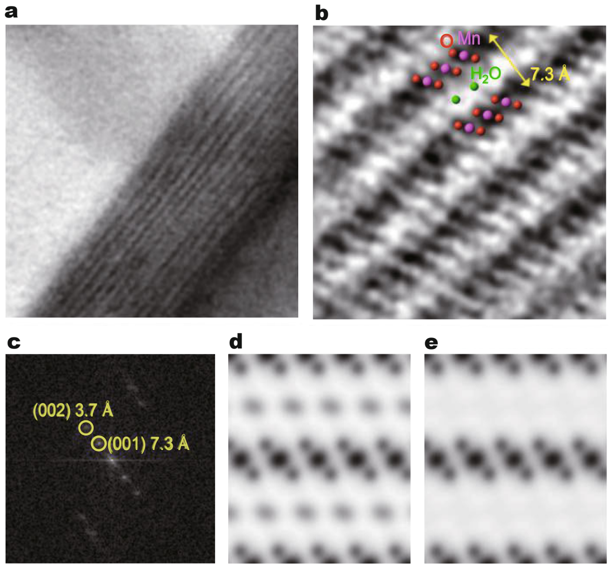

Figure 28 Annular bright field scanning transmission electron micrographs (ABF-STEM) at (a) low and (b) high magnification. The fast Fourier transform of (b) is shown in (c). Simulated ABF-STEM images (d) with and (e) without water demonstrate the contrast expected. Reprinted from Ref. [229], Copyright 2015, American Chemical Society.

Another study demonstrated charge screening with water, even in dry electrolytes [232]. Amorphous MnO_2 nanowires (~200 nm wide, ~4.5 μm long) were electrodeposited using an anodized aluminum oxide template. Consistent with other results [116,229], water shielded the charge to reduce the kinetic barrier to intercalation at the electrode interface, thus enabling improved reversible electrochemistry. Cyclic voltammograms taken at a scan rate of 0.5 mV s^{-1} showed that the optimum electrolyte composition was 0.1 mol L^{-1} $Mg(ClO_4)_2{\cdot}6H_2O$/PC, at which point a composition of $Mg_{0.69}MnO_2$ was obtained (corresponding to a high capacity of ~425 mA h g^{-1}, and indicating partial reduction from Mn^{4+} to Mn^{2+}). The synergetic effect of both the nanostructure and water was also noted, as the nanowires in water-containing electrolyte outperformed electrodes where only one aspect was incorporated into the electrochemical setup. An initial capacity of ~160 mA h g^{-1} was obtained in a three-electrode cell with activated carbon reference and counter electrodes at a 1.6 C rate (Fig. 29). The capacity retention was very good, with 67% remaining after 200 cycles. Further, reversible performance was possible in dry electrolyte. As in Ref. [229], electrochemical quartz microbalance (EQMB) measurements showed co-insertion of ~3 water molecules per Mg-ion. After "activating" cathodes by cycling in wet electrolyte, cyclic voltammograms showed new redox peaks in the water-free electrolyte. This effect was observed in both the charged and discharged state, indicating that water molecules stay in the host structure even as Mg^{2+} is removed. Extended cycling in a dry electrolyte with an "activated" cathode was not as good as in the wet electrolyte, but still showed an initial capacity of ~120 mA h g^{-1} and ~70% retention after 100 cycles at a 0.4 C rate.

Manganese oxide spinels (λ-MnO$_2$) have also received relatively significant attention, owing to their commendable performance in LIBs [235]. Relatively low strain and negligible capacity for co-intercalation of the solvent during cycling are features that are suggestive of good long-term stability [99], and a mix of both experimental and computational studies have been published.

Kurihara *et al.* [217] prepared spinel MgMn$_2$O$_4$ from MgO and Mn$_2$O$_3$ powder via a microwave discharge synthesis analogous to Ref. [200] The capacity increased with the microwave power, up to as much as ~90 mA h g^{-1} at 500 W, and retained ~60 mA h g^{-1} after nine cycles. Yuan *et al.* [225] studied Mg^{2+} and Zn^{2+} insertion into spinel MnO$_2$ in aqueous electrolytes. The λ-MnO$_2$ phase was obtained by leaching Li$^+$ from LiMn$_2$O$_4$ with sulfuric acid. MgCl$_2$ showed higher ionic conductivity and performance than MgSO$_4$ or Mg(NO$_3$)$_2$. A very high capacity of 545.6 mA h g^{-1} was obtained in 0.5 mol L^{-1} MgCl$_2$ at a discharge rate of 13.6 mA g^{-1} (Fig. 30). This high capacity corresponds to full reduction of Mn^{4+} to Mn^{3+}, with additional partial reduction to Mn^{2+}, which was corroborated by XPS and XRD results. The spinel obtained from the acid leaching step was apparently quite stable, as extended cycling at a current density of 136 mA g^{-1} yielded a capacity of 155.6 mA h g^{-1} after 300 cycles (~60% capacity retention).

Kim *et al.* [226] prepared spinel MgMn$_2$O$_4$ by the Pechini method, a solution-based technique that gives nanosized particles (~10 nm). Acid leaching with H$_2$SO$_4$ for 5 h produced a mixture that was roughly 75% λ-MnO$_2$ and 25% α-MnO$_2$, while extended leaching for 36 h caused further transformation to ~75% α-MnO$_2$ and ~25% β-MnO$_2$. When tested in three-electrode cells with Mg(ClO$_4$)$_2$/AN as the electrolyte, Ag/Ag$^+$ as the reference and Pt as the counter electrode, the initial capacities were ~330 mA h g^{-1} for the spinel-rich mixture and ~210 mA h g^{-1} for the hollandite-rich material. The superior performance was rationalized in terms of impedance spectra, which showed a lower charge-transfer resistance for the spinel-rich cathode, and DFT calculations that predicted more favorable absorption on the spinel compared to the tunneled phase (5.7 *vs.* 2.0 eV, respectively). However, poor cyclic stability was displayed in both cases (<60% after only five cycles). EIS measurements implicated decomposition of AN as part of the problem, and the cyclability improved when tetramethylsilane was substituted as the solvent (although the increased viscosity lead to a lower capacities overall, ~76.3 mA h g^{-1}).

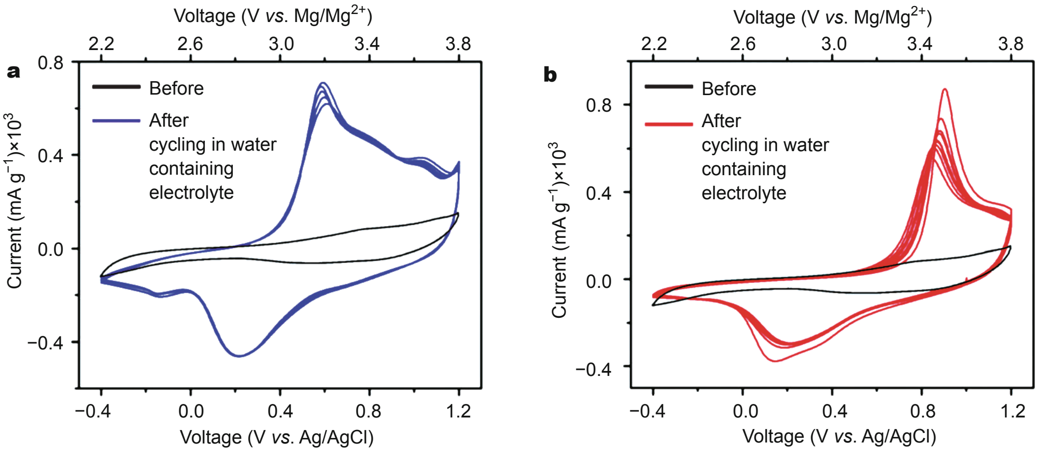

Figure 29 Cyclic voltammograms obtained before and after conditioning the electrode in water-containing electrolyte, starting from either (a) the discharged or (b) charged state. Reprinted from Ref. [232], Copyright 2015, the PCCP Owner Societies

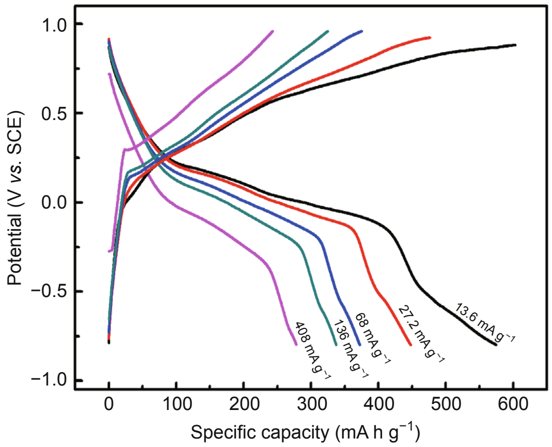

Figure 30 Galvanostatic voltage profiles obtained at the indicated current densities for spinel MnO_2 using aqueous 1 mol L^{-1} $MgCl_2$ as the electrolyte. Reprinted from Ref. [225], Copyright 2013, Elsevier.

Thus, this is another instance where the choice of electrolyte has a significant effect on cathode performance.

Defect spinel $Mg_{1.5}MnO_3$ has also been synthesized via the Pechini route [106]. CV studies indicated very low energy density. Two redox reactions centered at ~0.61 and ~1.0 V are observed and capacities of ~12.6 mA h g^{-1} were obtained, although 99.9% Coulombic efficiency was maintained for 100 cycles.

Direct Mg^{2+} intercalation into tetrahedral sites of spinel MnO_2 was recently reported, effectively demonstrating the versatility of TEM paired with complimentary spectroscopic techniques [211]. XRD spectra taken at different states of charge coupled with XAS and ^{25}Mg nuclear magnetic resonance (NMR) showed progressive tetragonal distortion of the spinel, consistent with the reduction of Mn^{4+} to Jahn-Teller active Mn^{3+} and the formation of $MgMn_2O_4$. STEM images combined with EDX spectra provided very clear evidence for insertion (Fig. 31). While most tests were performed in the aqueous electrolyte, similar XRD patterns were observed for cathode discharged in nonaqueous solvents (diglyme or PC), but lower capacities and more pronounced hysteretic behavior were obtained.

Okamoto *et al.* [230] used a combination of electrochemical, structural, and *ab initio* analyses to study several spinels ($MgCo_2O_4$, $MgMn_2O_4$, $MgFe_2O_4$, $MgCrO_2$, and Co_3O_4), and suggest spinel $MgMn_2O_4$ may be a viable above-room-temperature (150°C) MIB cathode material. The operating temperature was selected to improve solid state diffusion and accommodate the ionic liquid electrolyte (Cs-bis(trifluoromethane sulfonyl)amide (TFSA)), whose melting point is 120°C. XRD showed the coherent formation of a rock salt phase upon intercalation (discharge). XANES spectra reveal oxidation state changes upon charging and discharging, suggesting that the material then reverts back to the spinel upon charging (Fig. 32). The equilibrium potentials for $Mn^{4+/3+}$ and $Mn^{3+/2+}$ redox couples were 3.4 and 2.3 V, respectively. A capacity in the range of 150–200 mA h g^{-1} was also observed, but this was

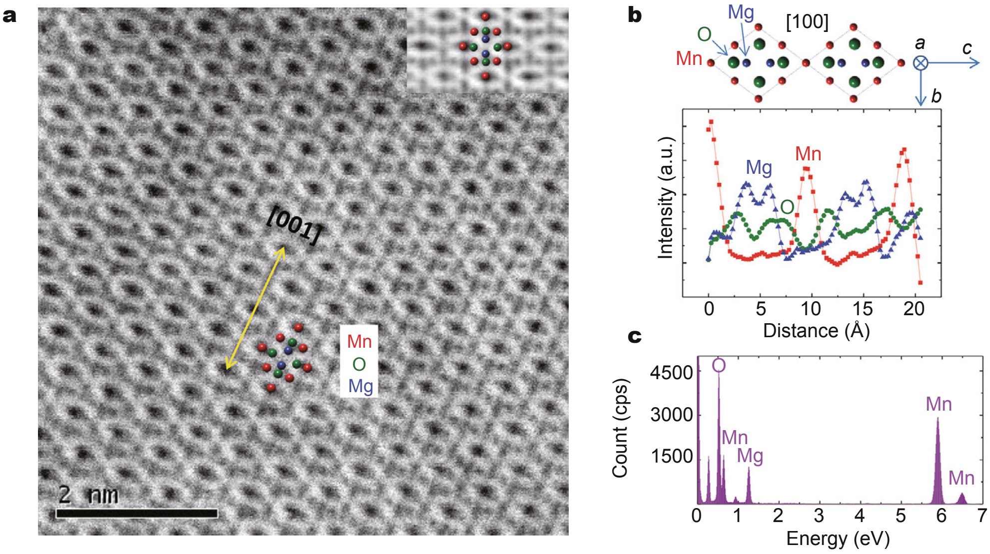

Figure 31 (a) ABF-STEM image taken for a fully discharged spinel viewed along the [100] zone axis, with atom positions as indicated by red (Mn), green (O) and blue (Mg) spheres and a cross-correlated image inset. (b) An EDS line scan taken along the same direction as the yellow line in (a) shows the atomic arrangement of atoms in the spinel. (c) The integrated EDX spectra shows ~11 at.% Mg. Reprinted from Ref. [211], Copyright 2015, WILEY-VCH Verlag GmbH & Co. KGaA, Weinheim.

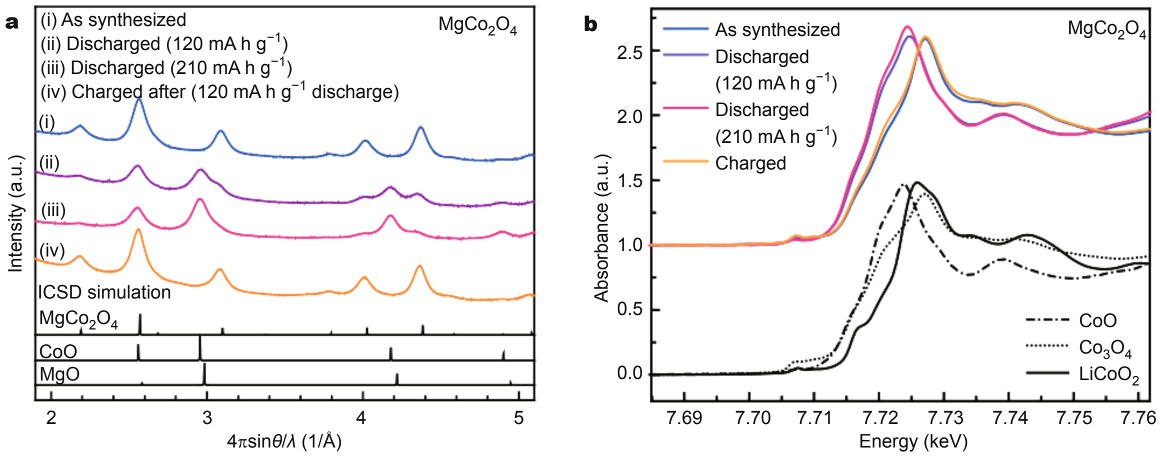

Figure 32 XRD spectra (a) indicate phase changes upon charge and discharge, while XANES spectra (b) demonstrate the conversion between Co oxidation states for $MgCo_2O_4$. Reprinted from Ref. [230], Copyright 2015, WILEY-VCH Verlag GmbH & Co. KGaA, Weinheim.

apparently limited by the electrochemical window of the electrolyte and strain from lattice mismatch between MnO and MgO in the rock salt.

Another DFT study looked at a wide range of spinels for multivalent batteries [123]. In total, 35 combinations of AB_2O_4 were studied, where A = {Ca, Zn, Mg, Al, and Y} and B = {Ti, V, Cr, Mn, Fe, Co, Ni}. The average voltage for $MgMn_2O_4$ is about 1 V lower than that of the corresponding Li spinel, but still has a higher theoretical energy density since it has twice the capacity compared to Li ions. Further, it showed the highest thermodynamic stability both in the charged and discharged state, and doesn't decompose until 342°C. The Mg diffusion barrier was higher than ideal at ~800 meV, but not unusual for MIB cathodes.

Ling and Mizuno [223] studied post-spinel AMn_2O_4 as a host for A = {Li, Na, Mg} ions from first principles. At high pressures, the spinel undergoes a transition that leads to one of three kinetically stable phases at ambient conditions. These phases form 1D channels that are predicted to have high ionic mobility. In particular, the calculated diffusion barrier for $CaFe_2O_4$-type Mg post-spinel was ~0.4 eV. At the same time, the discharge voltage ranges from 2.84 to 1.68 V as insertion takes place, making this material worth considering as a MIB cathode.

(iii) Molybdenum oxides. MoO_3 is an orthorhombic layered material that is assembled from corner-sharing MoO_6 octahedra. Initial tests with MoO_3 showed an V_{oc} of 2.28 V and a capacity of 143 mA h g^{-1} for $Mg_{0.5}MoO_3$ [97]. Spahr *et al.* [236] followed this up by reversibly cycling MoO_3 in an ionic liquid electrolyte and $Mg(ClO_4)_2$/AN with 3 mol% water added. As with vanadium oxides [116], the presence of water was crucial to the cyclability, as the 'dry' aprotic electrolyte could not support Mg electrochemistry. However, amorphization of the host material upon cycling led to limited long-term cycling.

In the context of studying electrochromic behavior, Sian and Reddy [237] measured very low diffusivity of Mg in amorphous MoO_3 (~10^{-17} cm^2 s^{-1}). Pandey *et al.* [238] used MoO_3 as a cathode in a cell with a solid electrolyte cell with Mg and multiwalled carbon nanotubes (CNTs) as the anode. They achieved ~175 mA h g^{-1} for ten cycles. The only thorough study of MoO_3 as a cathode material was conducted by Gershinsky *et al.* [201]. An electrodeposited thin film (~100 nm) of MoO_3 was used to probe its intrinsic behavior. Electrochemical and spectroscopic tests showed very large overpotentials and a large volume change upon intercalation, which appears to lead to disintegration and charge trapping over time. Nevertheless, a two-stage intercalation process at 1.80 and 1.74 V was observed, with a high capacity of ~200 mA h g^{-1} and ~95% Coulombic efficiency for ten cycles.

(iv) Other transition metal oxides. As with the TMCs, a variety of other transition metal oxides have been studied as Mg hosts, with largely unremarkable results. In addition to the oxides mentioned above, Gregory *et al.* [97] screened Co_3O_4, RuO_2, WO_3, and two lead oxides. The lead oxides showed high V_{oc} (3.10 V), but very low extents of intercalation (<56 mA h g^{-1}) and are obviously not attractive on an energy density-per-mass basis. WO_3 had a moderate voltage and intercalation capacity (2.16 V, 116 mA h g^{-1}), but very low intercalation was observed by Bruce *et al.* [169] and has not been investigated further. The potential and capacity for RuO_2 were both fairly high (2.55 V, 266 mA h g^{-1}), but subsequent studies found only irrerversible behavior [116] or severe overpotentials and capacity fading [239]. Uranium oxide (U_3O_8) reversibly inserted Mg^{2+} in both aqueous and nonaqueous electrolytes. Similar phases were observed in each electrolyte, and the phases became more Mg-rich when cycled at 100°C. The highest extent of intercalation achieved was $Mg_{0.78}U_3O_8$, where a new phase was observed [240].

Unlike $LiCoO_2$ and many other successful Li-intercalation hosts, magnesiated cobalt oxides have not yet proven to be promising for MIB cathodes. A preliminary test in a full cell configuration showed high polarization and a low discharge voltage for Co_3O_4 [97]. Sutto and Duncan [241] tested Co_3O_4 in an ionic liquid electrolyte, but as with RuO_2 [239], found poor electrochemical performance. XRD results indicated ~20% volume change upon intercalation, and the capacity decreased linearly with cycling. The capacity retention was only 60% after 30 cycles.

Spinel $MgCo_2O_4$ was investigated by Kamioka *et al.* [242]. A solid state synthesis was not successful, but a wet chemical route using the metal nitrates followed by heat treatment gave the desired material. Its electrical conductivity was comparable to $LiCoO_2$ (~10^{-2} S cm^{-1}). Later, researchers from the same university studied the classical high voltage Li hosts, CoO_2 and NiO_2 [243]. Co-precipitation from the appropriate metal nitrates (analogous to Ref. [242]) was employed to prepare $MgCo_2O_4$ and $Mg_{0.67}Ni_{1.33}O_2$. The presence of unstable valence states such as Co^{4+} led to high V_{oc} around 3.5–3.9 V *vs.* Li/Li^+, although Mg diffusion appeared to be quite low. As mentioned above, Okamoto *et al.* [230] studied various spinels ($MgCo_2O_4$, $MgMn_2O_4$, $MgFe_2O_4$, $MgCrO_2$, and Co_3O_4) as cathodes at elevated temperatures in an ionic liquid electrolyte. While these materials possessed reasonably high voltages (2.2–2.9 V), all except the $MgMn_2O_4$ spinel were ruled out as likely battery materials. $MgFe_2O_4$ and $MgCrO_2$ are unlikely MIB cathodes since energetically unstable FeO and CrO phases are formed in the rock salt phase, and are liable to disproportionate. At the same time, $MgCo_2O_4$ requires prohibitively high overpotentials to remove Mg from the lattice. Quite similarly, Liu *et al.* [123] studied a range of transition metal oxide spinels (MgB_2O_4, for B = {Ti, V, Cr, Mn, Fe, Co, Ni }) from first principles and came to the same conclusion that $MgMn_2O_4$ is the most promising material in the set because of its high stability and good energy density. High voltages between 2.5 and 4.0 V for the various redox metals are expected, except for $MgTi_2O_4$, which cannot compete with current LIB energy densities. The other spinels have issues with stability. Cr_2O_4 and V_2O_4 are not particularly stable in the charged state. Fe_2O_4 and Ni_2O_4 have high voltages but are inherently unsafe in that they are likely to evolve O_2 at room temperature, and Co_2O_4 decomposes around 100°C.

Lastly, TiO_2 has been reported for the first time as an MIB host [244,245]. Commerical TiO_2 was tested without further processing (besides addition of carbon and binder) in a full cell configuration using a Mg metal anode and an $Mg(BH_4)_2$/$LiBH_4$/glyme electrolyte [245]. Although the discharge voltage was low (~0.9 V), so was voltage polarization (~0.3 V) (Fig. 33a). Further, a capacity of ~140 mA h g^{-1} was retained for 90 cycles (Fig. 33). This corresponds to a ~10% capacity loss, a significant fraction of which is lost after the first cycle. In addition to very good cycle life, good rate capacity was reported. Over 50% of the capacity was retained at a 2 C rate compared to the initial capacity seen at 0.1 C. This performance was strongly determined by the electrolyte, as no effort was made to modify the morphology of the TiO_2 powder. The best performance was observed when the Li/Mg content in the electrolyte was 3:1, in which case ICP-MS and EDS show co-intercalation of both Li and Mg. In contrast, a Mg-compatible organohaloaluminate electrolyte 0.4 mol L^{-1} $(PhMgCl)_2$-$AlCl_3$/THF gave poor electrochemical results, thus underscoring the importance of the appropriate choice of electrolyte in MIB systems.

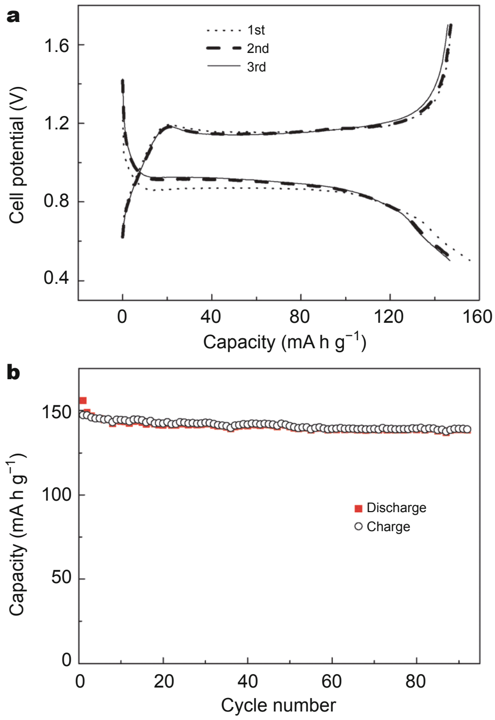

Figure 33 (a) Galvanostatic voltage profiles for the first three cycles of a Mg/TiO_2 coin cell at a 0.2 C rate. (b) Charge and discharge capacities obtained for the cell cycled at 0.2 C rate. Reprinted from Ref. [245], Copyright 2015, Royal Society of Chemistry.

While the enhanced ionic character of TMOs implies higher voltages and energy densities in MIB cathode materials, the penalty has been stronger electrostatic interactions with Mg^{2+}. This gives rise to higher kinetic barriers to insertion and diffusion that have thus far been hard to overcome. Attempts at charge screening and controlling the morphology have been the primary methods of improving performance, along with cation and sulfur doping. Attention needs to be paid to the electrochemical setup to ensure compatibility with all the cell components. Significant advances to the lifetime and rate performance of these materials are needed before any will be competitive with LIB technology.

Polyanion compounds

Analogous to the commercially successful $LiFePO_4$ [246], a variety of olivine-type materials with redox-active metal centers have been investigated as MIB cathode materials. In general, these materials can offer good energy density and benefit from relatively "green" source materials and syntheses. The inductive effect of the oxoanion groups helps to raise the voltage of these compounds relative to oxides, while polyanion groups such as phosphates have demonstrated very high ionic mobility [247]. For the most part, these studies have focused on transition metal phosphates and silicates. These classes of materials can transfer one or two electrons per metal atom, respectively, and additional anion substitutions (e.g., F^- for PO_4^{3-}) have been made to augment the voltage.

(i) Phosphates. Makino *et al.* [248–250] investigated $Ti_2(PO_4)_3$. A sol-gel process in ethanol followed by a 24-hour annealing step gave crystalline $Mg_{0.5}Ti_2(PO_4)_3$ when the annealing temperature was 600°C. They reported negligible lattice expansion with Mg insertion, and up to 1 Mg atom could be intercalated per host molecule. However, the slow kinetics limited the usable current density to ~50 $\mu A\ cm^{-2}$, and the voltage was only ~0.6 V when adjusted to the reversible Mg couple. Replacing Ti^{4+} with Fe^{3+} or Cr^{3+} did not improve the performance of the phosphate, but did slightly shrink the size of the unit cell. The smaller unit cell was correlated with more stringent kinetic limitations to Mg insertion, which is reasonable given the expectation that a smaller volume should lead to more severe electrostatic effects.

Ling *et al.* [122] studied a variety of olivine compounds with Co, Ni, Fe, and Mn metal centers using DFT calculations. For the olivine phosphates, only $TMPO_4$ and $Mg_{0.5}TMPO_4$ phases are expected, which corresponds to reduction from TM^{3+} to TM^{2+} upon intercalation of magnesium. $Mg_{0.5}FePO_4$ was proposed as a viable MIB candidate cathode owing to its moderate volume change upon magnesiation (~7%, similar to $LiFePO_4$), and a predicted voltage (~2.5 V) within the electrolyte limit at the time of publication (Fig. 34). The rather large ~12% volume change for $MnPO_4$ is likely untenable, unless nonequilibrium pathways exist that avoid pulverizing the cathode during cycle, analogous to $LiFePO_4$ [210], while Co and Ni phosphates both have superior voltages and smaller volume changes than $Mg_{0.5}FePO_4$, but require electrolytes stable beyond 3.5 V.

Huang *et al.* [251] investigated a closely related phosphate, $MgFePO_4F$. The reactants, $MgHPO_4$, $FeC_2O_4{\cdot}2H_2O$, and NH_4F, were ball milled in a dispersion of CNTs in ethanol. The mixture was annealed at 600–850°C and ball milled again to obtain the final $MgFePO_4F$/CNT composite. Characterization of the material revealed particle sizes of ~50 nm and disordered Fe/Mg cation site occupation, which likely blocked off Mg^{2+} diffusion pathways. $MgFePO_4F$ displayed a relatively low capacity of ~53 mA h g^{-1}, or less than 40% of the theoretical capacity of 138 mA h g^{-1}, and dQ/dV plots indicated wide redox peak separation of ~0.93 V. However, the average potential of ~2.6 V is quite high, which makes $MgFePO_4F$ an attractive potential cathode material if cation mixing and poor kinetics can be avoided. The same authors [252] also studied another high-voltage material, $V_2(PO_4)_3$. The material was obtained after fully delithiating $Li_3V_2(PO_4)_3$ by discharging a composite electrode at 55°C at a slow rate of C/20. $Li_3V_2(PO_4)_3$ was itself prepared from a similar procedure compared to that described in Ref. [251]. Very high energy density was

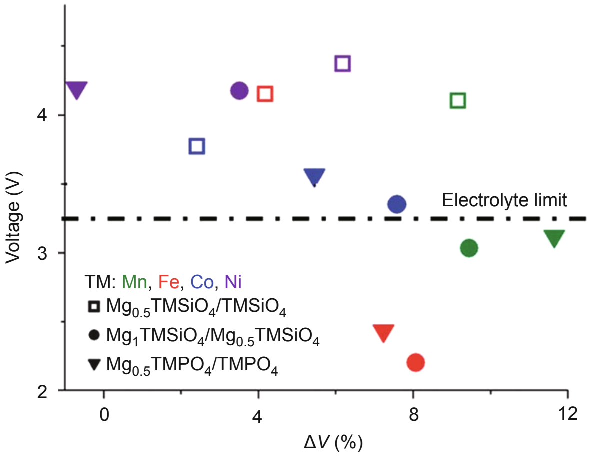

Figure 34 Scatterplot of the voltage and volumetric change for the $TM^{4+/3+}$ (for silicates) and $TM^{3+/2+}$ (for both phosphates and silicates) reactions, where TM = {Mn, Fe, Co Ni}. The dotted line indicates the electrolyte voltage limit at the time of publication [234]. Reprinted from Ref. [122], Copyright 2012, Royal Society of Chemistry.

reported. An average voltage of ~2.9 V and a capacity of ~200 mA h g^{-1} were obtained when the delithiated composite was cycled in a three-electrode cell with 0.5 mol L^{-1} $Mg(TFSI)_2$ as the electrolyte (Fig. 35).

Another phosphate derivative, $MgVPO_4F$, was investigated from first principles by Wu *et al.* [253]. As with Ref. [251], the introduction of F^- is intended to reduce Mg-anion interactions and increase the ionic conductivity of the host material. Again, a reasonably high voltage was predicted. Two insertion plateaus at 2.6 and 1.5 V were calculated for V^{4+}/V^{3+} and V^{3+}/V^{2+}, respectively. This, in turn, corresponds to the stepwise formation of $Mg_{0.5}VPO_4F$ and $MgVPO_4F$. However, while fully discharged $MgVPO_4F$ has a theoretical capacity of over 300 mA h g^{-1}, they found that Mg_xVPO_4F undergoes ~17% lattice expansion as x is varied from 0 to 1. To avoid structural instability with cycling, they suggest limiting the extent of intercalation. Lastly, they calculated the activation energies for Mg diffusion along various pathways. The most favorable path was along the [111] direction and had a relatively low energy barrier of 0.704 eV.

(ii) Silicates. Feng *et al.* [254,255] were the first to study manganese silicates, which have a high theoretical capacity of ~313 mA h g^{-1} with respect to $MgMnSiO_4$. $Mg_{1.03}Mn_{0.97}SiO_4$ was prepared by both solid state and sol-gel routes. The high-temperature solid-state reaction yielded large, coarse particles (on the order of microns) and poor electrochemical performance relative to the sol-gel synthesis. The sol-gel product was prepared using the respective metal acetates and nanosized SiO_2 powder, and the particle size was below 100 nm. While the solid-state product delivered a maximum capacity of 64.5 mA h g^{-1}, the sol-gel product reached a high capacity of 244 mA h g^{-1} when discharged in a coin cell using the DCC electrolyte and Mg as the anode. Voltage plateaus at ~1.6 and ~1.1 V indicate the presence of two distinct insertion sites [254]. A slightly different sol-gel method used tetraethyl silicate as the silicon source and similar particle sizes, but the performance was poorer. *In situ* pyrolysis with sucrose as a carbon source was superior to carbon coating via ball milling with acetylene black, but the maximum capacity for the latter composite was less than 100 mA h g^{-1}, even at a low discharge rate of C/50, and fell below 40 mA h g^{-1} at a C/10 rate [255].

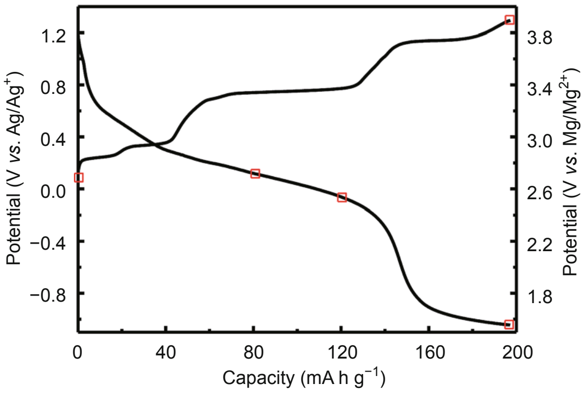

Figure 35 The voltage profile for the first discharge and charge processes for $Mg_xV_2(PO_4)_3$. Reprinted from Ref. [252], Copyright 2014, Royal Society of Chemistry.

NuLi *et al.* [256–258] then reported a third preparation method using a molten salt synthesis with KCl as flux. The ~8 h synthesis compared favorably to the 24 h sol-gel steps at 700–900°C and 10 h solid-state synthesis at 1250°C. The temperature affected the final particle size, with micron-sized particles obtained at 1000°C and 80–90 nm sized particles obtained at 800°C. The nanosized particles showed better capacity retention than the microparticles after 80 cycles at a C/5 rate (120 *vs.* 96 mA h g^{-1}, respectively), which was attributed to the larger surface area for intercalation [256]. Replacing bulk SiO_2 with a mesoporous silicate template in the synthesis further improved performance. Relatively high initial energy density (~1.65 V, 301.4 mA h g^{-1}) was obtained with one mesoporous silicon template, while 96% of an initial capacity of 214.2 mA h g^{-1} was retained after 20 cycles for another template when the discharge rate was C/5 [257]. Growing CNTs on powder as obtained in Ref. [256] also boosted performance, especially rate capacity. The electrical and mechanical properties of the CNTs helped reduce cracking and gave a capacity of ~300 mA h g^{-1} cycled at a C/5 rate, with 120 mA h g^{-1} retained when the rate increased to C/2 [258].

The same researchers have also explored iron and cobalt silicates. Li *et al.* [259] prepared $MgFeSiO_4$ using the molten salt method. The electrochemical performance was best when the synthesis temperature was 900°C, as evidenced by EIS and charge-discharge tests with coin cells using DCC as the electrolyte and Mg anodes. The initial capacity was 125.1 mA h g^{-1} with 91.4% capacity retention after 20 cycles at a current density of C/10.

A hydrothermal synthesis was employed to prepare $MgCoSiO_4$, which was then heated in the presence of polystyrene beads as a template to give a mesoporous cathode material. Calcining the material at 700°C led to the largest measured surface area and pore volume, which contributed to its good electrochemical performance. Lower temperatures did not yield the desired product, as evidenced by XRD, while higher temperatures deteriorated the connected structure of the material. The initial capacity was

271.1 mA h g^{-1}, or roughly 90% of the theoretical capacity, and ~120 mA h g^{-1} remained after 200 cycles when cycled at a C/4 rate [260]. Another study compared $MgCoSiO_4$ prepared by solid state, molten salt, and solvothermal methods [261]. The solvothermal method was similar to that employed in Ref. [255]. Material produced using this method had a mesoporous structure and higher surface areas than the other two methods (13.3 m^2 g^{-1}, compared to 0.03 and 1.79 m^2 g^{-1} for the solid state and molten salt methods, respectively), which was cited as the reason for the improved electrochemical performance [261]. While the voltage improved slightly (~1.7 V), the maximum capacity of 167 mA h g^{-1} at C/10 is only marginally better than that observed with iron as the redox active species, and not yet on par with the best results for manganese silicates.

The DFT study by Ling *et al.* [122] also included silicates, in particular $MgMnSiO_4$. Thermodynamic data for the formation energies of various Mg_xMnSiO_4 compounds, coupled with the results of density of states and Bader charge analysis suggested a two-step redox mechanism. In the first step, insertion of one Mg^{2+} ion reduces two separate Mn^{4+} metal centers to Mn^{3+}. The next step forms two Mn^{2+} ions after another Mg^{2+} ion is inserted. This corresponds to the sequential formation of $Mg_{0.5}MnSiO_4$ and then $MgMnSiO_4$, rather than solid solutions of intermediate composition. This two-step mechanism was consistent with the analysis for Fe, Co and Ni silicates as well. The predicted average voltages for the silicates were all significantly higher than what has been observed experimentally (>3.0 V for the average of the TM^{4+}/TM^{3+} and TM^{3+}/TM^{2+} couples, compared to ~1.6–1.7 V as mentioned in the studies described above). This may be a function of electrolyte solvation effects as proposed by Ichitsubo *et al.* [149] that drive down the voltage. Full magnesiation of $MnSiO_4$ up to $MgMnSiO_4$ showed the largest volume change at ~20% and the same process in the other silicates leads to expected changes in excess of 10%, which suggests that limits on the cycling range may be required to avoid straining the lattice of the silicates.

Most recently, Orikasa *et al.* [262] prepared $MgFeSiO_4$ by electrochemically replacing lithium in the original Li_2FeSiO_4 host with magnesium (Fig. 36). Preparing the metastable magnesium iron silicate in this way avoided the problem of Mg/Fe cation mixing, thus keeping diffusion channels open. Using $Mg(TFSI)_2$/AN as the electrolyte, $FeSiO_4$ was magnesiated up to a high capacity of ~330 mA h g^{-1} at a high average discharge voltage of ~2.4 V. The estimated energy density was 746 Wh kg^{-1}, which is the highest reported value to date for an MIB cathode. XRD results indicate that the orthorhombic structure

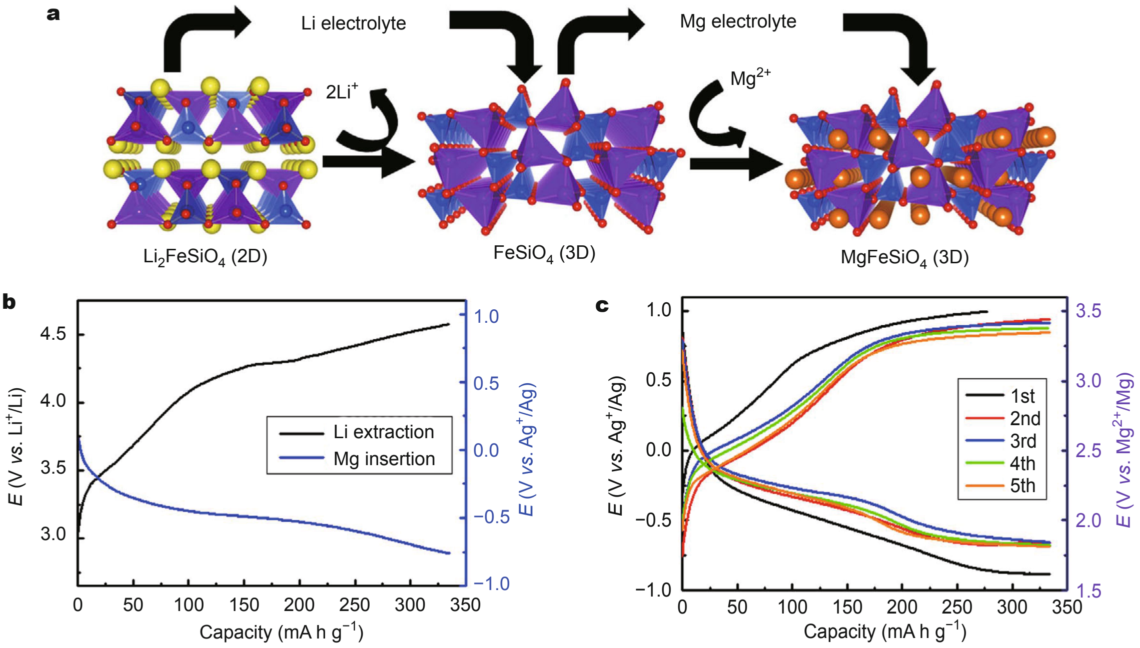

Figure 36 (a) Schematic describing the removal of Li^+ from Li_2FeSiO_4 and subsequent magnsiation. (b) Li^+ extraction up to a charge capacity of 330 mA h g^{-1} took place in $LiClO_4$/PC with Li as the reference and counter electrode. Magnesiation was performed at a 55°C at a current density of 6.62 mA g^{-1} in $Mg(TFSI)_2$/AN with Mg and Ag counter and reference electrodes, respectively. (c) The first five charge-discharge curves obtained under the same experimental conditions as (b) shows reversible Mg-insertion. Reprinted from Ref. [262], Copyright 2014, Nature Publishing Group.

$FeSiO_4$ is retained upon Mg intercalation, and suggests a 3D Mg diffusion path. A practical prototype cell was built using triglyme as the solvent instead of AN. This electrolyte is stabile up to ~3.5 V, and simultaneously supports Mg stripping/deposition without corrosive or low-boiling constituents. The full $MgFeSiO_4|Mg(TFSI)_2$/triglyme|Mg cell showed a good albeit significantly reduced capacity of 166 mA h g^{-1}. However, high polarization was observed even at an elevated temperature of 100°C and a slow discharge rate of C/50, which is suggestive of slow transport in the host and/or electrolyte.

(iii) Other polyanion compounds. Wu *et al.* [263] conducted a study similar to their previous work with VPO_4F that considered $FeSO_4F$ from first principles. The discharge voltage was predicted to be 2.52 V, which corresponds to the Fe^{3+}/Fe^{2+} redox process and magnesiation up to $Mg_{0.5}FeSO_4F$. The unit cell is expected to expand by ~11% during this process, which is relatively severe, but a low activation energy for Mg transport (0.36 eV) was calculated along the [010] direction. While such diffusion calculations do not take into consideration electronic conductivity or defects in the material [264], the authors rationalize how Mg diffusion should be comparable to that observed for Li in the same host.

Magnesium borates were recently reported for the first time as well [265]. In principle, $MgVBO_4$ offers a high capacity of ~360 mA h g^{-1}. However, attempts at thermal and chemical oxidation showed no Mg-ion mobility whatsoever, which precludes it from MIB applications. Another borate, $Mg_xFe_{2-x}B_2O_5$, appears to be more promising. This material is composed of units of four MO_6 octahedra connected by the $B_2O_5^{4-}$ anion groups (Fig. 37a). Bond valence modeling combined with diffraction data showed that Mg^{2+} preferentially depopulate from the middle M_B sites, although Fe^{2+} and Mg^{2+} are approximately evenly distributed over the M_A and M_B sites. Once Mg-ions are thermally excited into a neighboring interstitial site, the cation can move along the *a*-axis. The preferred diffusion path links interstitial sites between two M_B sites (denoted I_B), which have a more open geometry than I_A sites. The arrangement of MO_6 octahedra creates "parking lot" aisles that are not affected by cation disorder, although Mg^{2+} is only mobile at relatively high temperatures ($T > 250$°C).

While these results are preliminary, they suggest how polyanion compounds may come to constitute a class of high energy density MIB cathodes. However, despite high voltages and capacities, the kinetics remain slow. It is reasonable to expect that enlarging the unit cell (for example, through the appropriate choice of cation or anion dopants) may prove to be an effective way to improve the transport kinetics, while employing new high-voltage electrolytes may lead to improved surface reaction kinetics.

Alternative battery materials

(i) Borides. Initial screening by Gregory *et al.* [97] showed high intercalation levels in excess of 300 mA h g^{-1} and moderately low V_{oc} around ~1.2 V. However, the reversibil-

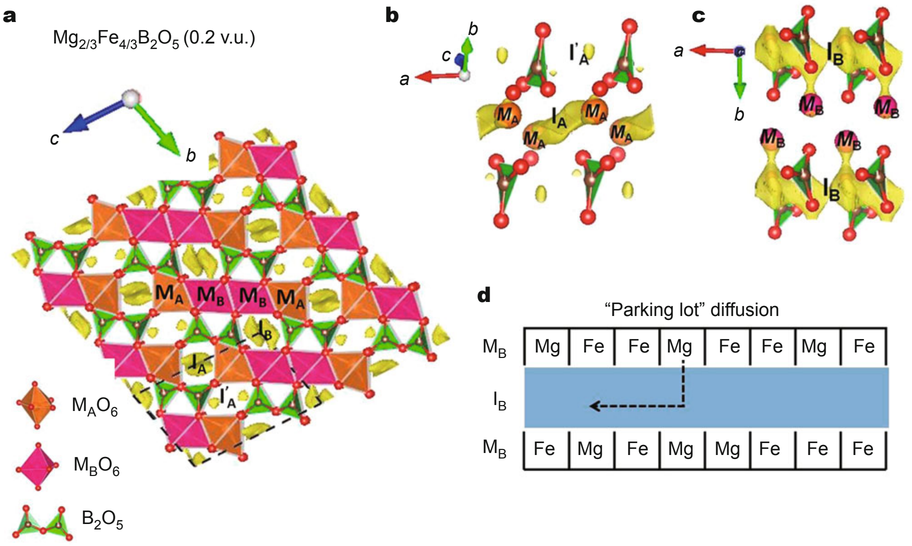

Figure 37 (a) Diffusion paths in the [100] direction are indicated in yellow at a threshold of 0.2 valence units (v.u.). (b) The threshold for a connected diffusion path in aisles of I_A sites is ~0.5 v.u. (c) For I_B-connected aisles, the threshold is lower (0.2 v.u.). (d) Excitation and diffusion along these aisles resembles a car pulling out of a parking lot. Reprinted from Ref. [265], Copyright 2015, American Chemical Society.

ity was apparently minimal and no further interest in the borides was shown until a recent paper by Zhao *et al.* [266]. Their computational study suggests that layered magnesium borides may function as high-capacity cathode materials owing to the continuum of valence states available to planar boron sheets. While the predicted voltage was quite low (0.64 V), they predict stable cycling for Mg_xB_{32} in the range of $4 < x < 16$, corresponding to a capacity of 876 mA h g^{-1}.

(ii) Organic cathode materials. An eclectic mix of carbonaceous materials has been proposed as rechargeable MIB cathode materials. Carbon-based materials have a number of potential advantages, including low toxicity, and low materials and manufacturing costs. Additionally, the absence of highly ionic bonds reduces electrostatic effects that stymie diffusion in inorganic hosts.

As an alternative to transition metal intercalation electrodes, Zhang *et al.* [267] investigated the electrochemical behavior of fullerenes. Although the energy density is relatively low (~1.6 V, ~50 mA h g^{-1}), high rate capability was obtained. Raman and XPS evidence suggests that strong delocalization of electrons on the C_{60} molecule easily allows for charge neutrality as Mg^{2+} is inserted and removed. In this way, the electrode retained 44% of its capacity when discharged at 1515 μA cm^{-2} (relative to the capacity obtained at 19 μA cm^{-2}, or ~80 times slower).

NuLi *et al.* [268] proposed organosulfur compounds that reversibly stores energy using the –SH/S–S redox couple, similar to sulfur conversion batteries. Using poly-2,2′-dithiodianiline (PDTDA) as the active material, they obtained an initial capacity of 78 mA h g^{-1} with 80% capacity retention after 30 cycles, while polyaniline mixed with a conductive sulfur compound gave an initial capacity of 117 mA h g^{-1}. More recently, the same authors reported an improved material that uses carbyne as a conductive framework and polysulfide as the redox active material [269]. Cyclic voltammetry indicated two reduction peaks at 1.6 and 1.1 V, and galvanostatic cycling showed a high total capacity of 327.7 mA h g^{-1}, which corresponds to 53.8% of the theoretical capacity. However, the cycling capacity was much lower (~60 mA h g^{-1}) after only a 40% increase in current density (from 3.9 to 5.4 mA g^{-1}).

Sano *et al.* [270] reported on a composite with 2,5-dimethoxy-1,4-benzoquinone (DMBQ) as the active material. The cyclic stability was low, but the DMBQ cathode retained a capacity of 200 mA h g^{-1} for five cycles. Two discharge plateaus at 1.1 and 0.8 V were observed, which is attributed to the stepwise reduction of DMBQ to semiquinone and then quinone upon Mg^{2+} insertion [27]. The low voltage partly stems from the Mg wire quasi-reference electrode, which was 0.7 V higher than the reversible Mg/Mg^{2+} couple. Another redox-active organic material (poly(2,2,6,6-tetramethylpiperidinyloxy-4-yl methacrylate, PMTA) was studied by Chen *et al.* [271]. The PTMA/graphene composite only retained a capacity of ~20 mA h g^{-1} after a few cycles.

Kanakaiah *et al.* [272] used a graphite fluoride cathode and an ionic liquid-based gel electrolyte. The cell capacity was stable at ~100 mA h g^{-1} for over 500 cycles, with an average discharge voltage of ~1.6 V and good energy efficiency (97%). The good cyclability was enabled by the stability of the C-F host and the low resistivity of the SEI layer. Giraudet *et al.* [273] also studied graphite fluorides and achieved energy densities as high as 618 Wh kg^{-1} using $Mg(ClO_4)_2$/AN as the electrolyte, but did not investigate rechargeability.

(iii) Prussian blue analogs (PBAs). Metal organic frameworks (MOF) based on Prussian blue are an attractive material considered for aqueous rechargeable magnesium batteries. Despite voltages limited by the decomposition of water, these materials demonstrate high ionic conduction, and hence high rate capability [274]. The general formula is given by $A_xPR(CN)_6 \cdot yH_2O$. These materials have an open structure that is similar to perovskites (ABX_3), where A is the inserted alkali ion, and P and R are metal ions. The cyano groups force the structure open to accommodate foreign ions in the tetrahedral A sites (Fig. 38).

Wang *et al.* [275] studied a compound whose nominal formula was $KNiFe(CN)_6$. Insertion of Mg^{2+} corresponds to the reduction of some of the iron atoms from 3+ to 2+. Going from C/5 to 10 C, the MOF retained ~63% of its capacity, and had only a minor voltage hysteresis at half charge of 59 mV. After 2000 cycles at 5 C, 65% capacity retention was observed, with better than 99.7% Coulombic efficiency throughout. Capacity and retention increased to about

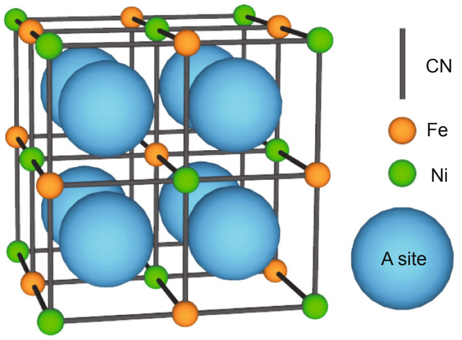

Figure 38 Representation of the PBA open framework. Reprinted from Ref. [275], Copyright 2013, American Chemical Society.

50 mA h g^{-1} and 100%, respectively upon the addition of Ni^{2+} to the electrolyte, to combat dissolution of Ni from the PBA host. The longevity is in part due to the minimal strain placed on the host, as XRD analysis showed that full insertion corresponds to a 1% volume change. Additionally, the fast kinetics were attributed to charge shielding effects of water, similar to what has been observed with V_2O_5 and shortened diffusion paths in the nanoscale PBA.

Mizuno *et al.* [276] used EIS to confirm that water reduces the charge transfer resistance at the electrolyte interface of a NiFe PBA thin film electrode, and showed insertion behavior in an aqueous electrolyte that was not possible when PC was used as the solvent. Further, the same authors synthesized a similar compound ($K_{0.1}Cu[Fe(CN)_6]_{0.7}\cdot 3.6\,H_2O$), and obtained qualitatively similar results to those obtained by Wang *et al.* [275]. A capacity of ~50 mA h g^{-1} at a current density of 100 mA g^{-1} was obtained, and retained ~74% of that capacity when the current was increased by a factor of ten. Interestingly, Mössbauer and XAS indicated that both Cu and Fe underwent redox processes upon insertion [277].

(iv) Metal chlorides. Zhang *et al.* [278] demonstrated a novel battery system that simultaneously strips or plates Mg^{2+} at the anode and transfers Cl^- at the MCl_x cathode, where M = {Ag, Pb, Cu, Ni, Fe, Cr}. This configuration achieves high rate capability by all together avoiding diffusion of Mg^{2+} in a host material. The relatively large and monovalent Cl^- ion diffuses much faster than Mg^{2+}. In particular, AgCl showed low solubility in THF and offered an initial capacity of 178 mA h g^{-1}, which represents ~95% of the theoretical capacity, and operated at ~2.0 V. Dissolution of the cathode caused the capacity to quickly faded below 100 mA h g^{-1} within 10 cycles. However, it is notable that a capacity of 104 mA h g^{-1} was possible at a 10 C discharge rate, and a low but stable capacity of ~40 mA h g^{-1} was observed at this rate even after 200 cycles.

(v) Magnesium-sulfur (Mg/S). As with Li/S batteries, Mg/S batteries have a high theoretical energy density and no solid state diffusion. Sulfur boasts capacities of 1671 mA h g^{-1} and 3459 mA h cm^{-3}, and at the cell level Mg/S batteries are projected to have energy densities in excess of 4 kWh L^{-1} [234]. However, Mg/S has been much less studied since it has the same problems as Li/S (e.g., dissolution of sulfur) with the additional challenge of the electrophilic sulfur cathode reacting with nucleophilic Mg-compatible electrolytes. Kim *et al.* [234] reported the first Mg/S battery after identifying an appropriate electrolyte. A non-nucleophilic salt (hexamethyldisilazide magnesium chloride, HMDS-MgCl) was prepared in a 3:1 ratio with $AlCl_3$ and then crystallized for use in the electrolyte. This electrolyte showed anodic stability up to 3.2 V with a Pt working electrode. A discharge capacity of 1200 mA h g^{-1} was observed after the first cycle, but immediately fell to 394 mA h g^{-1} after the second cycle. Problems with self-discharge and polysulfide dissolution still need to be addressed, but this report was a big first step towards Mg/S batteries.

Building on this development, Zhao-Karger *et al.* [279] reported an efficient one-pot synthesis of the electroactive material in the Mg-HMDS electrolyte. They also improved the cell voltage to 1.65 V (compared to 1.77 V in theory, and less than 1 V published by Kim *et al.* [234]) when a glyme/ionic liquid mixture was used as the electrolyte solvent and a sulfur-carbon composite was used as the cathode. The initial capacity was 800 mA h g^{-1}, but still suffered from rapid fading. Nevertheless, it highlighted the beneficial effects that appropriate solvents and composites may have on Mg/S battery performance.

Experimental design for MIB cathode research

For the most part, the material performance summarized here has been taken at face value. However, a more critical view reveals a large number of discrepancies in magnesium battery literature. A number of studies on the MIB electrolytes [98,280] and their compatibility with Mg [109,281] and current collectors [111,282–286] conflict with the experimental protocol reported in a significant fraction of publications on MIB cathodes. Presumably, these experimental protocols have been designed on the implicit assumption that the setups used in LIB research carries over to MIB studies. However, this is demonstratively untrue in the case of electrolyte and cathode material performance, and should not be assumed in the case of any other component of an MIB cell. Here we discuss the alternatives to certain procedural pitfalls that have plagued the literature.

Electrolyte

The dearth of robust MIB electrolytes has long hampered the search for high-voltage cathode materials. For convenience, electrolytes such as $Mg(ClO_4)_2$ in AN or PC have often been substituted to study electrochemistry at the cathode. However, the high charge density of Mg^{2+} leads to large de-solvation energies at the cathode (roughly 3 times larger than for Li^+) [209]. As a consequence, the choice of Mg electrolyte will have a much more significant impact on the performance of the cathode. For example, while excellent cycling performance is observed for Chevrel phase materials in $Mg(AlCl_2BuEt)_2$/THF, fundamentally poorer behavior is observed for the same cathode in $Mg(ClO_4)_2$/AN, and no insertion at all occurs when the solvent is PC [120]. At the anode, AN does not appear to support reversible magnesium electrochemistry, as it decomposes at −0.2 V rather than plate magnesium [281]. Further, water in the electrolyte has been long known as crucial to improving electrode capacity [116,229], while other additives like LiCl boost ionic conductivity [287]. As such, cathode performance may be artificially limited by the electrolyte, as opposed to the cathode material itself. While this was unavoidable in the past, a number of new Mg-compatible electrolytes have been developed which have voltage windows that approach 4 V or more [104,107,112,113,284]. Since the electrolytes often used to date are suboptimal for both the cathode and the anode, it is reasonable to start examining the cathode/electrolyte compatibility of systems that are more likely to enable practical magnesium batteries.

Counter and reference electrodes

Another related issue that has long been reported is the passivation of Mg in most conventional salts and solvents [97,109]. However, the severity and rate of passivation is not entirely clear, as many studies report reversible (albeit limited) electrochemistry using this combination of anode and electrolyte. Again, it may be the case that such studies show the results of limitations on the electrochemical system and not the cathode alone. Although this possibility is not often addressed, results published by Liang *et al.* [161] support this hypothesis. By nanosizing both the MoS_2 cathode material and the Mg anode, nearly twice the capacity was obtained compared to the cases where only the cathode material particle size was reduced (Fig. 13). However, having said this, the cells were charged up to 3 V, which is beyond the stability window of the electrolyte, $Mg(AlCl_3Bu)_2$, (~2.5 V [280]), and the Cu and Al current collectors (<1.8 V [111]). It has been suggested that at low current densities, the anode will not be fully passivated by the formation of surface films [243]. Nevertheless, even in the case where the Mg anode is not totally passivated (and thus still usable as a counter electrode), it should be understood as a quasi-reference electrode. Native surface films will be present on Mg even after polishing the metal in a glove box [109], and additional films (of varying thickness and resistivity) are expected to grow after immersion in the electrolyte. If that electrolyte passivates Mg, then the potential of the reference electrode is no longer governed by the reversible Mg/Mg^{2+} couple, but by the potential of whatever surface films form. When this has been taken into consideration, the voltage of a Mg metal quasi-reference electrode has been consistently more positive than the reversible Mg/Mg^{2+} redox couple by 0.5–0.7 V [109,270,288]. Hence, the discharge voltages measured at the cathode are significantly lower than the equilibrium potential, which may partially explain the difference between experimental and theoretical voltages obtained in some cases. This is yet another situation where the design of the experimental setup adversely affects the observed cathode energy densities. To avoid this issue, silver-ion and activated carbon electrodes can serve as reference electrodes in nonaqueous three-electrode experiments [201,232,289–291], and similarly activated carbon can serve as readily available alternatives for the counter electrode [201,232].

Current collectors

Lastly, the current collector has often been overlooked. Corrosion of current collectors in LIBs is a known issue that affects long-term functionality and safety [292,293]. While Cu or Al foil are popular choices for LIB research, it has been shown that both corrode at relatively low potentials in $Mg(AlCl_2BuEt)_2$/THF (no greater than 1.8 and 1.2 V, respectively) [111,286]. This shows that the usable voltage window for electrolytes is also dependent on the current collector. Similar results were obtained for Ni and stainless steel, which are stable up to ~2.1 V [282], but chloride-containing electrolytes have been identified as corrosive to non-noble metals, which is problematic for battery components like SS casings [110]. Dissolution of the current collector can interfere with the intended electrochemical response in CV studies, as the observed corrosion current looks the same as intercalation at the same potential. To get around this issue, several ideas have been proposed. A bisimide electrolyte has been shown to inhibit corrosion on a number of different substrates, and Mo and W form passivation layers that showed stability up to 2.8 V [283,284]. Another study showed Pt and glassy carbon show good stability (up to at least 3 V in 0.50 mol L^{-1} PhMgCl/0.25 mol L^{-1} $AlCl_3$/THF), which is useful for basic scientific studies, but not for commercial applications [285]. However, glassy carbon coatings formed via plasma carburization inhibited pitting corrosion on different metal electrodes when polarized at 4 V. Additionally, carbon cloth or carbon paper demonstrates high stability beyond most metals, and makes for a convenient low-cost current collector [104,282,294].

Searching through the MIB cathode literature reveals a slew of inconsistencies. These issues include operating the cells outside the voltage stability window of the electrolyte, charging cathode current collectors above their dissolution potential, and using Mg as an electrode in passivating electrolytes. These various effects cast some doubt on the veracity or reproducibility of some MIB studies, while in other cases substandard design options may curtail the performance of ostensibly underachieving materials. In both cases, the field benefits from adopting self-consistent experimental protocols as outlined here.

Perspectives

The toolbox for improving performance for the various cathode materials borrows from common LIB strategies such as cation or anion doping, tailoring the nanostructure to increase the active material surface area, and carbon coating. In addition, screening the Mg^{2+} charge with water in the lattice or electrolyte has been particularly effective for improving performance in MnO_2 and V_2O_5. Further, tuning the interlayer spacing should prove to be an effective method to reduce Coulombic interactions between Mg^{2+} and the matrix. An understanding of the electronic structure of materials has not been as appreciated as the crystal structure, but should also prove important, as the ability to delocalize charge and change valence states is crucial for the fast transport, as observed most notably in Chevrel phase materials. Computational studies have limitations, but should prove to be a powerful asset to screen prospective materials and help elucidate trends in properties.

A healthy appreciation for the nuances of magnesium electrochemistry will be important to improve on cathodes that thus far demonstrate limited capacity or energy density. The tools of the electrochemist (cyclic voltammetry, galvanostatic cycling, impedance spectroscopy, etc.) can then be connected with microscopy and spectroscopy techniques to uncover novel reaction mechanisms and design the cathodes for next-generation batteries.

CONCLUDING REMARKS

Sodium and magnesium batteries are among the most compelling alternatives to Li-ion batteries. Both have advantages in terms of safety and resource abundance. Efforts to develop NIBs are predicated on cost reduction relative to Li cells, whereas magnesium has the possibility of higher capacities by virtue of the divalent ion. Both are far less explored than the technologically mature Li-ion battery, but have drawn considerable interest as we begin to approach the limits of LIB energy density.

Sodium benefits from familiar electrochemical properties, and Na-containing analogs to LIB electrolytes and insertion hosts generally show similar behavior. However, a major difference is ion size. The larger Na^+ ion inflicts greater strain on the host lattice, leading to pulverization during cycling. Techniques to mitigate this effect are crucial to long-term performance. On the other hand, magnesium electrochemistry differs dramatically from that of lithium. The divalent atom exerts greater electrostatic forces that generally slow solid-state Mg diffusion to a crawl, and the search for suitable Mg-compatible electrolytes has been more arduous.

The rapidly growing field of MIB research has seen significant advances in the past 15 years. Enabled by early breakthroughs by Aurbach in 2000 and more recent electrolyte advances, the search for high performance MIB cathode materials is poised for future breakthroughs. While Chevrel phase materials are so far been the most successful cathode material developed, other materials such as MnO_2 and $MgFeSiO_4$ are strong candidates for future generations of magnesium batteries.

Received 6 September 2015; accepted 15 September 2015

1 IEA. Fossil-fuel subsidies, in: World Energy Outlook 2014. Paris: IEA, 2014: 313

2 US Energy Information Administration, International Energy Outlook 2013 with Projections to 2040. Washington, DC, 2013. http://www.eia.gov/forecasts/ieo/pdf/0484(2013).pdf

3 REN21. Policy Landscape, in: Renewables 2014 Global Status Report. Paris: REN21 Secretariat, 2014: 75–91. http://www.ren21.net/status-of-renewables/global-status-report/

4 Erickson EM, Ghanty C, Aurbach D. New horizons for conventional lithium ion battery technology. J Phys Chem Lett, 2014, 5: 3313–3324

5 Wang Y, Liu B, Li Q, *et al.* Lithium and lithium ion batteries for applications in microelectronic devices: a review. J Power Sources, 2015, 286: 330–345

6 Nykvist B, Nilsson M. Rapidly falling costs of battery packs for electric vehicles. Nat Clim Change, 2015, 5: 329–332

7 Sathiya M, Abakumov AM, Foix D, *et al.* Origin of voltage decay in high-capacity layered oxide electrodes. Nat Mater, 2015, 14: 230–238

8 Sakti A, Michalek JJ, Fuchs ERH, Whitacre JF. A techno-economic analysis and optimization of Li-ion batteries for light-duty passenger vehicle electrification. J Power Sources, 2015, 273: 966–980

9 Yoo HD, Markevich E, Salitra G, Sharon D, Aurbach D. On the challenge of developing advanced technologies for electrochemical energy storage and conversion. Mater Today, 2014, 17: 110–121

10 Augustyn V, Come J, Lowe MA, *et al.* High-rate electrochemical energy storage through Li^+ intercalation pseudocapacitance. Nat Mater, 2013, 12: 518–522

11 Bruce PG, Scrosati B, Tarascon JM. Nanomaterials for rechargeable lithium batteries. Angew Chem Int Ed, 2008, 47: 2930–2946

12 Zhang WJ. A review of the electrochemical performance of alloy anodes for lithium-ion batteries. J Power Sources, 2011, 196: 13–24

13 Park CM, Kim JH, Kim H, Sohn HJ. Li-alloy based anode materials for Li secondary batteries. Chem Soc Rev, 2010, 39: 3115–3141

14 Cabana J, Monconduit L, Larcher D, Palacín MR. Beyond intercalation-based Li-ion batteries: the state of the art and challenges of electrode materials reacting through conversion reactions. Adv Mater, 2010, 22: 170–192

15 Armstrong AR, Bruce PG. Synthesis of layered $LiMnO_2$ as an electrode for rechargeable lithium batteries. Nature, 1996, 381: 499–500

16 Mizushima K, Jones PC, Wiseman PJ, Goodenough JB. Li_xCoO_2 $(0<x\leqslant1)$: a new cathode material for batteries of high energy density. Mater Res Bull, 1980, 15: 783–789

17 Whittingham MS. Electrical energy storage and intercalation chemistry. Science, 1976, 192: 1126–1127

18 Goodenough JBB, Kim Y. Challenges for rechargeable Li batteries. Chem Mater, 2010, 22: 587–603

19 Goodenough JBB, Park KSS. The Li-ion rechargeable battery: a perspective. J Am Chem Soc, 2013, 165: 1167–1176

20 Etacheri V, Marom R, Elazari R, Salitra G, Aurbach D. Challenges in the development of advanced Li-ion batteries: a review. Energy Environ Sci, 2011, 4: 3243–3262

21 Guo YG, Hu JS, Wan LJ. Nanostructured materials for electrochemical energy conversion and storage devices. Adv Mater, 2008, 20: 2878–2887

22 Scrosati B, Garche J. Lithium batteries: status, prospects and future. J Power Sources, 2010, 195: 2419–2430

23 Palomares V, Serras P, Villaluenga I, *et al*. Na-ion batteries, recent advances and present challenges to become low cost energy storage systems. Energy Environ Sci, 2012, 5: 5884–5901

24 Kim SW, Seo DH, Ma X, Ceder G, Kang K. Electrode materials for rechargeable sodium-ion batteries: potential alternatives to current lithium-ion batteries. Adv Energy Mater, 2012, 2: 710–721

25 Ellis BL, Nazar LF. Sodium and sodium-ion energy storage batteries. Curr Opin Solid State Mater Sci, 2012, 16: 168–177

26 Huie MM, Bock DC, Takeuchi ES, Marschilok AC, Takeuchi KJ. Cathode materials for magnesium and magnesium-ion based batteries. Coord Chem Rev, 2015, 287: 15–27

27 Muldoon J, Bucur CB, Gregory T. Quest for nonaqueous multivalent secondary batteries: magnesium and beyond. Chem Rev, 2014, 114: 11683–11720

28 Haynes WM. CRC Handbook of Chemistry and Physics, 93rd Edition. Boca Raton: Taylor & Francis, 2012

29 Shannon RD. Revised effective ionic radii and systematic studies of interatomie distances in halides and chaleogenides, Acta Cryst, 1976, 32; 751–767

30 Slater MD, Kim D, Lee E, Johnson CS, Sodium-ion batteries. Adv Funct Mater, 2013, 23: 947–958

31 Mohtadi R, Mizuno F. Magnesium batteries: current state of the art, issues and future perspectives. Beilstein J Nanotech, 2014. 5: 1291–311

32 Shterenberg I, Salama M, Gofer Y, Levi E, Aurbach D. The challenge of developing rechargeable magnesium batteries. MRS Bull, 2014, 39: 453–460

33 Islam MS, Fisher CAJ. Lithium and sodium battery cathode materials: computational insights into voltage, diffusion and nanostructural properties. Chem Soc Rev, 2014, 43: 185–204

34 Haxel GB, Hedrick JB, Orris GJ. Rare earth elements: critical resources for high technology. Reston: US Geological Survey, 2002. http://pubs.usgs.gov/fs/2002/fs087-02

35 US Geological Survey. Mineral Commodity Summaries 2015, Reston: US Geological Survey, 2015.

36 Zu CX, Li H. Thermodynamic analysis on energy densities of batteries. Energy Environ Sci, 201, 41: 2614–2624

37 Yabuuchi N, Kubota K, Dahbi M, Komaba S. Research development on sodium-ion batteries. Chem Rev, 2014, 114: 11636–11682

38 Mikkor M. Graphite aluminum- and silicon carbide-coated current collectors for sodium-sulfur cells. J Electrochem Soc, 1985, 132: 991–998

39 Hudak N, Huber D. Nanostructured lithium-aluminum alloy electrodes for lithium-ion batteries. ECS Trans, 2011, 33: 1–13

40 Ong SP, Chevrier VL, Hautier G, *et al*. Voltage, stability and diffusion barrier differences between sodium-ion and lithium-ion intercalation materials. Energy Environ Sci, 2011, 4: 3680–3688

41 Kim Y, Park Y, Choi A, *et al*. An amorphous red phosphorus/carbon composite as a promising anode material for sodium ion batteries. Adv Mater, 2013, 25: 3045–3049

42 Xiong H, Slater MD, Balasubramanian M, Johnson CS, Rajh T. Amorphous TiO_2 nanotube anode for rechargeable sodium ion batteries. J Phys Chem Lett, 2011, 2: 2560–2565

43 Bernhart W, Kruger FJ. Technology & Market Drivers for Stationary and Automotive Battery Systems. Nice: Roland Berger Strategy Consultants, 2012 http://www.rechargebatteries.org/wp-content/uploads/2013/04/Batteries-2012-Roland-Berger-Report1.pdf

44 Uchaker E, Zheng YZ, Li S, *et al*. Better than crystalline: amorphous vanadium oxide for sodium-ion batteries. J Mater Chem A, 2014, 2: 18208–18214

45 Wei Q, Liu J, Feng W, *et al*. Hydrated vanadium pentoxide with superior sodium storage capacity. J Mater Chem A, 2015, 3: 8070–8075

46 Wang Y, Takahashi K, Lee K, Cao G. Nanostructured vanadium oxide electrodes for enhanced lithium-ion intercalation. Adv Funct Mater, 2006, 16: 1133–1144

47 Wang Y, Shang H, Chou T, Cao G. Effects of thermal annealing on the Li^+ intercalation properties of $V_2O_5{\cdot}nH_2O$ xerogel films. J Phys Chem B, 2005, 109: 11361–11366

48 Nam KW, Kim S, Yang E, *et al*. Critical role of crystal water for a layered cathode material in sodium ion batteries. Chem Mater, 2015, 27: 3721–3725

49 Yabuuchi N, Komaba S. Recent research progress on iron- and manganese-based positive electrode materials for rechargeable sodium batteries. Sci Technol Adv Mater, 2014, 15: 043501

50 Mo Y, Ong SP, Ceder G. Insights into diffusion mechanisms in P2 layered oxide materials by first-principles calculations. Chem Mater, 2014, 26: 5208–5214

51 Han SC, Lim H, Jeong J, *et al*. Ca-doped Na_xCoO_2 for improved cyclability in sodium ion batteries. J Power Sources, 2015, 277: 9–16

52 Roger M, Morris DJP, Tennant DA, *et al*. Patterning of sodium ions and the control of electrons in sodium cobaltate. Nature, 2007, 445: 631–634

53 Zandbergen HW, Foo M, Xu Q, Kumar V, Cava RJ. Sodium ion ordering in Na_xCoO_2: electron diffraction study. Phys Rev B, 2004, 70: 1–8

54 Lei Y, Li X, Liu L, Ceder G. Synthesis and stoichiometry of different layered sodium cobalt oxides. Chem mater, 2014, 26: 5288–5296

55 Shibata T, Fukuzumi Y, Kobayashi W, Moritomo Y. Fast discharge process of layered cobalt oxides due to high Na^+ diffusion. Sci Rep, 2015, 5: 9006

56 Hasa I, Buchholz D, Passerini S, Hassoun J. A comparative study of layered transition metal oxide cathodes for application in sodium-ion battery. ACS Appl Mater Interfaces, 2015, 7: 5206–5212

57 Noh HJ, Youn S, Yoon CS, Sun YK. Comparison of the structural and electrochemical properties of layered $Li[Ni_xCo_yMn_z]O_2$ (x = 1/3, 0.5, 0.6, 0.7, 0.8 and 0.85) cathode material for lithium-ion batteries. J Power Sources, 2013, 233: 121–130

58 Saadoune I, Delmas C. On the $Li_xNi_{0.8}Co_{0.2}O_2$ System. J Solid State Chem, 1998, 136: 8–15

59 Hwang JY, Oh SM, Myung ST, *et al*. Radially aligned hierarchical columnar structure as a cathode material for high energy density sodium-ion batteries. Nat Commun, 2015, 6: 6865

60 Shu GJ, Chou FC. Sodium-ion diffusion and ordering in single-crystal P2 -Na_xCoO_2. Phys Rev B, 2008, 78: 3–6

61 Medarde M, Mena M, Gavilano JL, *et al*. 1D to 2D Na^+ ion diffusion inherently linked to structural transitions in $Na_{0.7}CoO_2$. Phys Rev

Lett, 2013, 110: 1–5

62 Wang Y, Xiao R, Hu YS, Avdeev M, Chen L. P2-$Na_{0.6}[Cr_{0.6}Ti_{0.4}]O_2$ cation-disordered electrode for high-rate symmetric rechargeable sodium-ion batteries. Nat Commun, 2015, 6: 6954

63 Casas-Cabanas M, Roddatis V, Saurel D, *et al*. Crystal chemistry of Na insertion/deinsertion in $FePO_4$-$NaFePO_4$. J Mater Chem, 2012, 22: 17421–17423

64 Oh SM, Myung ST, Hassoun J, Scrosati B, Sun YK. Reversible $NaFePO_4$ electrode for sodium secondary batteries. Electrochem Commun, 201, 22 2: 149–152

65 Kim J, Seo DH, Kim H, *et al*. Unexpected discovery of low-cost maricite $NaFePO_4$ as a high-performance electrode for Na-ion batteries. Energy Environ Sci, 2015, 8: 540–545

66 Lee YJ, Yi H, Kim WJ, *et al*. Fabricating genetically engineered high-power lithium-ion batteries using multiple virus genes, Science, 2009, 324: 1051–1055

67 Kim SW, Ryu J, Park CB, Kang K. Carbon nanotube-amorphous $FePO_4$ core-shell nanowires as cathode material for Li ion batteries. Chem Commun, 2010, 46: 7409–7411

68 Ha KH, Woo SH, Mok D, *et al*. $Na_{4-\alpha}M_{2+\alpha/2}(P_2O_7)_2$ ($2/3 \le \alpha \le 7/8$, M = Fe, $Fe_{0.5}Mn_{0.5}$, Mn): a promising sodium ion cathode for Na-ion batteries. Adv Energy Mater, 2013, 3: 770–776

69 Kundu D, Tripathi R, Popov G, Makahnouk WRM, Nazar LF. Synthesis, structure, and Na-ion migration in $Na_4NiP_2O_7F_2$: a prospective high voltage positive electrode material for the Na-ion batter. Chem Mater, 2015, 27: 885–891

70 Barpanda P, Oyama G, Nishimura SI, Chung SC, Yamada A. A 3.8-V earth-abundant sodium battery electrode. Nat Commun, 2014, 5: 4358

71 Saha P, Jampani PH, Datta MK, *et al*. Electrochemical performance of chemically and solid state-derived Chevrel phase Mo_6T_8(T = S, Se) positive electrodes for sodium-ion batteries. J Phys Chem C, 2015, 119: 5771–5782

72 Cao Y, Xiao L, Sushko ML, *et al*. Sodium ion insertion in hollow carbon nanowires for battery applications. Nano Lett, 2012, 12: 3783–3787

73 Stevens DA, Dahn JR. The mechanisms of lithium and sodium insertion in carbon materials. J Electrochem Soc, 2001, 148: A803–A811

74 Datta D, Li J, Shenoy VB. Defective graphene as promising anode material for Na-ion battery and Ca-ion batteries. ACS Appl Mater Interfaces, 2014, 6: 1788–1795

75 Zhou LJ, Hou ZF, Wu LM, Zhang YF. First-principles studies of lithium adsorption and diffusion on graphene with grain boundaries. J Phys Chem C, 2014, 118: 28055–28062

76 Datta D, Li J, Koratkar N, Shenoy VB. Enhanced lithiation in defective graphene. Carbon, 2014, 80: 305–310

77 Pramudita JC, Pontiroli D, Magnani G, *et al*. Graphene and selected derivatives as negative electrodes in sodium- and lithium-ion batteries. ChemElectroChem, 2015, 2: 600–610

78 Wen Y, He K, Zhu Y, *et al*. Expanded graphite as superior anode for sodium-ion batteries. Nat Commun, 2014, 5: 4033

79 Tsai P, Chung SC, Lin S, Yamada A. *Ab initio* study of sodium intercalation into disordered carbon. J Mater Chem A, 2015, 3: 9763–9768

80 Malyi OI, Sopiha K, Kulish VV, *et al*. A computational study of Na behavior on graphene. Appl Surf Sci, 2015, 333: 235–243

81 Xu J, Wang M, Wickramaratne NP, *et al*. High-performance sodium ion batteries based on three-dimensional anode from nitrogen-doped graphene foams. Adv Mater, 2015, 27: 2042–2048

82 Kim KT, Ali G, Chung KY, *et al*. Anatase titania nanorods as an intercalation anode material for rechargeable sodium batteries. Nano Lett, 2014, 14: 416–422

83 Wu L, Bresser D, Buchholz D, *et al*. Unfolding the mechanism of sodium insertion in anatase TiO_2 nanoparticles. Adv Energy Mater, 2015, doi: 10.1002/aenm.201401142

84 Cha HA, Jeong HM, Kang JK. Nitrogen-doped open pore channeled graphene facilitating electrochemical performance of TiO_2 nanoparticles as an anode material for sodium ion batteries. J Mater Chem A, 2014, 2: 5182–5186

85 Gonzalez JR, Alcantara R, Nacimiento F, Ortiz GF, Tirado JL. Microstructure of the epitaxial film of anatase nanotubes obtained at high voltage and the mechanism of its electrochemical reaction with sodium. CrystEngComm, 2014, 16: 4602–4609

86 Legrain F, Malyi O, Manzhos S. Insertion energetics of lithium, sodium, and magnesium in crystalline and amorphous titanium dioxide: a comparative first-principles study. J Power Sources, 2015, 278: 197–202

87 Usui H, Yoshioka S, Wasada K, Shimizu M, Sakaguchi H. Nb-doped rutile TiO_2 : a potential anode material for Na-ion battery. ACS Appl Mater Interfaces, 2015, 7: 6567–6573

88 Darwiche A, Toiron M, Sougrati MT, *et al*. Performance and mechanism of $FeSb_2$ as negative electrode for Na-ion batteries. J Power Sources, 2015, 280: 588–592

89 Wu D, Li X, Xu B, *et al*. $NaTiO_2$: a layered anode material for sodium-ion batteries. Energy Environ Sci, 2015, 8: 195–202

90 Chen C, Wen Y, Hu X, *et al*. Na^+ intercalation pseudocapacitance in graphene-coupled titanium oxide enabling ultra-fast sodium storage and long-term cycling. Nat Commun, 2015, 6: 6929

91 Sun Y, Zhao L, Pan H, *et al*. Direct atomic-scale confirmation of three-phase storage mechanism in $Li_4Ti_5O_{12}$ anodes for room-temperature sodium-ion batteries. Nat Commun, 2013, 4: 1870

92 Wang Y, Yu X, Xu S, *et al*. A zero-strain layered metal oxide as the negative electrode for long-life sodium-ion batteries. Nat Commun, 2013, 4: 2365

93 Wang Y, Liu J, Lee B, *et al*. Ti-substituted tunnel-type $Na_{0.44}MnO_2$ oxide as a negative electrode for aqueous sodium-ion batteries. Nat Commun, 2015, 6: 6401

94 Qian J, Wu X, Cao Y, Ai X, Yang H. High capacity and rate capability of amorphous phosphorus for sodium ion batteries. Angew Chem Int Ed, 2013, 52: 4633–4636

95 Hembram KPSS, Jung H, Yeo BC, *et al*. Unraveling the atomistic sodiation mechanism of black phosphorus for sodium ion batteries by first-principles calculations. J Phys Chem C, 2015, 119: 15041–15046

96 Wang C, Xu Y, Fang Y, *et al*. Extended π-conjugated system for fast-charge and -discharge sodium-ion batteries. J Am Chem Soc, 2015, 137: 3124–3130

97 Gregory TD, Hoffman RJ, Winterton RC. Nonaqueous electrochemistry of magnesium. J Electrochem Soc, 1990, 137: 775–780

98 Aurbach D, Lu Z, Schechter A, *et al*. Prototype systems for rechargeable magnesium batteries. Nature, 2000, 407: 724–727

99 Novák P, Imhof R, Haas O. Magnesium insertion electrodes for rechargeable nonaqueous batteries—a competitive alternative to lithium? Electrochim Acta, 1999, 45: 351–367

100 Aurbach D, Weissman I, Gofer Y, Levi E. Nonaqueous magnesium electrochemistry and its application in secondary batteries. Chem Rec, 2003, 3: 61–73

101 Yuan H, Jiao L, Cao J, *et al*. Development of magnesium-insertion positive electrode for rechargeable magnesium batteries. J Mater Sci Technol, 2004, 20: 41–45

102 Levi E, Levi MD, Chasid O, Aurbach D. A review on the problems of the solid state ions diffusion in cathodes for rechargeable Mg batteries. J Electroceramics, 2009, 22: 13–19

103 Levi E, Gofer Y, Aurbach D. On the way to rechargeable Mg batteries: the challenge of new cathode materials. Chem Mater, 2010,

22: 860–868

104 Muldoon J, Bucur CB, Oliver AG, *et al*. Electrolyte roadblocks to a magnesium rechargeable battery. Energy Environ Sci, 2012, 5: 5941–5950

105 Yoo HD, Shterenberg I, Gofer Y, *et al*. Mg rechargeable batteries: an on-going challenge. Energy Environ Sci, 2013, 6: 2265–2279

106 Saha P, Datta MK, Velikokhatnyi OI, *et al*. Rechargeable magnesium battery: current status and key challenges for the future. Prog Mater Sci, 2014, 66: 1–86

107 Tutusaus O, Mohtadi R. Paving the way towards highly stable and practical electrolytes for rechargeable magnesium batteries. ChemElectroChem, 2015, 2: 51–57

108 Park MS, Kim JG, Kim YJ, Choi NS, Kim JS. Recent advances in rechargeable magnesium battery technology: a review of the field's current status and prospects. Isr J Chem, 2015, 55: 570–585

109 Lu Z, Schechter A, Moshkovich M, Aurbach D. On the electrochemical behavior of magnesium electrodes in polar aprotic electrolyte solutions. J Electroanal Chem, 1999, 466: 203–217

110 Muldoon J, Bucur CB, Oliver AG, *et al*. Corrosion of magnesium electrolytes: chlorides – the culprit. Energy Environ Sci, 2013, 6: 482–487

111 Lv D, Xu T, Saha P, *et al*. A scientific study of current collectors for Mg batteries in $Mg(AlCl_2EtBu)_2$/THF electrolyte. J Electrochem Soc, 2012, 160: A351–A355

112 Nelson EG, Brody SI, Kampf JW, Bartlett BM. A magnesium tetraphenylaluminate battery electrolyte exhibits a wide electrochemical potential window and reduces stainless steel corrosion. J Mater Chem A, 2014, 2: 18194–18198

113 Tutusaus O, Mohtadi R, Arthur TS, *et al*. An efficient halogen-free electrolyte for use in rechargeable magnesium batteries. Angew Chem Int Ed, 2015, 54: 7900–7904

114 Guo Y, Zhang F, Yang J, *et al*. Boron-based electrolyte solutions with wide electrochemical windows for rechargeable magnesium batteries. Energy Environ Sci, 2012, 5: 9100–9106

115 Amatucci GG, Badway F, Singhal A, *et al*. Investigation of yttrium and polyvalent ion intercalation into nanocrystalline vanadium oxide. J Electrochem Soc, 2001, 148: A940–A950

116 Novák P. Electrochemical insertion of magnesium in metal oxides and sulfides from aprotic electrolytes. J Electrochem Soc, 1993, 140: 140–144

117 Levi E, Gershinsky G, Aurbach D, Isnard O, Ceder G. New insight on the unusually high ionic mobility in Chevrel phases. Chem Mater, 2009, 21: 1390–1399

118 Aurbach D, Gofer Y, Lu Z, *et al*. A short review on the comparison between Li battery systems and rechargeable magnesium battery technology. J Power Sources, 2001, 97-98: 28–32

119 Kapustinskii AF. Lattice energy of ionic crystals. Q Rev Chem Soc, 1956, 10: 283–294

120 Levi MD, Lancry E, Gizbar H, *et al*. Kinetic and thermodynamic studies of Mg^{2+} and Li^+ ion insertion into the Mo_6S_8 Chevrel phase. J Electrochem Soc, 2004, 151: A1044–A1051

121 Tao ZL, Xu LN, Gou XL, Chen J, Yuan HT. TiS_2 nanotubes as the cathode materials of Mg-ion batteries. Chem Commun, 2004: 2080–2081

122 Ling C, Banerjee D, Song W, Zhang M, Matsui M. First-principles study of the magnesiation of olivines: redox reaction mechanism, electrochemical and thermodynamic properties. J Mater Chem, 2012, 22: 13517–13523

123 Liu M, Rong Z, Malik R, *et al*. Spinel compounds as multivalent battery cathodes: a systematic evaluation based on *ab initio* calculations. Energy Environ Sci, 2014, 8: 964–974

124 Aurbach D, Cohen Y, Moshkovich M. The study of reversible magnesium deposition by *in situ* scanning tunneling microscopy. Electrochem Solid State Lett, 2001, 4: A113–A116

125 Matsui M. Study on electrochemically deposited Mg metal. J Power Sources, 2011, 196: 7048–7055

126 Ling C, Banerjee D, Matsui M. Study of the electrochemical deposition of Mg in the atomic level: why it prefers the non-dendritic morphology. Electrochim Acta, 2012, 76: 270–274

127 Levi E, Gofer Y, Vestfreed Y, Lancry E, Aurbach D. $Cu_2Mo_6S_8$ Chevrel phase, a promising cathode material for new rechargeable Mg batteries: a mechanically induced chemical reaction. Chem Mater, 2002, 14: 2767–2773

128 Besenhard JO, Winter M. Advances in battery technology: rechargeable magnesium batteries and novel negative-electrode materials for lithium ion batteries. ChemPhysChem, 2002, 3: 155–159

129 Kganyago KR, Ngoepe PE, Catlow CRA. Voltage profile, structural prediction, and electronic calculations for $Mg_xMo_6S_8$. Phys Rev B, 2003, 67: 1–10

130 Levi MD, Gizbar H, Lancry E, *et al*. A comparative study of Mg^{2+} and Li^+ ion insertions into the Mo_6S_8 Chevrel phase using electrochemical impedance spectroscopy. J Electroanal Chem, 2004, 569: 211–223

131 Lancry E, Levi E, Gofer Y, *et al*. Leaching chemistry and the performance of the Mo_6S_8 cathodes in rechargeable Mg batteries. Chem Mater, 2004, 16: 2832–2838

132 Lancry E, Levi E, Gofer Y, Levi MD, Aurbach D. The effect of milling on the performance of a Mo_6S_8 Chevrel phase as a cathode material for rechargeable Mg batteries. J Solid State Electrochem, 2005, 9: 259–266

133 Levi MD, Aurbach D. A comparison between intercalation of Li and Mg ions into the model Chevrel phase compound ($M_xMo_6S_8$): impedance spectroscopic studies. J Power Sources, 2005, 146: 349–354

134 Levi MD, Lancri E, Levi E, *et al*. The effect of the anionic framework of Mo_6X_8 Chevrel Phase (X = S, Se) on the thermodynamics and the kinetics of the electrochemical insertion of Mg^{2+} ions. Solid State Ionics, 2005, 176: 1695–1699

135 Levi E, Lancry E, Gofer Y, Aurbach D. The crystal structure of the inorganic surface films formed on Mg and Li intercalation compounds and the electrode performance. J Solid State Electrochem, 2006, 10: 176–184

136 Lancry E, Levi E, Mitelman A, Malovany S, Aurbach D. Molten salt synthesis (MSS) of $Cu_2Mo_6S_8$—new way for large-scale production of Chevrel phases. J Solid State Chem, 2006, 179: 1879–1882

137 Levi E, Lancry E, Mitelman A, *et al*. Phase diagram of Mg insertion into Chevrel phases, $Mg_xMo_6T_8$ (T = S, Se). 2. The crystal structure of triclinic $MgMo_6Se_8$. Chem Mater, 2006, 18: 3705–3714

138 Levi E, Lancry E, Mitelman A, *et al*. Phase diagram of Mg insertion into Chevrel phases, $Mg_xMo_6T_8$ (T = S, Se). 1. Crystal structure of the sulfides. Chem Mater, 2006, 18: 5492–5503

139 Levi E, Mitelman A, Aurbach D, Isnard O. On the mechanism of triclinic distortion in Chevrel phase as probed by *in-situ* neutron diffraction. Inorg Chem, 2007, 46: 7528–7535

140 Mitelman A, Levi E, Lancry E, Aurbach D. On the Mg trapping mechanism in electrodes comprising Chevrel phases. ECS Trans, 2007, 3: 109–115

141 Mitelman A, Levi MD, Lancry E, Levi E, Aurbach D. New cathode materials for rechargeable Mg batteries: fast Mg ion transport and reversible copper extrusion in $Cu_yMo_6S_8$ compounds. Chem Commun, 2007: 4212–4214

142 Levi E, Mitelman A, Aurbach D, Brunelli M. Structural mechanism of the phase transitions in the Mg-Cu-Mo_6S_8 system probed by *ex situ* synchrotron X-ray diffraction. Chem Mater, 2007, 19: 5131–5142

143 Aurbach D, Suresh GS, Levi E, *et al*. Progress in rechargeable mag-

nesium battery technology. Adv Mater, 2007, 19: 4260–4267
144 Suresh GS, Levi MD, Aurbach D, Effect of chalcogen substitution in mixed $Mo_6S_{8-n}Se_n$ (n = 0, 1, 2) Chevrel phases on the thermodynamics and kinetics of reversible Mg ions insertion. Electrochim Acta, 2008, 53: 3889–3896
145 Levi E, Mitelman A, Isnard O, Brunelli M, Aurbach D. Phase diagram of Mg insertion into Chevrel phases, $Mg_xMo_6T_8$ (T = S, Se). 3. The crystal structure of triclinic $Mg_2Mo_6Se_8$. Inorg Chem, 2008, 47: 1975–1983
146 Woan KV, Scheffler RH, Bell NS, Sigmund WM. Electrospinning of nanofiber Chevrel phase materials. J Mater Chem, 2011, 21: 8537–8539
147 Gershinsky G, Haik O, Salitra G, *et al*. Ultra fast elemental synthesis of high yield copper Chevrel phase with high electrochemical performance. J Solid State Chem, 2012, 188: 50–58
148 Ryu A, Park M, Cho W, Kim JS, Kim Y. Size-controlled Chevrel Mo_6S_8 as cathode material for Mg rechargeable battery. Bull Korean Chem Soc, 2013, 34: 3033–3038
149 Ichitsubo T, Yagi S, Nakamura R, *et al*. A new aspect of Chevrel compounds as a positive electrode for magnesium battery. J Mater Chem A, 2014, 2: 14858–14866
150 Saha P, Jampani PH, Datta MK, *et al*. A convenient approach to Mo_6S_8 Chevrel phase cathode for rechargeable magnesium battery. J Electrochem Soc, 2014, 161: A593–A598
151 Taniguchi K, Yoshino T, Gu Y, Katsura Y, Takagi H. Reversible electrochemical insertion/extraction of Mg and Li Ions for orthorhombic Mo_9Se_{11} with cluster structure. J Electrochem Soc, 2014, 162: 198–202
152 Kaewmaraya T, Ramzan M, Osorio-Guillén JM, Ahuja R. Electronic structure and ionic diffusion of green battery cathode material: $Mg_2Mo_6S_8$. Solid State Ionics, 2014, 261: 17–20
153 Woo SG, Yoo JY, Cho W, *et al*. Copper incorporated $Cu_xMo_6S_8$ ($x \geq$ 1) Chevrel-phase cathode materials synthesized by chemical intercalation process for rechargeable magnesium batteries. RSC Adv, 2014, 4: 59048–59055
154 Cho W, Moon B, Woo SG, *et al*. Size effect of Chevrel $Mg_xMo_6S_8$ as cathode material for magnesium rechargeable batteries. Bull Korean Chem Soc, 2015, 36: 1209–1214
155 Choi SH, Kim JS, Woo SG, *et al*. Role of Cu in Mo_6S_8 and Cu mixture cathodes for magnesium ion batteries. ACS Appl Mater Interfaces, 2015, 7: 7016–7024
156 Doe RE, Han R, Hwang J, *et al*. Novel, electrolyte solutions comprising fully inorganic salts with high anodic stability for rechargeable magnesium batteries. Chem Commun, 2014, 50: 243–245
157 Shao Y, Liu T, Li G, *et al*. Coordination chemistry in magnesium battery electrolytes: how ligands affect their performance. Sci Rep, 2013, 3: 3130
158 Mohtadi R, Matsui M, Arthur TS, Hwang SJ. Magnesium borohydride: from hydrogen storage to magnesium battery. Angew Chem Int Ed, 2012, 51: 9780–9783
159 Zhu J, Guo Y, Yang J, *et al*. Halogen-free boron based electrolyte solution for rechargeable magnesium batteries. J Power Sources, 2014, 248: 690–694
160 Amir N, Vestfrid Y, Chusid O, Gofer Y, Aurbach D. Progress in nonaqueous magnesium electrochemistry. J Power Sources, 2007, 174: 1234–1240
161 Liang Y, Feng R, Yang S, *et al*. Rechargeable Mg batteries with graphene-like MoS_2 cathode and ultrasmall Mg nanoparticle anode. Adv Mater, 2011, 23: 640–643
162 Li XL, Li YD. MoS_2 nanostructures: synthesis and electrochemical Mg^{2+} intercalation. J Phys Chem B , 2004, 108: 13893–13900
163 Liu Y, Jiao L, Wu Q, *et al*. Sandwich-structured graphene-like MoS_2/C microspheres for rechargeable Mg batteries. J Mater Chem A, 2013, 1: 5822–5826
164 Liu Y, Jiao L, Wu Q, *et al*. Synthesis of rGO-supported layered MoS_2 for high-performance rechargeable Mg batteries. Nanoscale, 2013, 5: 9562–9567
165 Yang S, Li D, Zhang T, Tao Z, Chen J. First-principles study of zigzag MoS_2 nanoribbon as a promising cathode material for rechargeable Mg batteries. J Phys Chem C, 2012, 116: 1307–1312
166 Liang Y, Yoo HD, Li Y, *et al*. Interlayer-expanded molybdenum disulfide nanocomposites for electrochemical magnesium storage. Nano Lett, 2015, 15: 2194-2202
167 Hu Z, Wang L, Zhang K, *et al*. MoS_2 nanoflowers with expanded interlayers as high-performance anodes for sodium-ion batteries. Angew Chem Int Ed, 2014, 53: 12794–12798
168 Pereira AO, Miranda CR. First-principles investigation of transition metal dichalcogenide nanotubes for Li and Mg ion battery applications. J Phys Chem C, 2015, 119: 4302–4311
169 Bruce PG, Krok F, Nowinski J, Gibson VC, Tavakkoli K. Chemical intercalation of magnesium into solid hosts. J Mater Chem, 1991, 1: 705–706
170 Bruce PG, Krok F, Lightfoot P, Nowinski JL, Gibson VC. Multivalent cation intercalation. Solid State Ionics, 1992, 53-56: 351–355
171 Emly A, Van der Ven A. Mg intercalation in layered and spinel host crystal structures for Mg batteries. Inorg Chem, 2015, 54: 4394–4402
172 Gu Y, Katsura Y, Yoshino T, Takagi H, Taniguchi K. Rechargeable magnesium-ion battery based on a $TiSe_2$-cathode with d-p orbital hybridized electronic structure. Sci Rep, 2015, 5: 12486
173 Liu B, Luo T, Mu G, *et al*. Rechargeable Mg-ion batteries based on WSe_2 nanowire cathodes, ACS Nano, 2013, 7: 8051–8058
174 Tarascon JM, Wang E, Shokoohi FK, McKinnon WR, Colson S. The spinel phase of $LiMn_2O_4$ as a cathode in secondary lithium cells. J Electrochem Soc, 1991, 138: 2859–2864
175 Yuan W, Gunter JR. Insertion of bivalent cations into monoclinic NbS_3 prepared under high pressure and their secondary batteries. Solid State Ionics, 1995, 76: 253–258
176 He D, Wu D, Gao J, *et al*. Flower-like CoS with nanostructures as a new cathode-active material for rechargeable magnesium batteries. J Power Sources, 2015, 294: 643–649
177 Yu W, Wang D, Zhu B, Zhou G. Intercalation of Mg in V_2O_5. Solid State Commun, 1987, 63: 1043–1044
178 Yu W, Wang D, Zhu B, Wang S, Xue L. Insertion of bi-valence cations Mg^{2+} and Zn^{2+} into V_2O_5. Solid State Commun, 1987, 61: 271–273
179 Pereira-Ramos JP, Messina R, Perichon J. Electrochemical formation of a magnesium vanadium bronze $Mg_xV_2O_5$ in sulfone-based electrolytes at 150°C. J Electroanal Chem Interfacial Electrochem, 1987, 218: 241–249
180 Novák P, Scheifele W, Joho F, Haas O. Electrochemical insertion of magnesium into hydrated vanadium bronzes. J Electrochem Soc, 1995, 142: 2544–2550
181 Novák P, Scheifele W, Haas O. Magnesium insertion batteries—an alternative to lithium? J Power Sources, 1995, 54: 479–482
182 Shklover V, Haibach T, Ried F, Nesper R, Novák P. Crystal structure of the product of Mg^{2+} insertion into V_2O_5 single crystals. J Solid State Chem, 1996, 123: 317–323
183 Le DB, Passerini S, Coustier F, *et al*. Intercalation of polyvalent cations into V_2O_5 aerogels. Chem Mater, 1998, 4756: 682–684
184 Morita M, Yoshimoto N, Yakushiji S, Ishikawa M. Rechargeable magnesium batteries using a novel polymeric solid electrolyte. Electrochem Solid State Lett, 2001, 4: A177–A179
185 Imamura D, Miyayama M, Hibino M, Kudo T. Mg intercalation properties into V_2O_5 gel/carbon composites under high-rate condition. J Electrochem Soc, 2003, 150: A753–A758

186 Imamura D, Masaru M. Characterization of magnesium-intercalated V_2O_5/carbon composites. Solid State Ionics, 2003, 161: 173–180
187 Yoshimoto N, Yakushiji S, Ishikawa M, Morita M. Rechargeable magnesium batteries with polymeric gel electrolytes containing magnesium salts. Electrochim Acta, 2003, 48: 2317–2322
188 Yu L, Zhang X. Electrochemical insertion of magnesium ions into V_2O_5 from aprotic electrolytes with varied water content. J Colloid Interface Sci, 2004, 278: 160–165
189 Tang PE, Sakamoto JS, Baudrin E, Dunn B. V_2O_5 aerogel as a versatile host for metal ions. J Non Cryst Solids, 2004, 350: 67–72
190 Oh JS, Ko JM, Kim DW. Preparation and characterization of gel polymer electrolytes for solid state magnesium batteries. Electrochim Acta, 2004, 50: 903–906
191 Bervas M, Klein LC, Amatucci GG. Vanadium oxide–propylene carbonate composite as a host for the intercalation of polyvalent cations. Solid State Ionics, 2005, 176: 2735–2747
192 Jiao L, Yuan H, Wang Y, Cao J, Wang Y. Mg intercalation properties into open-ended vanadium oxide nanotubes. Electrochem Commun, 2005, 7: 431–436
193 Jiao L, Yuan H, Si Y, *et al*. Electrochemical insertion of magnesium in open-ended vanadium oxide nanotubes. J Power Sources, 2006, 156: 673–676
194 Jiao LF, Yuan HT, Si YC, Wang YJ, Wang YM. Synthesis of $Cu_{0.1}$-doped vanadium oxide nanotubes and their application as cathode materials for rechargeable magnesium batteries. Electrochem Commun, 2006, 8: 1041–1044
195 Hu T, Lin JB, Kong F, Mao JG. $Mg_7V_4O_{16}(OH)_2(H_2O)$: a magnesium vanadate with a novel 3D magnesium oxide open framework. Inorg Chem Commun, 2008, 11: 1012–1014
196 Stojković I, Cvjetićanin N, Marković S, Mitrić M, Mentus S. Electrochemical behaviour of V_2O_5 xerogel and V_2O_5 xerogel/C composite in an aqueous $LiNO_3$ and $Mg(NO_3)_2$ solutions. Acta Phys Polonica A, 2010, 117: 837–840
197 Pandey GP, Agrawal RC, Hashmi SA. Performance studies on composite gel polymer electrolytes for rechargeable magnesium battery application. J Phys Chem Solids, 2011, 72: 1408–1413
198 Sun JZ. Study of MgV_2O_6 as cathode material for secondary magnesium batteries. Asian J Chem, 2011, 23: 1399–1400
199 Wang Z, Su Q, Deng H. Single-layered V_2O_5 a promising cathode material for rechargeable Li and Mg ion batteries: an *ab initio* study. Phys Chem Chem Phys, 2013, 15: 8705–8709
200 Inamoto M, Kurihara H, Yajima T. Vanadium pentoxide-based composite synthesized using microwave water plasma for cathode material in rechargeable magnesium batteries. Materials, 2013, 6: 4514–4522
201 Gershinsky G, Yoo HD, Gofer Y, Aurbach D. Electrochemical and spectroscopic analysis of Mg^{2+} intercalation into thin film electrodes of layered oxides: V_2O_5 and MoO_3. Langmuir, 2013, 29: 10964–10972
202 Kim RH, Kim JS, Kim HJ, *et al*. Highly reduced VO_x nanotube cathode materials with ultra-high capacity for magnesium ion batteries. J Mater Chem A, 2014, 2: 20636–20641
203 Carrasco J. Role of van der Waals forces in thermodynamics and kinetics of layered transition metal oxide electrodes: alkali and alkaline-earth ion insertion into V_2O_5. J Phys Chem C, 2014, 118: 19599–19607
204 Lee SH, DiLeo RA, Marschilok AC, Takeuchi KJ, Takeuchi ES. Sol gel based synthesis and electrochemistry of magnesium vanadium oxide: a promising cathode material for secondary magnesium ion batteries. ECS Electrochem Lett, 2014, 3: A87–A90
205 Zhou B, Shi H, Cao R, Zhang X, Jiang Z. Theoretical study on the initial stage of magnesium battery based on V_2O_5 cathode. Phys Chem Chem Phys, 2014, 16: 18578–18585
206 Wang H, Senguttuvan P, Proffit DL, *et al*. Formation of MgO during chemical magnesiation of Mg-ion battery materials. ECS Electrochem Lett, 2015, 4: A90–A93
207 Sai Gautam G, Canepa P, Abdellahi A, *et al*. The intercalation phase diagram of Mg in V_2O_5 from first principles. Chem Mater, 2015, 27: 3733–3742
208 Okoshi M, Yamada Y, Yamada A, Nakai H. Theoretical analysis on de-solvation of lithium, sodium, and magnesium cations to organic electrolyte solvents. J Electrochem Soc, 2013, 160: A2160–A2165
209 Le DB, Passerini S, Guo J, *et al*. High surface area V_2O_5 aerogel intercalation electrodes. J Electrochem Soc, 1996, 143: 2099–2104
210 Malik R, Zhou F, Ceder G. Kinetics of non-equilibrium lithium incorporation in $LiFePO_4$. Nat Mater, 2011, 10: 587–590
211 Kim C, Phillips PJ, Key B, *et al*. Direct observation of reversible magnesium ion intercalation into a spinel oxide host. Adv Mater, 2015, 27: 3377–3384
212 Sánchez L, Pereira-Ramos JP. Electrochemical insertion of magnesium in a mixed manganese-cobalt oxide. J Mater Chem, 1997, 7: 471–473
213 Kumar GG, Munichandraiah N. Solid-state Mg/MnO_2 cell employing a gel polymer electrolyte of magnesium triflate. J Power Sources, 2000, 91: 157–160
214 Kumagai N, Komaba S, Sakai H, Kumagai N. Preparation of todorokite-type manganese-based oxide and its application as lithium and magnesium rechargeable battery cathode. J Power Sources, 2001, 97-98: 515–517
215 Kumar GG, Munichandraiah N. Solid-state rechargeable magnesium cell with poly(vinylidenefluoride)-magnesium triflate gel polymer electrolyte. J Power Sources, 2001, 102: 46–54
216 Kumar G, Munichandraiah N. Poly(methylmethacrylate)-magnesium triflate gel polymer electrolyte for solid state magnesium battery application. Electrochim Acta, 2002, 47: 1013–1022
217 Kurihara H, Yajima T, Suzuki S. Preparation of cathode active material for rechargeable magnesium battery by atmospheric pressure microwave discharge using carbon felt pieces. Chem Lett, 2008, 37: 376–377
218 Sheha E, El-Mansy MK. A high voltage magnesium battery based on H_2SO_4-doped $(PVA)_{0.7}(NaBr)_{0.3}$ solid polymer electrolyte. J Power Sources, 2008, 185: 1509–1513
219 Sheha E. Ionic conductivity and dielectric properties of plasticized $PVA_{0.7}(LiBr)_{0.3}(H_2SO_4)_{2.7M}$ solid acid membrane and its performance in a magnesium battery. Solid State Ionics, 2009, 180: 1575–1579
220 Rasul S, Suzuki S, Yamaguchi S, Miyayama M. High capacity positive electrodes for secondary Mg-ion batteries. Electrochim Acta, 2012, 82: 243–249
221 Zhang R, Yu X, Nam KW, *et al*. α-MnO_2 as a cathode material for rechargeable Mg batteries. Electrochem Commun, 2012, 23: 110–113
222 Rasul S, Suzuki S, Yamaguchi S, Miyayama M. Synthesis and electrochemical behavior of hollandite MnO_2/acetylene black composite cathode for secondary Mg-ion batteries. Solid State Ionics, 2012, 225: 542–546
223 Ling C, Mizuno F. Phase stability of post-spinel compound AMn_2O_4 (A = Li, Na, or Mg) and its application as a rechargeable battery cathode. Chem Mater, 2013, 25: 3062–3071
224 Rasul S, Suzuki S, Yamaguchi S, Miyayama M. Manganese oxide octahedral molecular sieves as insertion electrodes for rechargeable Mg batteries. Electrochim Acta, 2013, 110: 247–252
225 Yuan C, Zhang Y, Pan Y, *et al*. Investigation of the intercalation of polyvalent cations (Mg^{2+}, Zn^{2+}) into λ-MnO_2 for rechargeable aqueous battery. Electrochim Acta, 2014, 116: 404–412
226 Kim JS, Chang WS, Kim RH, *et al*. High-capacity nanostructured manganese dioxide cathode for rechargeable magnesium ion batteries. J Power Sources, 2014, 273: 210–215

227 Arthur TS, Zhang R, Ling C, *et al*. Understanding the electrochemical mechanism of K-αMnO_2 for magnesium battery cathodes. ACS Appl Mater Interfaces, 2014, 6: 7004–7008

228 Mizuno F, Singh N, Arthur TS, *et al*. Understanding and overcoming the challenges posed by electrode/electrolyte interfaces in rechargeable magnesium batteries. Front Energy Res, 2014, 2: 1–11

229 Nam KW, Kim S, Lee S, *et al*. The high performance of crystal water containing manganese birnessite cathodes for magnesium batteries. Nano Lett, 2015, 15: 4071–4079

230 Okamoto S, Ichitsubo T, Kawaguchi T, *et al*. Intercalation and push-out process with spinel-to-rocksalt transition on Mg insertion into spinel oxides in magnesium batteries. Adv Sci, 2015, doi: 10.1002/advs.201500072

231 Zhang R, Arthur TS, Ling C, Mizuno F. Manganese dioxides as rechargeable magnesium battery cathode; synthetic approach to understand magnesiation process. J Power Sources, 2015, 282: 630–638

232 Song J, Noked M, Gillette E, *et al*. Activation of a MnO_2 cathode by water-stimulated Mg^{2+} insertion for a magnesium ion battery. Phys Chem Chem Phys, 2015, 17: 5256–5264

233 Yamada A, Tanaka M, Tanaka K, Sekai K. Jahn-Teller instability in spinel Li–Mn–O. J Power Sources, 1999, 81-82: 73–78

234 Kim HS, Arthur TS, Allred GD, *et al*. Structure and compatibility of a magnesium electrolyte with a sulphur cathode. Nat Commun, 2011, 2: 427

235 Park OK, Cho Y, Lee S, *et al*. Who will drive electric vehicles, olivine or spinel? Energy Environ Sci, 2011, 4: 1621–1633

236 Spahr ME, Novák P, Haas O, Nesper R. Electrochemical insertion of lithium, sodium, and magnesium in molybdenum(VI) oxide. J Power Sources, 1995, 54: 346–351

237 Sian TS, Reddy GB. Infrared spectroscopic studies on Mg intercalated crystalline MoO_3 thin films. Appl Surf Sci, 2004, 236: 1–5

238 Pandey GP, Agrawal RC, Hashmi SA. Magnesium ion-conducting gel polymer electrolytes dispersed with fumed silica for rechargeable magnesium battery application. J Solid State Electrochem, 2011, 15: 2253–2264

239 Sutto TE, Duncan TT. Electrochemical and structural characterization of Mg ion intercalation into RuO_2 using an ionic liquid electrolyte. Electrochim Acta, 2012, 79: 170–174

240 Dueber RE, Fleetwood JM, Dickens PG. The insertion of magnesium into α-U_3O_8. Solid State Ionics, 1992, 50: 329–337

241 Sutto TE, Duncan TT. Electrochemical and structural characterization of Mg ion intercalation into Co_3O_4 using ionic liquid electrolytes. Electrochim Acta, 2012, 80: 413–417

242 Kamioka N, Ichitsubo T, Uda T, *et al*. Synthesis of spinel-type magnesium cobalt oxide and its electrical conductivity. Mater Trans, 2008, 49: 824–828

243 Ichitsubo T, Adachi T, Yagi S, Doi T. Potential positive electrodes for high-voltage magnesium-ion batteries. J Mater Chem, 2011, 21: 11764–11772

244 Sheha E. Studies on TiO_2/reduced graphene oxide composites as cathode materials for magnesium-ion battery. Graphene. 2014, 3: 36–43

245 Su S, Huang Z, NuLi Y, *et al*. A novel rechargeable battery with a magnesium anode, a titanium dioxide cathode, and a magnesium borohydride/tetraglyme electrolyte. Chem Commun, 2015, 51: 2641–2644

246 Padhi AK. Phospho-olivines as positive-electrode materials for rechargeable lithium batteries. J Electrochem Soc, 1997, 144: 1188–1194

247 Kang B, Ceder G. Battery materials for ultrafast charging and discharging. Nature, 2009, 458: 190–193

248 Makino K, Katayama Y, Miura T, Kishi T. Electrochemical insertion of magnesium to $Mg_{0.5}Ti_2(PO_4)_3$. J Power Sources, 2001, 99: 66–69

249 Makino K, Katayama Y, Miura T, Kishi T. Magnesium insertion into $Mg_{0.5+y}(Fe_yTi_{1-y})_2(PO_4)_3$. J Power Sources, 2001, 97-98: 512–514

250 Makino K, Katayama Y, Miura T, Kishi T. Preparation and electrochemical magnesium insertion behaviors of $Mg_{0.5+y}(Me_yTi_{1-y})_2(PO_4)_3$ (Me = Cr, Fe). J Power Sources, 2002, 112: 85–89

251 Huang Z, Masese T, Orikasa Y, *et al*. $MgFePO_4F$ as a feasible cathode material for magnesium batteries. J Mater Chem A, 2014, 2: 11578–11582

252 Huang ZD, Masese T, Orikasa Y, Mori T, Yamamoto K. Vanadium phosphate as a promising high-voltage magnesium ion (de)-intercalation cathode host. RSC Adv, 2014, 5: 8598–8603

253 Wu J, Gao G, Wu G, *et al*. $MgVPO_4F$ as a one-dimensional Mg-ion conductor for Mg ion battery positive electrode: a first principles calculation. RSC Adv, 2014, 4: 15014–15017

254 Feng Z, Yang J, NuLi Y, *et al*. Preparation and electrochemical study of a new magnesium intercalation material $Mg_{1.03}Mn_{0.97}SiO_4$. Electrochem Commun, 2008, 10: 1291–1294

255 Feng Z, Yang J, Nuli Y, Wang J. Sol-gel synthesis of $Mg_{1.03}Mn_{0.97}SiO_4$ and its electrochemical intercalation behavior. J Power Sources, 2008, 184: 604–609

256 NuLi Y, Yang J, Wang J, Li Y. Electrochemical intercalation of Mg^{2+} in magnesium manganese silicate and its application as high-energy rechargeable magnesium battery cathode. J Phys Chem C, 2009, 113: 12594–12597

257 NuLi Y, Yang J, Li Y, Wang J. Mesoporous magnesium manganese silicate as cathode materials for rechargeable magnesium batteries. Chem Commun, 2010, 46: 3794–3796

258 Nuli Y, Zheng Y, Wang F, *et al*. MWNT/C/$Mg_{1.03}Mn_{0.97}SiO_4$ hierarchical nanostructure for superior reversible magnesium ion storage. Electrochem Commun, 2011, 13: 1143–1146

259 Li Y, Nuli Y, Yang J, Yilinuer T, Wang. $MgFeSiO_4$ prepared via a molten salt method as a new cathode material for rechargeable magnesium batteries. Chinese Sci Bull, 2011, 56: 386–390

260 NuLi Y, Zheng Y, Wang Y, Yang J, Wang J. Electrochemical intercalation of Mg^{2+} in 3D hierarchically porous magnesium cobalt silicate and its application as an advanced cathode material in rechargeable magnesium batteries. J Mater Chem, 2011, 21: 12437–12443

261 Zheng Y, Nuli Y, Chen Q, *et al*. Magnesium cobalt silicate materials for reversible magnesium ion storage. Electrochim Acta, 2012, 66: 75–81

262 Orikasa Y, Masese T, Koyama Y, *et al*. High energy density rechargeable magnesium battery using earth-abundant and non-toxic elements. Sci Rep, 2014, 4: 5622

263 Wu J, Gao G, Wu G, *et al*. Tavorite-$FeSO_4F$ as a potential cathode material for Mg ion batteries: a first principles calculation. Phys Chem Chem Phys, 2014, 16: 22974–22978

264 Morgan D, Van der Ven A, Ceder G. Li conductivity in Li_xMPO_4 (M=Mn, Fe, Co, Ni) olivine materials. Electrochem Solid State Lett, 2004, 7: A30–A32

265 Bo SH, Grey CP, Khalifah PG. Defect-tolerant diffusion channels for M^{2+} ions in ribbon-type borates: structural insights into potential battery cathodes $MgVBO_4$ and $Mg_xFe_{2-x}B_2O_5$. Chem Mater, 2015, 27: 4630–4639

266 Zhao Y, Ban C, Xu Q, Wei SH, Dillon AC. Charge-driven structural transformation and valence versatility of boron sheets in magnesium borides. Phys Rev B, 2011, 83: 1–5

267 Zhang R, Mizuno F, Ling C. Fullerenes: non-transition metal clusters as rechargeable magnesium battery cathodes. Chem Commun, 2015, 51: 1108–1111

268 NuLi Y, Guo Z, Liu H, Yang J. A new class of cathode materials for rechargeable magnesium batteries: organosulfur compounds based on sulfur-sulfur bonds. Electrochem Commun, 2007, 9: 1913–1917

269 NuLi Y, Chen Q, Wang W, *et al*. Carbyne polysulfide as a novel cathode material for rechargeable magnesium batteries. Sci World J, 2014, 2014: 107918

270 Sano H, Senoh H, Yao M, Sakaebe H, Kiyobayashi T. Mg^{2+} storage in organic positive-electrode active material based on 2,5-dimethoxy-1,4-benzoquinone. Chem Lett, 2012, 41: 1594–1596

271 Chen Q, Nuli YN, Guo W, *et al*. PTMA/graphene as a novel cathode material for rechargeable magnesium batteries. Acta Phys Chim Sin, 2013, 29: 2295–2299

272 Kanakaiah V, Latha M, Sravan B, Palanisamy A, Rani JV. Rechargeable magnesium carbon-fluoride battery with electrolyte gel of ionic liquid and low molecular weight gelator. J Electrochem Soc, 2014, 161: A1586–A1592

273 Giraudet J, Claves D, Guérin K, *et al*. Magnesium batteries: towards a first use of graphite fluorides. J Power Sources, 2007, 173: 592–598

274 Kim H, Hong J, Park KY, *et al*. Aqueous rechargeable Li and Na ion batteries. Chem Rev, 2014, 114: 11788–11827

275 Wang RY, Wessells CD, Huggins RA, Cui Y. Highly reversible open framework nanoscale electrodes for divalent ion batteries. Nano Lett, 2013, 13: 5748–5752

276 Mizuno Y, Okubo M, Hosono E, *et al*. Suppressed activation energy for interfacial charge transfer of a Prussian blue analog thin film electrode with hydrated ions (Li^+, Na^+, and Mg^{2+}). J Phys Chem C, 2013, 117: 10877–10882

277 Mizuno Y, Okubo M, Hosono E, *et al*. Electrochemical Mg^{2+} intercalation into a bimetallic CuFe Prussian blue analog in aqueous electrolytes. J Mater Chem A, 2013, 1: 13055–13059

278 Zhang R, Ling C, Mizuno F. A conceptual magnesium battery with ultrahigh rate capability. Chem Commun, 2015, 51: 1487–1490

279 Zhao-Karger Z, Zhao X, Wang D, *et al*. Performance improvement of magnesium sulfur batteries with modified non-nucleophilic electrolytes. Adv Energy Mater, 2015, doi: 10.1002/aenm.201401155

280 Aurbach D, Gizbar H, Schechter A, *et al*. Electrolyte solutions for rechargeable magnesium batteries based on organomagnesium chloroaluminate complexes. J Electrochem Soc, 2002, 149: A115–A121

281 Tran TT, Lamanna WM, Obrovac MN. Evaluation of $Mg[N(SO_2CF_3)_2]_2$/acetonitrile electrolyte for use in Mg-ion cells. J Electrochem Soc, 2012, 159: A2005–A2009

282 Chen Q, Nuli YN, Yang J, Kailibinuer K, Wang JL. Effects of current collectors on the electrochemical performance of electrolytes for rechargeable magnesium batteries. Acta Phys Chim Sin, 2012, 28: 2625–2631

283 Cheng Y, Liu T, Shao Y, *et al*. Electrochemically stable cathode current collectors for rechargeable magnesium batteries. J Mater Chem A, 2014, 2: 2473–2477

284 Wall C, Zhao-Karger Z, Fichtner M. Corrosion resistance of current collector materials in bisamide based electrolyte for magnesium batteries. ECS Electrochem Lett, 2014, 4: C8–C10

285 Yagi S, Tanaka A, Ichikawa Y, Ichitsubo T, Matsubara E. Electrochemical stability of magnesium battery current collectors in a grignard reagent-based electrolyte. J Electrochem Soc, 2013, 160: C83–C88

286 Yagi S, Tanaka A, Ichitsubo T, Matsubara E. Electrochemical stability of metal electrodes for reversible magnesium deposition/dissolution in tetrahydrofuran dissolving ethylmagnesium chloride. ECS Electrochem Lett, 2012, 1: D11–D14

287 Gofer Y, Chusid O, Gizbar H, *et al*. Improved electrolyte solutions for rechargeable magnesium batteries. Electrochem Solid State Lett, 2006, 9: A257–A260

288 Sasaki I, Murase K, Ichii T, Uchimoto Y, Sugimura H. Anodic dissolution behavior of magnesium in hydrophobic ionic liquids. ECS Trans, 2011, 33: 65–70

289 Kratochvil B, Lorah E, Garber C. Silver-silver nitrate couple as reference electrode in acetonitrile. Anal Chem, 1969, 41: 1793–1796

290 Snook GA, Best AS, Pandolfo AG, Hollenkamp AF. Evaluation of a $Ag|Ag^+$ reference electrode for use in room temperature ionic liquids. Electrochem Commun, 2006, 8: 1405–1411

291 Ruch PW, Cericola D, Hahn M, Kötz R, Wokaun A. On the use of activated carbon as a quasi-reference electrode in non-aqueous electrolyte solutions. J Electroanal Chem, 2009, 636: 128–131

292 Chen Y, Devine TM, Evans JW, *et al*. Examination of the corrosion behavior of aluminum current collectors in lithium/polymer batteries. J Electrochem Soc, 1999, 146: 1310–1317

293 Myung ST, Hitoshi Y, Sun YK. Electrochemical behavior and passivation of current collectors in lithium-ion batteries. J Mater Chem, 2011, 21: 9891–9911

294 Doe RE, Blomgren GE, Persson KA. Rechargeable magnesium ion cell components and assembly. US Patent, 20110159381 A1, 2011-06-30

Acknowledgements This work was supported in part by the National Science Foundation of the US (CMMI-1030048 and DMR-1505902) and the University of Washington TGIF. Massé RC and Uchaker E would like to acknowledge the support from the State of Washington through the University of Washington Clean Energy Institute. Massé RC acknowledges Grips D. for inspiration while preparing the manuscript.

Author contributions Uchaker E and Massé RC prepared the manuscript with support and input from Cao G.

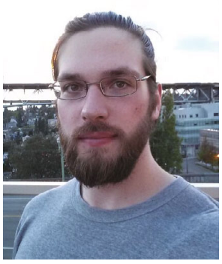

Robert C. Massé received his BSc degree from the University of Wisconsin-Madison. He is currently a PhD candidate at the University of Washington under the supervision of Prof. Guozhong Cao. His research interests include electrode materials for electrochemical energy storage devices such as alkali-ion batteries.

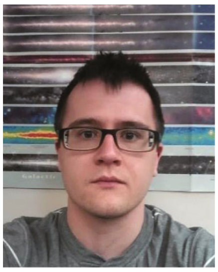

Evan Uchaker received his PhD degree in materials science and engineering at the University of Washington under the supervision of Prof. Guozhong Cao. His research interests are focused on the development and understanding of kinetically stabilized and defected electrode materials for electrochemical energy storage devices such as alkali-ion batteries.

Guozhong Cao is Boeing-Steiner Professor of materials science and engineering, professor of chemical engineering, and adjunct professor of mechanical engineering at the University of Washington, and also a professor at Beijing Institute of Nanoenergy and Nanosystems, Chinese Academy of Sciences and Dalian University of Technology. His current research is focused on chemical processing of nanomaterials for energy related applications including solar cells, rechargeable batteries, supercapacitors, and hydrogen storage.

中文摘要 对于经济和可持续能源存储设备的需求促进了当今电池的研究. 锂离子电池是目前最成熟的技术, 但是电化学储能的应用可通过降低成本和提高安全性进一步扩大. 钠和镁离子电池有可能成为两种可行的替代技术. 这两种金属比锂更便宜、储量更丰富, 并具有更好的安全特性, 而且二价镁还有一个附加优势, 即每个原子可以传输二倍的电荷. 另一方面, 钠和镁离子电池都还是新兴的研究领域, 仍有很多挑战需要克服. 例如, 因较大的离子穿梭而造成的重复形变使结合Na^+的电极容易粉末化, 而镁离子的插入和传输由于较大的静电作用力普遍显示出较慢的动力学特性. 本文综述了钠离子电池阴极和阳极材料的概况, 并对镁离子电池阴极的研究进行了全面总结. 此外, 本综述还讨论了文献中常见的一些实验差异, 指出了镁离子电化学研究的其他限制, 最后, 对未来研究提出了有价值的观点和策略.